Structural and magnetic properties of electrodeposited Fe x Ni 1-x ultra thin layers on Au(111)

Hugo Feitosa Jurca

▶ **To cite this version:**

Hugo Feitosa Jurca. Structural and magnetic properties of electrodeposited Fe x Ni 1-x ultra thin layers on Au(111). Condensed Matter [cond-mat]. Ecole polytechnique X, 2009. English. NNT : . tel-01252766

HAL Id: tel-01252766

https://pastel.hal.science/tel-01252766

Submitted on 8 Jan 2016
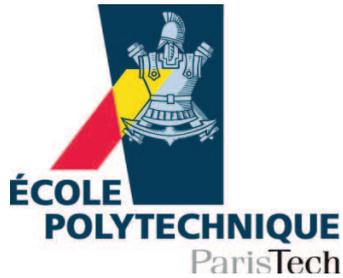
Thèse présentée pour obtenir le grade de

DOCTEUR DE L'ECOLE POLYTECHNIQUE

Spécialité : Physique

Par

Hugo FEITOSA JURCA

Structural and magnetic properties of electrodeposited Fe$_x$Ni$_{1-x}$ ultra thin layers on Au(111)

Soutenue le 27 novembre 2009 devant les membres du jury :

Dr Adilson J. A. de OLIVEIRA	UFSCAR	Rapporteur
Dr Daniel LINCOT	IRDEP EDF R&D	Rapporteur
Dr Jean-Eric WEGROWE	Ecole Polytechnique	Examinateur
Dr Philippe ALLONGUE	Ecole Polytechnique	Directeur
Dr Fouad MAROUN	Ecole Polytechnique	Co Directeur
Dr Dante H. MOSCA	UFPR	Co Directeur
Dr Robert CORTES	Ecole Polytechnique	Invité

To Juliana, my precious wife, to whom I owe all this work.

Acknowledgement:

Summary

Abstract

The magnetization of a film as well as its perpendicular magnetic anisotropy (PMA) are very sensitive to the film interfaces, to its morphology and to the atomic arrangement in the case of an alloy. The aim of this work is to investigate the magnetic properties of $Fe_x Ni_{(1-x)}$ ultrathin layers electrodeposited on Au(111) as a function their chemical composition and their atomic arrangement and to correlate them with their structural characterizations. For this purpose, we used real time in situ MOKE (Magneto-optical Kerr Effect), ex−situ extended X ray absorption fine structure (EXAFS) and ex−situ X−ray diffraction (XRD). Films of various composition were obtained by electrochemical co-reduction of the metal cations on the gold surface (Fe^{2+} and/or Ni^{2+}), at a rate ~ 0.1 atomic mono-layer per second (ML/s). The film stoechiometry was determined as a function of the deposition potential and the film thickness. Appropriate conditions were found to obtain an alloy film with a single phase solid solution, and which stoechiometry is fixed by the solution composition. EXAFS and XRD show that the films are in epitaxy with the Au(111) substrate. However, they also demonstrate that the film structure is stoechiometry dependent, with a strained bcc (110) phase for iron rich films (e.g. $Fe_{80}Ni_{20}$) and a relaxed fcc phase for lower iron content (e.g. $Fe_{50}Ni_{50}$). For layered Fe films deposited on Ni, we found evidence for a relaxed bcc phase for Fe and relaxed fcc phase for Ni. STM observations show that the alloy and the layered films are atomically flat. MOKE evidences a thickness dependent magnetic reorientation transition out of plane magnetization to in plane magnetization for $0.5 < x < 1$ (iron rich alloys). Moreover, the average magnetic moment per atom varies linearly with x, but remains smaller than that expected for completely magnetized iron atoms. On the other hand, for a layered film, the average magnetic moment per atom is very close to that expected for completely magnetized iron and nickel atoms. The contribution of the structural differences and of the local environment of the Fe atoms is discussed to evaluate the origin of the different magnetic behaviors.

Résumé

L'aimantation d'un film ainsi que son anisotropie magnétique perpendiculaire (PMA) sont très sensibles aux interfaces, à sa morphologie et à l'arrangement atomique dans le cas d'un alliage. L'objectif de ce travail est d'étudier les propriétés magnétiques des couches ultraminces $Fe_xNi_{(1-x)}$ électrodéposé sur Au (111) en fonction de leur composition chimique et leur arrangement atomique et de les corréler avec leur structure. À cette fin, nous avons utilisé les techniques de MOKE in situ (`Magnetic optical Kerr effect`), 'Extended X-ray Absorption Fine Structure' ex-situ (EXAFS) et la diffraction de rayons X ex-situ (XRD). Des films de compositions diverses ont été obtenus par co-réduction électrochimique des cations métalliques sur la surface d'or (Fe et/ou Ni), à une vitesse de dépôt ~ 0,1 mono couche atomique par seconde (ML/s). La stœchiométrie du film a été déterminée en fonction du potentiel et de l'épaisseur. Des conditions appropriées ont été trouvées pour obtenir un film d'alliage sous forme d'une solution solide avec une seule phase. Les mesures EXAFS et XRD montrent que les films sont en épitaxie avec le substrat de Au(111). Cependant, ils montrent aussi que la structure du film dépend de la stœchiométrie, avec une phase bcc (110) contrainte pour des films riches en fer (par exemple $Fe_{80}Ni_{20}$) et une phase fcc (111) relaxée pour une plus faible teneur en fer ($Fe_{50}Ni_{50}$ par exemple). Dans le cas d'une multi-couches de Fe déposé sur Ni, nous avons trouvé des évidences pour une phase de Fe bcc relaxée et une phase relaxée fcc pour Ni. Les observations STM montrent que les films sont atomiquement plans. Les mesures MOKE mettent en évidence une réorientation de l'aimantation hors du plan à l'aimantation dans le plan pour $0,5 < x < 1$ (alliages riches en fer) qui dépend de l'épaisseur du film. En plus, le moment magnétique moyen par atome varie linéairement avec x, mais reste inférieur à celui attendu pour une aimantation complète des atomes de fer. D'autre part, dans le cas d'une multi-couches Fe déposé sur Ni, le moment magnétique moyen par atome est très proche de celui prévu pour des atomes fer et de nickel complètement aimantés. La contribution de la structure et de l'environnement local des atomes de Fe sont discutés pour expliquer l'origine de ces comportements magnétiques.

Resumo

A magnetização de um filme, bem como a sua anisotropia magnética perpendicular (PMA) são muito sensíveis às interfaces do filme, à sua morfologia e ao arranjo atômico, no caso de uma liga metálica. O objetivo deste trabalho é de investigar as propriedades magnéticas de camadas ultrafinas de $Fe_xNi_{(1-x)}$ eletrodepositadas sobre Au(111), em função da sua composição química e seu arranjo atômico, e correlacioná-las com as suas caracterizações estruturais. Com esse objetivo, foram utilizadas como técnicas de caracterização: *"Magnetic Optical Kerr Effect"* (MOKE) in-situ, *"Extended X-ray Absorption Fine Structure"* ex-situ (EXAFS) e difração de raios-x ex-situ (XRD). Filmes de diferentes composições foram obtidos por co-redução eletroquímica de cátions metálicos na superfície do Au (Fe e/ou Ni), a uma velocidade de deposição de ~ 0,1 mono camada atômica por segundo (ML/s). A estequiometria dos filmes foi determinada em função do potencial eletroquímico e de suas espessuras. Condições apropriadas foram encontradas para obter um filme de liga metalica na forma de solução sólida com uma única fase. As medidas de EXAFS e XRD mostram que os filmes apresentam epitaxia com o substrato de Au(111); no entanto, esses experimentos também demonstram que a estrutura do filme depende da estequiometria, com uma fase bcc (110) dilatada para filmes ricos em Fe (por exemplo, $Fe_{80}Ni_{20}$) e uma fase fcc (111) relaxada para filmes pobres em Ni (por exemplo, $Fe_{50}Ni_{50}$). No caso de multi-camadas de Fe sobre Ni, encontramos evidências de uma fase bcc relaxada para o Fe e uma fase fcc também relaxada para o Ni. Observações usando a técnica STM mostram que os filmes são atomicamente planos. Medidas MOKE mostram evidências de uma reorientação magnética de spin, de uma magnetização fora do plano para uma magnetização no plano quando $0,5 < x < 1,0$ (ligas ricas em ferro) que dependem da espessura do filme. Além disso, o momento magnético médio por átomo varia linearmente com x, mas permanece menor que a média esperada para átomos de ferro saturados magneticamente. Por outro lado, no caso de multicamadas de Fe depositadas sobre Ni, o momento magnético médio por átomo é muito próximo do esperado para os átomos de Fe e de Ni magnetizados até a saturação. A contribuição da estrutura e do ambiente local dos átomos de Fe são discutidos para explicar a origem destes comportamentos magnéticos.

Chapter 1

Introduction

Spintronics, a neologism meaning "spin dependent electron transport" is a very recent concept which could develop thanks to key improvements in ultrathin epitaxial growth of magnetic layers, with only a few atomic layers in thickness. This crucial step led to the discovery of Giant Magnetic Resistance (GMR) [1] and Tunnel Magnetic Resistance.[2] The device consists of a stack of nm-thick magnetic layers separated by a non magnetic layer, which is a noble metal (GMR device) or an oxide (TMR device). The external resistance of the stack is low when the magnetization of the two layers are parallel (Fig. 1.1a) and high when the magnetization of the two layers are anti parallel (Fig. 1.1b). In the case of GMR we have oscillations of the interlayer coupling as a function of the non magnetic layer thickness.[3] The GMR is observed in the half-period with antiferromagnetic interlayer coupling. Another way to functioning is to exploit two magnetic layers with different coercive field. In the scheme above the top magnetic layer is magnetically softer than the lower one, valve spin device.[4] Different strategies have been developed to achieve this goal, including the incorporation of an antiferromagnetic layer that pins the bottom layer. More recently it was demonstrated that the magnetization of the soft layer can be reverse by injecting a current in GMR and TMR based devices. This is a key extension of the concept and are at the root of the enormous advances that occurred during the last decades in magnetic data storage industry.[5] Thanks to GMR it was possible to design miniaturized and very sensitive read heads which led to a very fast increase of magnetic hard disk capabilities. GMR heads allows also faster bit reading than past inductive read heads. Today magnetic disks have a storage capability of more than 100 Gb/in^2. Patterned GMR based MRAM are currently under development and future MRAM will probably be based on spin torque transfer switching (i.e. by injection of spin polarized current) [6].
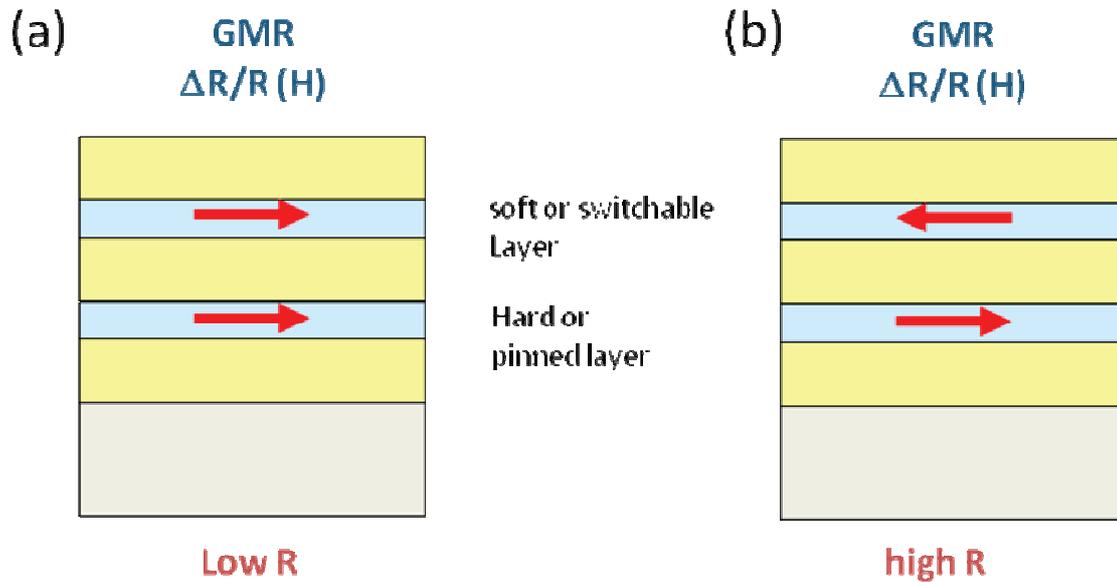
Figure 1.1 – Schematic principle of GMR device: two magnetic layers are separated by a thin layer of a noble metal. The thickness of layers are in the nm-range. The resistance of the stack is low when the magnetization of the two layers are parallel (a) and high when the magnetizations of the two layers are anti parallel (b). In the scheme the top magnetic layer is switchable.

One of the issues in spintronics is tailoring the magnetic properties of layers and nanostructures. This includes controlling the direction of magnetization (anisotropy), the coercive field and the magnetic moment. Maintaining the magnetization vector in a specific in plane direction is easily achieved by adapting the shape of the device. An oblate shape is sufficient. Obtaining a magnetization vector perpendicular to the surface, also called perpendicular magnetization anisotropy (PMA) requires nanostructures with a length greater than the diameter, which is a strong limitation since the lateral dimension of patterned nanostructures is typically 100 nm. The preferred alternative is considering ultrathin films. Surface-induced PMA was first predicted by L. Néel,[7] who performed theoretical study of magnetostriction, magnetocrystalline anisotropy, surface energy anisotropy. Néel demonstrated that the lower symmetry at the surface should promote PMA. Experimental evidence of PMA was given by depositing a magnetic layer on a substrate. Several reviews are available on the subject of PMA in ultrathin films.[8] In the case where PMA arises from the interface, there exists a critical thickness t* above which the magnetic easy axis rotates from out of plane to in-plane direction. At sufficiently small thickness, the interface to volume ratio is such that interface effects

dominate the magnetic properties of the layer. The morphology and structure of films, temperature [9] and interfaces [10] are the key factors influencing PMA.

Considering magnetic alloys is a complementary component to tailor magnetic properties of nanostructures. For instance, material engineering has become a key point to reduce the volume of material necessary to store one bit of information: PMA with magnetic alloys has a tendency to be the next generation of perpendicular magnetic recording and hard magnetic component, because they offer a large degree of freedom of magnetic properties. Some works demonstrated the presence of PMA in the alloys thin films of FePd/Cu(111) [11], CoPt/MgO(001) [12], FeCo and others [13] present a high uniaxial anisotropy. Special attention was also given to FeNi alloys for the Invar Effect, low coefficient of thermal expansion for Fe64Ni36 alloy.[14] It has been observed the existence of a collapse in the Curie temperature (T_c) and magnetic moment followed by the structural phase transition, from fcc into the bcc phase with increasing content of Fe.[15] Schumann et al[16] have used Fe_xNi_{1-x}/Cu(100), substrate on which Fe deposit is in the fcc structure, in order to understand the collapse of structural transformation. They found a not linear atomic volume variation in function of quantity of Fe, predicted before theoretically by Abrikosov.[17]

As mentioned above progress with GMR devices came from controlled epitaxial growth of stacks of layers using physical methods. Thermal deposition (TD) and to a much lesser extent pulsed laser deposition (PLD) of ultrathin layers on single crystal substrates or buffer layers have been the preferred techniques for fundamental studies, even though sputtering is technologically more relevant. However, electrochemical deposition has proven its ability to growth magnetic nanostructures such as nm-multilayers, nanowires and ultrathin films or various compositions. Electrochemical growth is a classical method to deposit alloys. Early works date back to 1905 with those of Fritz Spitzer.[18] Since they works about alloy electrodeposition have dealt with thin film deposition (several 10 of nm up to a few µm) for various industrial and technological applications, which include corrosion protection, jewelry, magnetism (inductive write heads) [19] and also semiconductor compounds for photovoltaics.[20]

Alloy electrodeposition is simply obtained by co-reducing two (or more) metal cations dissolved in an electrolyte (see Chapter 2 for the main principles of metal electrodeposition). Not so simple however is really controlling the film composition and microstructure because they *a priori* depend on the relative rate of deposition of individual metals (the relative concentrations

in metal cations and the applied potential are key parameters). Empirically it was however noticed that the less noble metal is codeposited at a faster rate than in the absence of the nobler element. This phenomenon is called *anomalous* deposition and was studied theoretically.[21] As a whole alloy electrodeposition remains very much empirical.

Electrochemical growth is also strongly relevant to grow nanowires with tailored sequences of metallic layers of variable composition by template deposition inside a porous insulating matrix.[22] Such nanostructures may present interesting transport and GMR properties.[23] Spin torque transfer switching was also reported with such structure.[24] Only a few groups studied epitaxial growth of Co[25,26], Fe[27] and Ni[25,28] on Au(111), Ni on Au(100)[29] and Cu(001)[30] single crystal electrodes. It was soon demonstrated that electrodeposited Co/Au(111) layers exhibit a strong perpendicular magnetization anisotropy (PMA), with an out of plane → in plane spin reorientation transition (SRT) occurring for a critical thickness of ~9 ML.[26] This value stands as a proof of the formation of well defined interfaces because it is close to the one measured with layers prepared by thermal deposition in the UHV.[31] Double layers (Co/Au) were also electrochemically grown, with each of the Co layer exhibiting PMA.[32] It should be added that our group has developed *in situ* magnetic characterizations. In cooperation with a Brazilian group at the Federal University in Porto Alegre (Laboratory of Magnetism, Physics Institute), AGFM was adapted to the electrochemical environment. For the first time magnetism of electrodeposited layers could be probed at sub monolayer coverage.[26,27,33] The development of *in situ* MOKE at our laboratory has constituted a real progress since real time measurements are now accessible with sub monolayer sensitivity.[34] Moreover, the information is now complete since magnetization curves can be recorded at a rate of 2 per second, during the deposition of the magnetic layer. By coupling *in situ* scanning tunneling microscopy (STM) observations with *in situ* real time MOKE our group[35] has developed studies in the spirit of those which have been performed in the UHV where the structure of layers and interfaces are correlated with the magnetic properties in the initial stages of the growth.

In this work we investigate magnetic FeNi alloy electrodeposition in the ultrathin film limit, which is rather unusual in the electrochemistry community. In addition, we couple thickness dependent structural and *in situ* real time magnetic characterizations, to gain insights into the nucleation and growth mode and the interplay between magnetism, in particular the strength of PMA, and alloy microstructure. A second aim of the present work is gaining new

insights into fundamental aspects of alloy electrodeposition. This is a supplementary reason to focus on the early stages of deposition and consider ultrathin films only. We have considered FeNi/Au(111) layers as a model system primarily because electrodeposited Ni [36] and Fe [27,34] layers are growing 2D on Au(111) and hoping that FeNi layers would also grow 2D. In fact one must be bear in mind that obtaining 2D alloy layers would ease the interpretation of magnetic data. We are aware that even *pure* Fe layers are a complex system rather than a simple model system. Iron may adopt different crystallographic structures (fcc or bcc) when it is in the form of an ultrathin layer deposited on a substrate. Fortunately there is a vast literature about FeNi layers grown by TD on various substrates and comparison with our data should be useful. There are also numerous theoretical works relating the magnetic properties of Fe, Ni and FeNi with the atomic volume and structure.

Apart theoretical and experimental aspects which are presented in chapter 2, the following manuscript is divided into three main chapters in which we describe and discuss results. Chapter 3 deals with Fe/Au(111). It revisits some past studies and also present new data about growth, structure and magnetic properties. Chapter 4 starts with a brief remainder about epitaxial growth and magnetism of Ni/Au(111) layers. It continues with a detailed study of Fe/Ni(1-2 ML)/Au(111) aiming at characterizing the influence of the Ni interlayer on Fe growth and magnetism. In fact, by depositing Fe on a Ni(111) interlayer not only we change the lattice parameter of the substrate but also we probe the *vertical* magnetic exchange coupling of the two films. Alloy growth and magnetism is finally investigated in Chapter 5.

Bibliography

[1] M. N. Baibich, J. M. Broto, A. Fert et al., "GIANT MAGNETORESISTANCE OF (001)FE/(001) CR MAGNETIC SUPERLATTICES," Phys. Rev. Lett. **61** (21), 2472-2475 (1988); P. Grunberg, R. Schreiber, Y. Pang et al., "LAYERED MAGNETIC-STRUCTURES - EVIDENCE FOR ANTIFERROMAGNETIC COUPLING OF FE LAYERS ACROSS CR INTERLAYERS," Phys. Rev. Lett. **57** (19), 2442-2445 (1986).

[2] J. S. Moodera, L. R. Kinder, T. M. Wong et al., "LARGE MAGNETORESISTANCE AT ROOM-TEMPERATURE IN FERROMAGNETIC THIN-FILM TUNNEL-JUNCTIONS," Phys. Rev. Lett. **74** (16), 3273-3276 (1995); H. Fujimori, S. Mitani, and S. Ohnuma, presented at the 5th NEC Symposium on Fundamental Approaches to New Material Phases - Spin-Dependent Phenomena in Multilayer Systems, Karuizawa, Japan, 1994 (unpublished).

[3] D. H. Mosca, F. Petroff, A. Fert et al., "OSCILLATORY INTERLAYER COUPLING AND GIANT MAGNETORESISTANCE IN CO/CU MULTILAYERS," Journal of Magnetism and Magnetic Materials **94** (1-2), L1-L5 (1991).

[4] A. M. Bratkovsky, "Spintronic effects in metallic, semiconductor, metal-oxide and metal-semiconductor heterostructures," Reports on Progress in Physics **71** (2), 31 (2008).

[5] E. Y. Tsymbal, O. N. Mryasov, and P. R. LeClair, "Spin-dependent tunnelling in magnetic tunnel junctions," J. Phys.-Condes. Matter **15** (4), R109-R142 (2003).

[6] J. E. Wegrowe, S. M. Santos, M. C. Ciornei et al., "Magnetization reversal driven by spin injection: A diffusive spin-transfer effect," Physical Review B **77** (17), 9 (2008).

[7] L. Néel, "*ANISOTROPIE MAGNETIQUE SUPERFICIELLE ET SURSTRUCTURES DORIENTATION," JOURNAL DE PHYSIQUE ET LE RADIUM **15** (4), 225-239 (1954).

[8] C. A. F. Vaz, J. A. C. Bland, and G. Lauhoff, "Magnetism in ultrathin film structures," Reports on Progress in Physics **71** (5), 78 (2008); Y. Shiratsuchi, M. Yamamoto, and S. D. Bader, "Magnetism and surface structure of atomically controlled ultrathin metal films," Prog. Surf. Sci. **82** (2-3), 121-160 (2007).

[9] P. J. Jensen and K. H. Bennemann, "Magnetic structure of films: Dependence on anisotropy and atomic morphology," Surf. Sci. Rep. **61** (3), 129-199 (2006).

[10] M. T. Johnson, P. J. H. Bloemen, F. J. A. den Broeder et al., "Magnetic anisotropy in metallic multilayers," Reports on Progress in Physics (11), 1409 (1996).

[11] C. F. Wang, K. M. Kuo, C. Y. Lin et al., "Magnetic anisotropy in (x=.30, .44, .55, .67, and .78) alloy film grown on and MgO(001) by molecular beam epitaxy," Solid State Communications **149** (37-38), 1523-1526 (2009).

[12] Iulica Zana, Giovanni Zangari, and Mohamad Shamsuzzoha, "Enhancing the perpendicular magnetic anisotropy of Co-Pt(P) films by epitaxial electrodeposition onto Cu(1 1 1) substrates," Journal of Magnetism and Magnetic Materials **292**, 266-280 (2005).

[13] T. Burkert, L. Nordstrom, O. Eriksson et al., "Giant magnetic anisotropy in tetragonal FeCo alloys," Phys. Rev. Lett. **93** (2), 4 (2004).

[14] Chih-wen. Chen, *Magnetism and metallurgy of soft magnetic materials*. (Amsterdam ; New York, 1977), p.571 p.

[15]   R. M. Bozorth, *Ferromagnetism*. (IEEE Press. , 1978).

[16]   F. O. Schumann, R. F. Willis, K. G. Goodman et al., "Magnetic instability of ultrathin fcc FexNi1-x films," Phys. Rev. Lett. **79** (25), 5166-5169 (1997).

[17]   I. A. Abrikosov, O. Eriksson, P. Söderlind et al., "Theoretical aspects of the FecNi1-c Invar alloy," Physical Review B **51** (2), 1058 (1995).

[18]   A. Brenner, *Electrodeposition of Alloys*. (New York, 1963).

[19]   Allen J. Bard, Faulkner, Larry R., *Electrochemical methods : fundamentals and applications*. (New York, 1980), p.718 p; T. Osaka, presented at the 50th Annual Meeting of the International-Society-of-Electrochemistry (ISE), Pavia, Italy, 1999 (unpublished).

[20]   S. Bastide, J. Vedel, D. Lincot et al., "PHOTOELECTROCHEMICAL DIFFUSION LENGTH MEASUREMENTS ON P-TYPE MULTICRYSTALLINE SILICON FOR PHOTOVOLTAIC APPLICATIONS," Journal of The Electrochemical Society **142** (3), 1024-1030 (1995).

[21]   N. Zech, E. J. Podlaha, and D. Landolt, "Anomalous Codeposition of Iron Group Metals: II. Mathematical Model," Journal of The Electrochemical Society **146** (8), 2892-2900 (1999); N. Zech, E. J. Podlaha, and D. Landolt, "Anomalous Codeposition of Iron Group Metals: I. Experimental Results," Journal of The Electrochemical Society **146** (8), 2886-2891 (1999); K. Y. Sasaki and J. B. Talbot, "ELECTRODEPOSITION OF BINARY IRON-GROUP ALLOYS," Journal of The Electrochemical Society **142** (3), 775-782 (1995); C. Grande Wendy and B. Talbot Jan, "Electrodeposition of Thin Films of Nickel-Iron," Journal of The Electrochemical Society **140** (3), 675-681 (1993); C. Grande Wendy and B. Talbot Jan, "Electrodeposition of Thin Films of Nickel-Iron," Journal of The Electrochemical Society **140** (3), 669-674 (1993).

[22]   S. Sharma, A. Barman, M. Sharma et al., "Structural and magnetic properties of electrodeposited Cobalt nanowire arrays," Solid State Communications **149** (39-40), 1650-1653 (2009).

[23]   L. Piraux, A. Encinas, L. Vila et al., "Magnetic and superconducting nanowires," Journal of Nanoscience and Nanotechnology **5** (3), 372-389 (2005); L. Piraux, J. M. George, J. F. Despres et al., "Giant Magnetoresistance in Magnetic Multilayered Nanowires," Applied Physics Letters **65** (19), 2484-2486 (1994).

[24]   Derek Kelly, Jean-Eric Wegrowe, Trong-kha Truong et al., "Spin-polarized current-induced magnetization reversal in single nanowires," Phys. Rev. B **68** (13), 134425 (2003); J. E. Wegrowe, A. Fabian, Guittienne Ph et al., "Exchange torque and spin transfer between spin polarized current and ferromagnetic layers," Applied Physics Letters **80** (20), 3775-3777 (2002).

[25]   P. Allongue, L. Cagnon, C. Gomes et al., "Electrodeposition of Co and Ni/Au(111) ultrathin layers. Part I: nucleation and growth mechanisms from in situ STM," Surf. Sci. **557** (1-3), 41-56 (2004).

[26]   L. Cagnon, T. Devolder, R. Cortes et al., "Enhanced interface perpendicular magnetic anisotropy in electrodeposited Co/Au(111) layers," Physical Review B **63** (10), 104419 (2001).

[27]   A. Gundel, L. Cagnon, C. Gomes et al., "In-situ magnetic measurements of electrodeposited ultrathin Co, Ni and Fe/Au(111) layers," Phys. Chem. Chem. Phys. **3** (16), 3330-3335 (2001).

[28]   F. A. Moller, J. Kintrup, A. Lachenwitzer et al., "In situ STM study of the electrodeposition and anodic dissolution of ultrathin epitaxial Ni films on Au(111)," Phys. Rev. B **56** (19), 12506-12518 (1997).

[29]   F. A. Moller, O. M. Magnussen, and R. J. Behm, Patent No. Part 1-2 (1999).

[30]   M. R. Vogt, F. A. Moller, C. M. Schilz et al., "Adsorbate-induced step faceting of Cu(100) electrodes in HCl," Surf. Sci. **367** (2), L33-L41 (1996).

[31]   C. Chappert, P. Bruno, B. Bartenlian et al., "Magnetic anisotropy and interlayer exchange coupling in Fe(110) / Au(111) ultrathin films," Journal of Magnetism and Magnetic Materials **148** (1-2), 165-166 (1995).

[32]   P. Prod'homme, F. Maroun, R. Cortès et al., "Preparation, characterization and magneto-optical investigations of electrodeposited Co/Au films," Journal of Magnetism and Magnetic Materials **315** (1), 26-38 (2007).

[33]   L. Cagnon, A. Gundel, T. Devolder et al., "Anion effect in Co/Au(111) electrodeposition: structure and magnetic behavior," Appl. Surf. Sci. **164**, 22-28 (2000).

[34]   Philippe Allongue, Fouad Maroun, Hugo F. Jurca et al., "Magnetism of electrodeposited ultrathin layers: Challenges and opportunities," Surface Science **603** (10-12), 1831-1840 (2009).

[35]   P. Allongue and F. Maroun, in *Electrocrystallization and Nanotechnology*, edited by G. Staikov (Wiley - VCH, Weinheim, 2006), pp. 217 - 241; P. Allongue and F. Maroun, "Metal electrodeposition on single crystal metal surfaces mechanisms, structure and applications," Curr. Opin. Solid State Mat. Sci. **10** (3-4), 173-181 (2006).

[36]   P. Allongue, L. Cagnon, C. Gomes et al., "Electrodeposition of Co and Ni/Au(1 1 1) ultrathin layers. Part I: nucleation and growth mechanisms from in situ STM," Surface Science **557** (1-3), 41-56 (2004); S. Muller, P. Bayer, C. Reischl et al., "STRUCTURAL INSTABILITY OF FERROMAGNETIC FEE FE FILMS ON CU(100)," Phys. Rev. Lett. **74** (5), 765-768 (1995).

Chapter 2

Theory and experimental procedures

This chapter deals with some theoretical concepts and fundamental aspects of measurements employed in this thesis. The basis of electrochemical deposition is presented in the section 2.1. Section 2.2 and 2.3 present the theoretical bases of x-ray diffraction (XRD) and Extended X-ray Absorption Fine Structure (EXAFS), respectively. Real time *in situ* Magneto Optical Kerr Effect (MOKE) magnetometer (coupled with in situ electrochemical cell) is introduced in section 2.4, along with details of the Kerr effect itself. In section 2.5 we describe the preparation of epitaxial Au/Si(111) buffer layers used as substrate in this work.

2.1 Electrochemistry

The domains of application of electrochemistry are very broad. This includes: energy production (batteries and accumulators), chemical reactions using the electric energy (electrolysis), detection and sensing of chemical specimens (analytical electrochemistry), mechanism determination and reaction kinetics (organic electrochemistry, corrosion). Electrochemical techniques are also widely used in microelectronics industry, in particular to perform interconnect and also magnetic inductive heads.

2.1.1 Interface Metal/Liquid

In the case of electrodeposition, the electrochemical solution (electrolyte) is generally an aqueous solution containing metallic ions M^{z+}, and is an ionic conductor; the working electrode is an electronic conductor. Both of them are characterized by the Fermi level E_F ($E_{F,S}$ and $E_{F,M}$, respectively), and the work function, that is the energy necessary to transfer one electron from the vacuum energy level to the Fermi energy level. Setting in contact the two phases creates an interfacial region where the organization of the solvent is strongly modified. The exact picture of the interface is however still in debate. From a macroscopic viewpoint it is generally accepted that the interface layer behaves like a planar capacitor of dielectric constant $\varepsilon \sim 6$ and thickness d

~ 3Å (Fig. 2.1), as derived from impedance measurements.[1] This region next to the interface is known as electrochemical double layer or the Helmholtz layer.

Before contact, each phase is characterized by its Fermi level (Fig. 2.2a). Upon contact and at thermodynamic equilibrium, the Fermi levels of both phases are equal which leads to exchange of free charges. As a result, both sides of the interface region are charged and a potential drop appears as shown in Fig. 2.2b. In practice the potential is measured with respect to a reference of potential in solution, which is a well defined redox system. In the case of the normalized hydrogen electrode (NHE) the associated energy level is 4.25 eV below vacuum level [1], Fig. 2.2c.
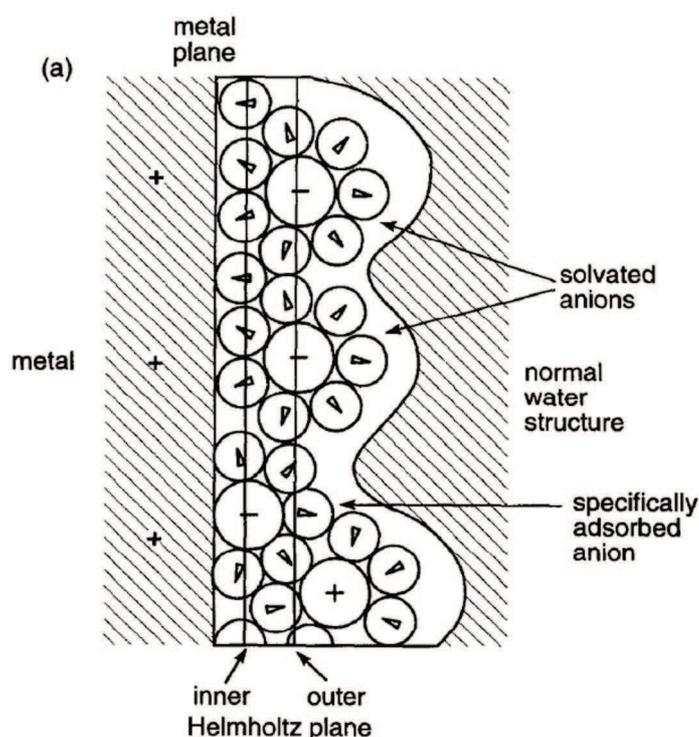
Figure 2.1 - **Model of the metal-electrolyte interface (electrical double layer) under conditions where anions are specifically adsorbed. Adapted from Ref. 2.**
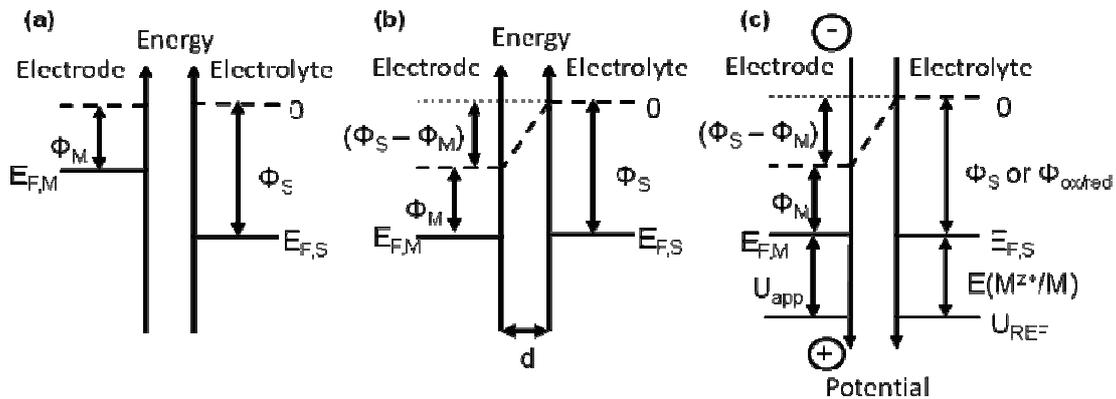
Figure 2.2 – (a) Energy diagram of the electrochemical interface before contact; (b) Same after contact formation and at thermodynamic equilibrium. (c) Same as (b) but with a reference of potential in solution.

Until now we presented the existence of a potential in the equilibrium, for the metal/solution interface, and they are linked with the difference at the Fermi level. This result has a particular value of electrode potential E_{eq}, which gives the possibility to realize the electrochemical equilibrium, i.e. the equality of both Fermi level at the interface: $E_F = E_F^{redox}$. This configuration of interface is represented in the Figure 2. 3 (c).

The application of a potential at the working electrode more positive to the equilibrium value (Figure 2. 3 (a)) causes a decrease of the Fermi level at the electrode. This results the transfer of electrons to the electrode (i. e. the oxidation of a chemical element in solution). Inversely, the application of a potential more negative than equilibrium potential (Figure 2. 3 (c)) leads to electron transfer from the electrode to the solution, resulting in the reduction of a chemical element. If we work with a metallic ion (M^{z+}) in solution, the reduction reaction means the deposition of ions (M^0) plus z electrons, whereas oxidation reaction gives back the z electrons with the ion returning to the solution as before (M^{z+}).
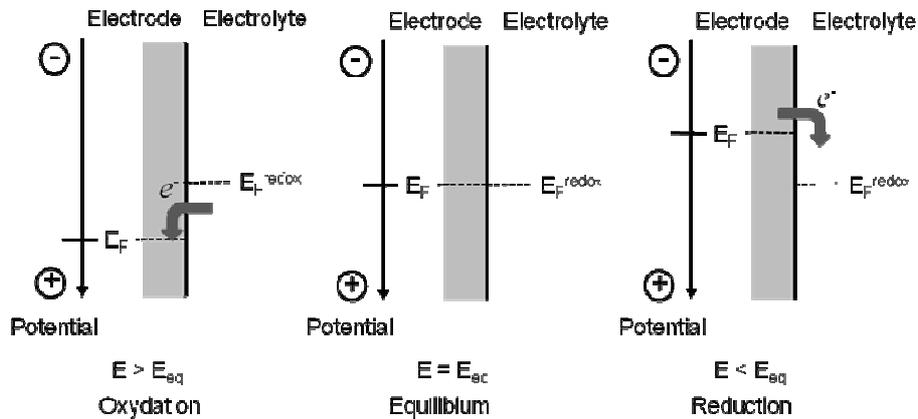
Figure 2. 3 - Scheme of electrode/electrolyte interface in three different configurations: (a) Oxidation, (b) Equilibrium and (c) Reduction.

The redox potential $E(M^{z+}/M)$ of the electrochemical reaction $M^{z+} + ze^- \leftrightarrow M$ is:

$$E\left(M^{z+}\!\!\Big/_{M}\right)= E^0\left(M^{z+}\!\!\Big/_{M}\right)+\frac{RT}{zF}\ln\left(\frac{a_{M^+}}{a_M}\right) \qquad \text{(Eq. 2.1)}$$

or at room temperature

$$E\left(M^{z+}\!\!\Big/_{M}\right)= E^0\left(M^{z+}\!\!\Big/_{M}\right)+\frac{0.59}{z}\ln\left(\frac{a_{M^+}}{a_M}\right) \qquad \text{(Eq. 2.2)}$$

This equation was established by Nernst in the beginning of XX century, and is known as Nernst law. [1] This equation shows that the Nernst potential depends on the concentration in metal ions. Symbols in Eq. 2.2 are:

- $E^0(M^{z+}/M)$ is the standard redox energy of reaction measured with respect to a reference of potential

- R is the perfect gas constant (R = 8.32 J/mol)

- T the temperature (T = 298 K)

- z number of electros changed

- F Faraday constant (F = 96500 C/mol)

- a_M^+ activity of metallic ions

- a_M activity of a pure metallic (conventionally a_M = 1)

The values of standard potentials of redox couples (M^{z+}/M) are tabulated in text books [3] versus the normal hydrogen electrode (NHE). In this work we used a saturated mercury/mercurous sulfate electrode (MSE) as reference of potentials. In the following, all potentials will be quoted against MSE. Table 2.1 lists the standard potentials of a few redox couples relevant to this thesis.

If the potential U applied to the electrode M is different from U_{eq} then metal bulk phase can be deposited ($U < U_{eq}$) or dissolved ($U > U_{eq}$). The magnitude of the deviation of the electrode potential U from the equilibrium value U_{eq} is often termed the overpotential η:

$$\eta = U - U_{eq} \qquad \text{(Eq. 2.3)}$$

and its sign is obviously determined whether U is lower than (cathodic overpotential) or greater than (anodic overpotential) U_{eq}. For $\eta < 0$, the growth process is called overpotential deposition.

Table 2.1 - Standard potentials for different redox couples with concentration solution of 1 M [3].

Redox Couple	Electrode Reaction	$U°$ / V_{NHE}	$U°$ / V_{MSE}
Fe^{2+}/Fe	$Fe^{2+} + 2e^- \leftrightarrow Fe$	-0.447	-1.087
Ni^{2+}/Ni	$Ni^{2+} + 2e^- \leftrightarrow Ni$	-0.257	-0.897
O/O$^-$	$O_2 + H_2O + 2e^- \leftrightarrow$ $HO_2^- + OH^-$	-0.076	-0.716
NHE electrode H_2/H^+	$H_2 + 2e^- \leftrightarrow 2H^+$	0.0	-0.64
MSE electrode Hg_2SO_4 /Hg	$Hg_2SO_4 + 2e^- \leftrightarrow 2Hg$ $+ SO_4^{2-}$	0.64 (saturated KCl)	0.0

2.1.2 Electrochemical charge transfer

To reduce a metal cation into an adatom at the electrode surface, or to promote the reaction $M^{z+} + ze^- \leftrightarrow M$, two phenomena are required in sequence:

- Ion diffusion in solution towards the electrode surface
- Charge transfer at the electrode surface.

The electrochemical charge transfer is a thermally activated process which activation energy barrier varies with the applied electrode potential.[1] The relationship between the current density i (expressed in A.cm^{-2}) and the applied potential η is given by the equation Erdey-Gruz and Volmer [4], derived from the Butler-Volmer equation:

$$i = i^+ + i^- = i_o \left[\exp\left(\frac{(1-a)zF}{RT}\eta \right) - \exp\left(\frac{-azF}{RT}\eta \right) \right].$$

(Eq. 2.4)

The overall current density i is actually the sum of the partial current densities related to the anodic (metal dissolution) and cathodic (metal deposition) partial reactions (i^+ and i^-, respectively). The electrochemical charge transfer coefficient α is a symmetry factor of the activation barrier ($0 < \alpha < 1$), and i_o corresponds to the exchange current density and is related to reaction kinetics.
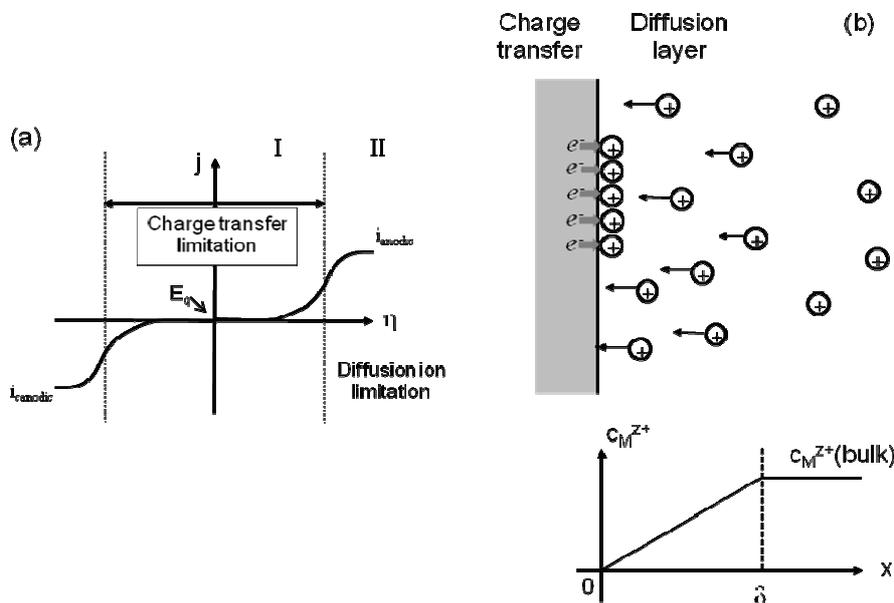
Figure 2.4 – (a) Simplified schematic current density versus applied potential. In region I, η ~ 0 and the reaction rate is limited by the electrochemical charge transfer. The current rises exceptionally. In region II, the reaction is limited by mass transport in solution. The current becomes independent of the applied potential indicating that the reaction becomes limited by the diffusion of caions in solution. (b) Scheme of concentration profile and diffusion layer approximation (dashed line). x = 0 corresponds to the electrode surface and δ is the diffusion layer thickness.

According to equation 2.4 the current density varies exponentially with the applied overpotential η, as schematically represented in Figure 2.4 (a). At small negative values of η (region I in fig. 2.4) the electrochemical transfer is limited by the kinetics and the concentration of ion at the electrode surface ($0 \leq x \leq \delta$) remains roughly equal to the one in the bulk of the solution (see Figure 2.4 (b). This deposition regime is usually defined as the kinetic regime. However, at large enough negative η (region II in fig. 2.4,) the reactive species are consumed so fast that the solution becomes depleted in reactive species in the vicinity of the electrode surface. As a result the reaction rate becomes limited by the diffusion of these species from the bulk solution to the electrode surface. The consumption of ions leads to a concentration gradient which extends over a distance δ termed the diffusion layer thickness. In this case the current density is given by the Fick's law. In this situation the ion concentration decreases to zero at the surface and is equal to:

$$i_{\text{lim}} = \text{-z}FD\frac{c_{M^{z+}}(\text{bulk})}{\delta} \qquad \text{eq. 2.7}$$

where D is the diffusion coefficient of species in the solution (typical values are~ 10^{-5} cm^2.s^{-1} for Fe and Ni) and c_M^{2+} (bulk) is the concentration ions. The expression for δ depends on the hydrodynamic conditions in the cell [1]. In unstirred solutions, the value of δ is time dependent and increases until it reaches an approximately constant value of ~100 µm due to microscopic convection effects.

2.1.3 Electrochemical growth

The electrodeposition is controlled by the value of the applied potential (η) which not only determines the flux but also may affect the deposition process by changing the electrode surface properties. On the atomic scale, the electrodeposition process implies the loss of the water shell surrounding the ions in solution and the creation of a surface adsorbed cation. The electrochemical discharge of the adsorbed cation creates an adatom. This process is represented in the Figure 2.5.
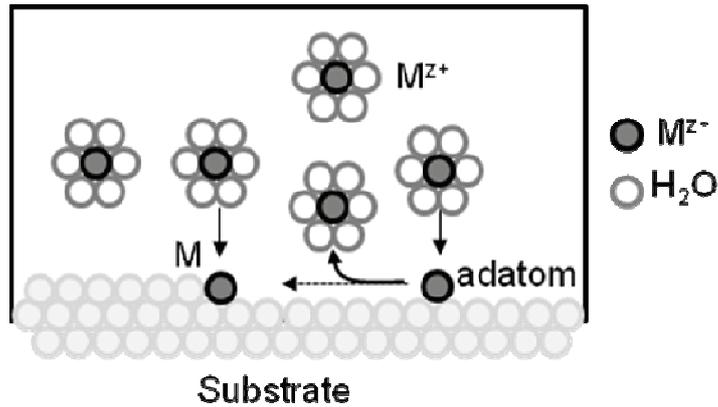
Figure 2.5 – Schematic description of electrochemical deposition: An adatom is created after electron transfer between the substrate and the cation M^{z+}. The adatom may diffuse on the surface and/or be dissolved according to the applied potential.

Close to the equilibrium potential, i.e. for $\eta \sim 0$, the adatom is unstable on defect free regions of the surface, unless they strongly interact with the substrate, and it can be dissolved in solution. In this case the description of the growth process relies on classical thermodynamic theory applied to epitaxial thin film growth. This approach takes into account the energy of the substrate, of the deposited metal and of the boundary between the substrate and the ad-layer. It leads to the definition of the so-called growth modes: (a) Volmer-Weber (VW) growth mode (island growth), (b) Frank-van der Merwe (FM) growth mode (layer-by-layer growth), (c) Stranski-Kranstanov (SK) growth mode (initially layer-by-layer growth and after critical thickness, island growth), which are represented in the Figure 2.6.[5] One factor which can determine the growth mode process is, for example, the surface energy.
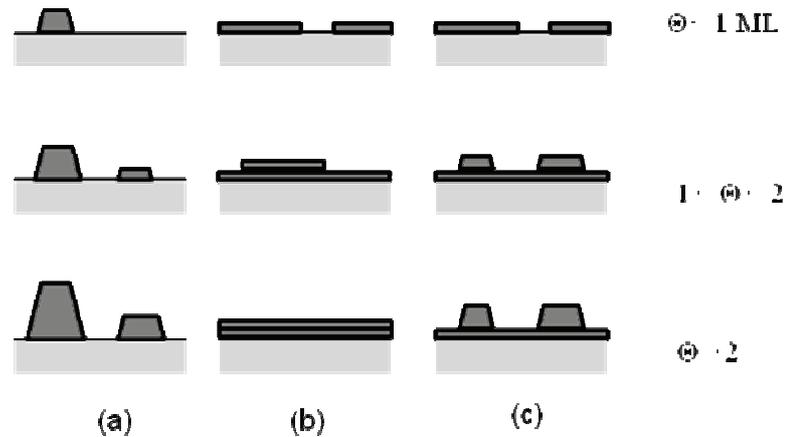
Figure 2.6 – Possible growth modes: (a) Volmer-Weber (VW) or island growth, (b) Frank-van der Merwe (FM) or layer-by-layer growth, (c) Stranski-Kranstanov (SK) or initially layer-by-layer growth followed, after critical thickness, by island growth.

At large enough potential, the growth process occurs far from equilibrium implying that the formed adatom is irreversibly stabilized on the surface. Then, it diffuses on the surface to aggregate into islands with other adatoms. Hence, the obtained morphology is influenced by kinetics rather than by thermodynamics and the term growth mode should now be replaced by growth morphologies. In this case, classical theory of nucleation and growth applies. This process resembles to the situation found for molecular beam epitaxial (MBE) with the existence of the same elementary steps involved during the growth (such as adsorption potential, surface diffusion barrier, Ehrlich-Schwoebel barrier). For a given deposition flux, the density of islands depends on the surface diffusion coefficient of the adatoms which may vary with η, via co-reactions, structural changes or changes in surface chemistry [6].

2.2 X-Ray diffraction

X-ray diffraction (XRD) was employed to determine the structure and the epitaxial relationship between the film and substrate. The concept and physical of measurable properties are discussed in this section. For more detail see text books.[7] This technique consists to incident the x-ray beam, with wavelength in the order of Angstrom, onto the sample and analyzing the radiation reflected by the crystal planes. At our laboratory we use a Cu Kα_1 x-ray tube (wavelength λ = 1.54 Å, E = 8.048 keV). The penetration depth can reach the µm scale,

depending to the incident angle and the analyzed material. But if the incident angle is grazing the penetration depth is very low, as we will see in the next paragraph. Given the very low samples thickness employed in this work, it is necessary to work at grazing incidence angle to maximize the optical path of X-rays in the film and increase the signal to noise ratio.

a) X-ray penetration depth:

Compton works show that there is a critical angle below which the x-ray beam is reflected by matter.[7] However, when the incident angle is close to zero the incoming beam becomes evanescent and propagates parallel and close to the surface. Below critical angle the penetration depth is particularly weak in the order of 1-2 nm, depending on the material density. However, above critical angle the penetration depth rapidly increases towards the value $\mu sin\theta$, where μ is the linear absorption coefficient and θ the incident angle,[7] as show in Figure 2.7. These curves were calculated using the method described by Parratt.[8] They show that the critical angle do depend on the material. For gold and E = 8048 eV the critical angle is equal to 0.6°. It is ~0.4° for Fe and Ni.
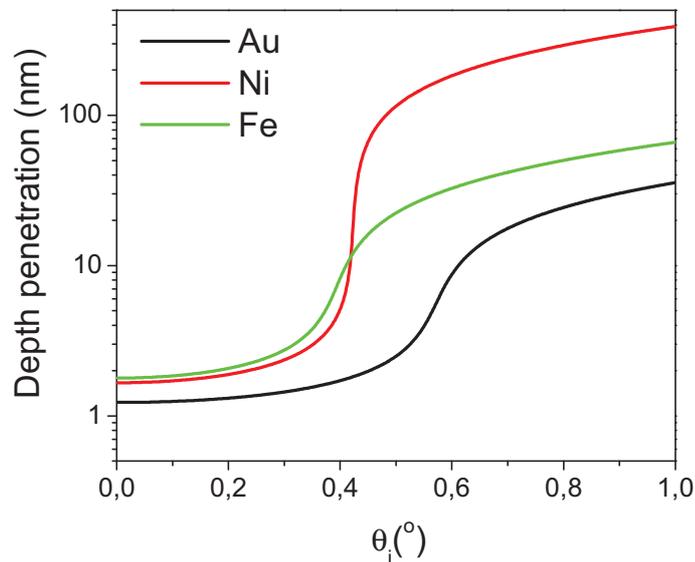
Figure 2.7 – Penetration depth of x-rays as function of the incident angle for Au (black line), Ni (red line) and Fe (green line). The beam energy is E = 8048 eV. Note that above the critical angle the depth penetration increases drastically.

b) Diffraction condition and experimental geometry:

The appropriate configuration to study the structure and epitaxial relationship of ultrathin films is working at low incidence angle and using a four circle diffractometer (two circles for the sample and two circles for the detector, see Figure 2.8). This way one may chose the incidence angle θ_i and rotate the sample in the perpendicular direction of the sample plane Φ (see Figure 2.8 (a)). The detector position is defined by its height (angle δ) and azimuth (angle γ) (see Figure 2.8 (b)).
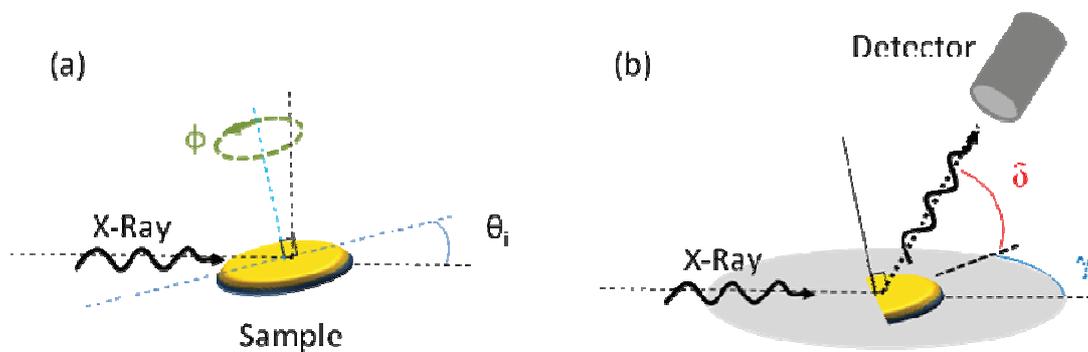
Figure 2.8 – Conditions used for X-ray diffraction, (a) θ_i is the incidence angle and Φ the rotation angle around the normal axis; (b) the detector position, is defined by the angles γ (azimuth) and δ (height)

The incident x-ray beam can be represented by the incident wave vector $\mathbf{k_i}$ and the diffracted x-ray beam by the diffracted wave vector $\mathbf{k_d}$, where $k_i = k_d = 2\pi/\lambda$. In the case of elastic diffusion, i.e. when the diffraction and incident wave vector have the same modulus, the diffusion vector is $\mathbf{Q} = \mathbf{k_d} - \mathbf{k_i}$. The diffused intensity is very weak except at the vicinity of diffraction condition given by $\mathbf{Q} = \mathbf{G}$, where $\mathbf{G}$ is a vector in the reciprocal space with modulus equal to $|\mathbf{G}| = 2\pi/d$, and d is the inter-planar lattice distance. The modulus of $|\mathbf{Q}| = |\mathbf{\Delta k}| = (4\pi/\lambda)\sin\theta_B$, where θ_B is the projection angle in relation to the diffracted lattice plane (see Figure 2.9). With the condition $\mathbf{Q} = \mathbf{G}$ we can deduce the Bragg law as $n\lambda = 2d\sin\theta_B$.
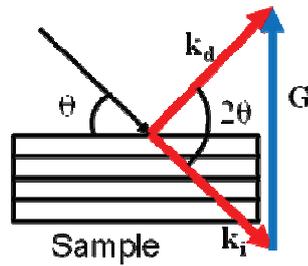
Figure 2.9 - Vector representation of diffraction x-ray condition.

The scans performed in this work are principally around the axis perpendicular to the sample surface, or an Φ rotation, with grazing incidence angle. To perform this experiment the x-ray detector is placed in the Bragg conditions expected for a family of crystallographic plane of a given structure. Therefore, in this configuration we can study: the lattice and the epitaxial relationship between the substrate and deposited film and the film mosaicity.

One may represent a x-ray scan in the reciprocal space using the Ewald sphere: see Figure 2.10 which shows the Ewald sphere with Si(111) sample in the reciprocal space [7]. The three **G** vectors (blue arrows) in this schema represent the three plane family [-111] (meaning the three specific plane (-111), (1-11) and (11-1) of Si sample). By rotating the sample in Φ the three **G** vector will cross the Ewald sphere producing the diffraction phenomenon, in the Bragg condition, and will be observed by the detector during the Φ scan.
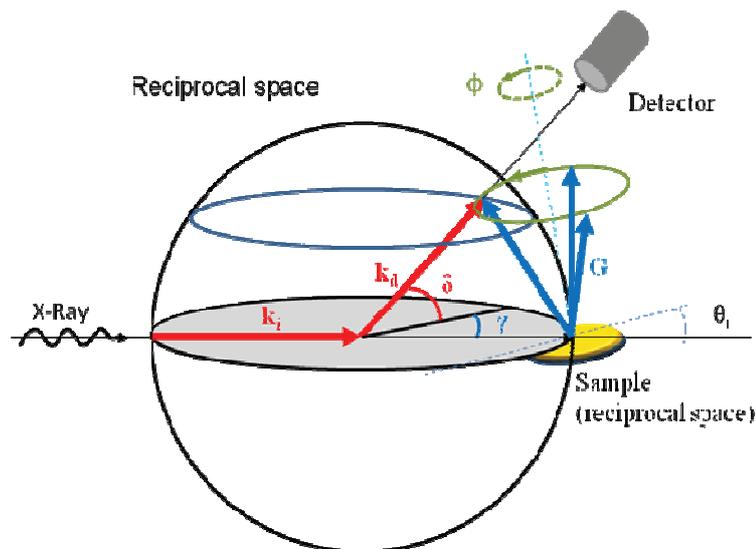
Figure 2.10 - Reciprocal space x-ray diffraction geometry, where the sample rotates in the axis perpendicular to the sample surface.

c) Coherent Bragg Rod Diffraction

A sample is the agglomeration of a large quantity of single crystalline grains. The reciprocal space is the lattice Fourier transform of each grain in the diffracted film. The Fourier transform of a very large lattice gives a pattern in the reciprocal space (see Figure 2.11 (a)), with area point dimension inversely proportional to the bulk dimension. This area of diffraction is called the diffraction domain. The Fourier transform of a thin film is a point ensemble linked by a line in one specific direction (see Figure 2.11 (b)), and the Fourier transform for one atomic layer film is represented by lines in the reciprocal space (see Figure 2.11 (c)). For a finite film the density distribution in the reciprocal space has an Airy function aspect ($\sin^2 \pi N x / \sin^2 \pi x$ where N is the number of monolayers). The density distribution of Airy function can be approximate by an Gaussian function peak, and the Full Width Half Maximum (FWHM) of peak is inversely proportional to the film thickness [9]. The scattering experiment performed in the link line of each point in the reciprocal space is known as a Coherent Bragg Rod Diffraction, and is a large area of research [10]. When the scattering experiments are performed with ultrathin samples, film the Coherent Bragg Rod Diffraction of substrate start to be relatively important. In our case we did not use this kind of diffraction.
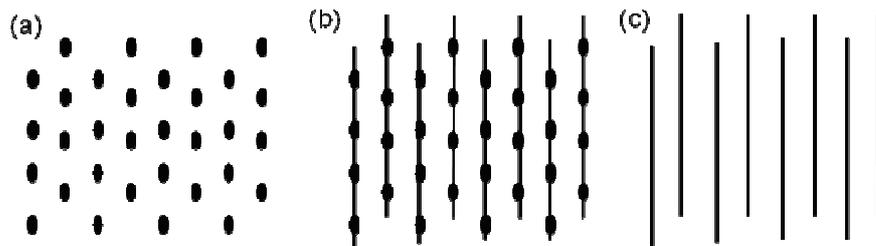
Figure 2.11 – Reciprocal space representation of: (a) perfect 3D crystal, (b) perfect 2D crystal and (c) a one atomic layer.

The intensity observed is proportional to the intersection of diffraction domain with the Ewald sphere. In our experiment we used large slits detector to increase the signal to noise ratio and minimize the integration time at each Φ angle. The large width slits permit to integrate the totality signal resulting from the intersection of the domain of diffraction with the Ewald sphere.

However, we have to choose the slit width in order to separate, if is possible, the searched ray to the parasite ray (for example arising from the substrate).

d) Full Width Half Maximum (FWHM) and diffracted object size

The experimental width of diffraction peaks depends on the dimension of the physical dimensions of grains and the mosaicity. For diffraction planes almost perpendicular to the sample surface, and supposing no mosaicity the FWHM is given by

$$\Delta\theta_S = \frac{\lambda \sin \alpha}{L \sin(\theta_B)} \qquad \text{eq. 2.8}$$

where λ is the x-ray wavelength, L average lateral grain size, θ_B the Bragg angle and α the angle between the sample plane and the diffracted plane. In the case of in plane mosaicity of grains, the complete relation becomes

$$\Delta\theta^2 = \Delta\theta_S^2 + \Delta\theta_M^2 \qquad \text{Eq. 2.9}$$

where $\Delta\theta_S$ refers to the grain size contribution and $\Delta\theta_M$ to the mosaicity.

The Bragg condition leads to $\Delta Q = 2\pi/L$, with L the lateral dimension of grains in the direct space. The mosaicity m corresponds to the average disorientation (Root Mean Square). Therefore, the mosaicity contribute to the enlargement of **Q** but with constant angular width equal to the mosaicity. In the Figure 2.12 is represented the reciprocal space with the two principal effects influencing FWHM.
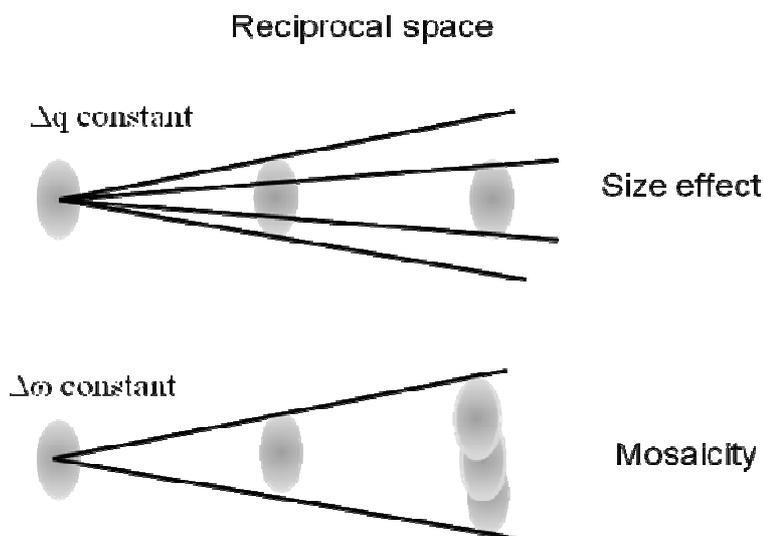
Reciprocal space

Figure 2.12- Reciprocal space and the two principal influences of FWHM; the grain size effect (Δq) and the mosaicity ($\Delta \omega$).

e) X-ray Nitrogen chamber:

A nitrogen atmosphere was created above the sample to perform the x-ray experiment in controlled atmosphere so as to avoid air oxidation of samples covered with a monolayer of carbon monoxide (CO). A chamber made of a Mylar film was constructed and flushed with N_2 (flux of 1 cm^3/s).

2.3 Extended X-ray Absorption Fine Structure (EXAFS)

a) Principle and method:

EXAFS yields information about the *local* arrangement of atoms around the absorbing atom. EXAFS signal refers to the variation of x-ray absorption, $\mu(E)$, as a function of the photon energy, close to the absorption edge E_0. In fact, if a photon of energy $E > E_0$ excites a core level electron this generates a photoelectron which propagates in the form of spherical wave around of excited atom. If the excited atom is in a condensed phase, the photoelectron is scattered by the neighboring atoms. The wave associated with the incident photoelectron interferes with that of the backscattering photoelectron. The backscattering waves will superpose or not depending on their relative phase. The total amplitude of the electron wave function will be enhanced or

reduced, respectively, thus modifying the probability of the x-ray absorption. Thus the variations of the fine structure in EXAFS as shown in Figure 2. 14 (a) are a direct consequence of the wave nature of the photoelectrons and oscillation are characteristic of the local environment. In fact the mean free path of one photoelectron, of wave vector $k = \sqrt{2m(E - E_0)}/\hbar$, is only a few Å long, depending on the energy. Therefore, the EXAFS technique is highly sensitive to the local atomic structure. . In addition, because the EXAFS signal is observed close to the absorption edge, EXAFS is also element selective.

The validity of the Kronig short-range-order theory was largely substantiated by Sayers *et al.* [11], who developed a quantitative parametrization of EXAFS that has become the standard for much current work:

$$\chi(k) = \sum_i N_i \frac{|f(k)|}{kR^2} \sin(2kR + 2\delta_c + \phi) e^{-2R/\lambda(k)} e^{-2\sigma^2 k^2}$$

Eq. 2.10

Where, R the interatomic distances, k is the wave vector, N_R is the coordination number (or number of equivalent scatterers), and σ is the temperature dependent fluctuation in bond length, which can also include effects due to structural disorder. The $|f(k)|$ is the backscattering amplitude, and δ_c is central-atom partial-wave phase shift of the final state, and $\lambda(k)$ is the energy-dependent EXAFS mean free path.[12] The phase factor Φ reflects the quantum-mechanical wavelike nature of the backscattering.

Among many techniques which allow obtaining the EXAFS signal, we chose the fluorescence method with the grazing angle incident, described in Figure 2.8. The X-ray incident angle was equal to 0.6° and the detector was placed close to the sample and in the orbital plane of synchrotron x-rays. X-ray fluorescence is the emission of characteristic "secondary" (or fluorescent) x-ray from a material that has been excited by bombarding with high-energy x-rays. After excitation of an atom one electron can be ejected from the core level, and can be follow by the relaxation of another electron, from the superior levels, emitting one photon (or fluorescence) and also emitting another electron (Auger electron).

Among EXAFS methods the fluorescence detection presents several advantages: a large sensitivity and a high signal to noise ratio because the signal uniquely comes from the excited element. The signal to noise ratio is even enhanced by using an energy selective detector. In the

case of Fe, the threshold energy is 7.12 keV, but the Fe fluorescence has the energy equal to 6.9 keV, so the detector count the photons only with energy equal to 6.9 keV, and the incident x-ray in the sample vary from 7.0 to 7.8 keV (see Figure 2.13). Given the samples thickness employed in this work, we worked with a grazing angle to have a depth x-ray penetration comparable to the sample thickness, in the order to increase the measurement sensibility.

b) Experimental data analysis:

Once the absorption spectrum is experimentally collected, the EXAFS spectra have to be extracted. The background before (μ_0) and after (μ_1) of absorption edge is subtracted by using the equation Eq 2.11, and is represented in the Figure 2.13.

$$\chi(k) = \frac{\mu(k) - \mu_1(k)}{\mu_1(k) - \mu_0(k)}$$

Eq. 2.11
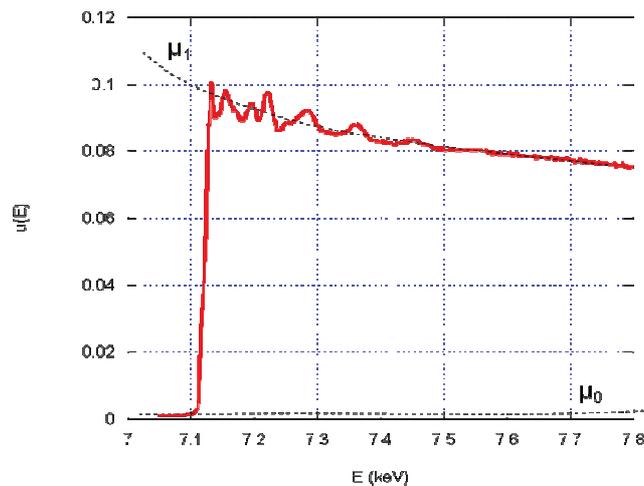
Figure 2.13 – Raw X-ray absorption spectrum of an Fe/Au(111) layer. The EXFAS signal is obtained by removing μ_0 and μ_1 from the experimental result.

(a) (b)
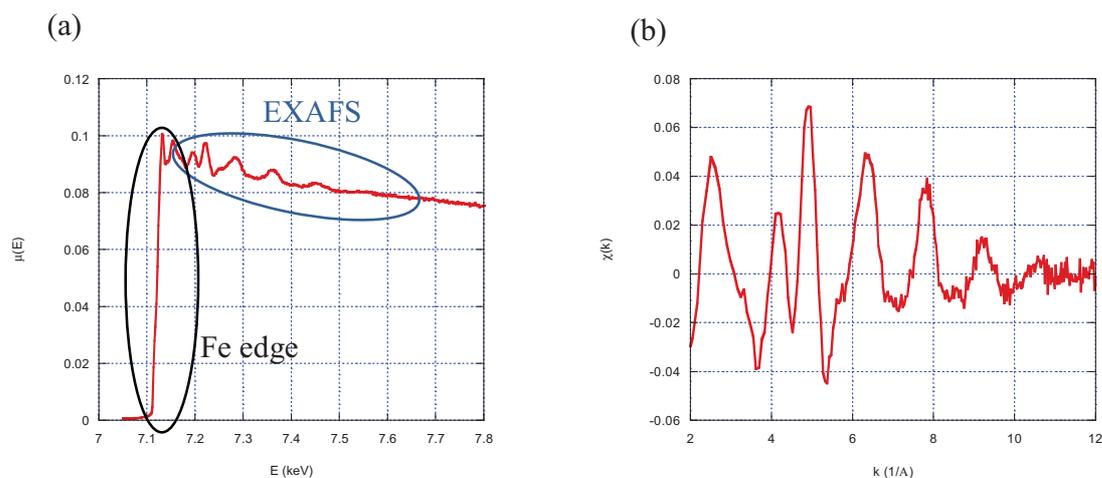
Figure 2. 14 –The relationship between (a) the x-ray absorption coefficient μ(E) with E in keV at the threshold of Fe, as measured, and (b) χ(k) after treatment of (a) spectrum, for a 5 ML Fe *K* edge sandwiched by Au.

The experimental spectrum is compared with theoretical ones, calculated using FEFF software.[13] FEFF allows one to determine χ(k) for a given atomic structure. In other words χ(k) is calculated by taking into account for the position (bond length, angles, number of neighbours etc. which are input parameters) and the nature (atomic number) of all atoms surrounding the target (emitting) atom. FEFF also accounts for thermal (or atomic) disorder and the polarization of the impinging x-ray beam. Given the large number of fitting parameters, we considered the crystal structure derived from XRD in order to reduce the number of parameters. The software allows also calculating the spectrum of a mixture of two phases (adding a supplementary phase would not significantly improve the fit). We hence obtain information about the crystallographic phase composing the layer, disorder, the number and distance of next nearest neighbours (the last parameters are sensitive to eventual lattice distortion).

2.4 Magneto Optical Kerr Effect Measurements (MOKE)

Magneto Optical Kerr Effect (MOKE) is widely employed to study the magnetic properties of thin film. Other technique may also be used, as for example: Alternative Gradient Field Magnetometer (AGFM), Superconducting Quantum Magneto Devices (SQUID) magnetometry. However, the time necessary for acquiring a hysteresis loop is much too long,

which make them more suited for *ex-situ* measurements. Indeed, due to the relatively simple MOKE setup, it but MOKE is possible to measure the magnetic properties *in-situ*.

2.4.1 MOKE

There are three different types of MOKE experiments geometry: polar, transverse, and longitudinal. In the Polar MOKE configuration, the magnetic field is perpendicular to the sample surface and parallel to the reflection plane (see Figure 2.15 (a)). In the Longitudinal MOKE configuration the magnetic field is parallel to the sample surface and parallel to the reflection plane (see Figure 2.15 (b)). In the Transverse MOKE configuration the magnetic field is in the sample surface and perpendicular to the reflection plane (see Figure 2.15 (c)).The PMOKE and LMOKE were used in this study.
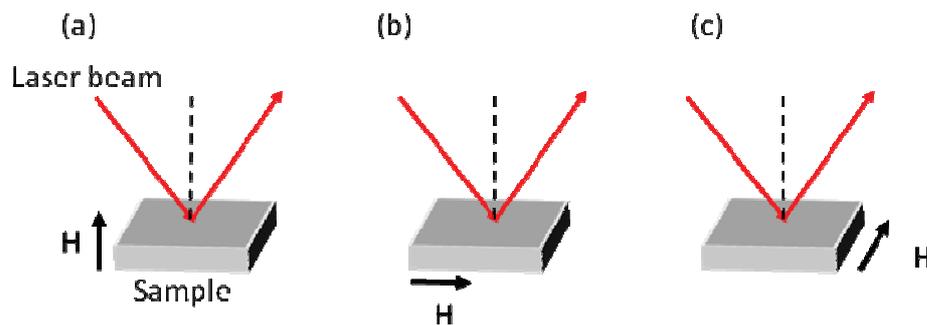
Figure 2.15 - Three possible MOKE configurations: (a) Polar MOKE, with the magnetic field perpendicular to the sample surface and parallel to the reflection plane. (b) Longitudinal MOKE the magnetic field is parallel to the sample surface and parallel to the reflection plane, and (c) Transverse MOKE the magnetic field is in the sample surface and perpendicular to the reflection plane.

After interaction between a polarized beam light and the magnetized sample, the polarization is altered due to magnetic orientation of sample. This effect is called Faraday Effect in the case of transmitted light and Kerr effect in the case of reflected light. Both effects are related to the spin-orbit interaction, and a rigorous treatment of both effects requires the use of perturbation theory. Conservation of angular momentum dictates that an incident (right or left) circular polarized light generates an electron population with non-zero orbital angular momentum in a material with opposite direction, and each polarization therefore produces a

contribution to the orbital angular momentum to having an opposite sign. A magnetic field gives rise to a spin-polarization along the magnetic field direction and the spin orbit interaction then leads to an energy contribution for the two circular polarizations having different amplitude but with opposite sign. This leads to right and left circular polarizations having different refractive indices in the material. If plane polarized light is incident on a magnetic material, it should be considered as sum of right and left circularly polarized beams which propagate through the material at different speeds. When they emerge, these two beams recombine but the phase-lag between them implies that the emerging beam has a rotated plane of polarization.

In an isotropic material the dielectric tensor becomes

$$\varepsilon = \varepsilon_0 \begin{pmatrix} 1 & iQ_z & -iQ_y \\ -iQ_z & 1 & iQ_x \\ iQ_y & -iQ_x & 1 \end{pmatrix} \qquad \text{eq. 2.12}$$

Where $\mathbf{Q} = (Q_x, Q_y, Q_z)$ is known as the Voigt Vector which is aligned with the magnetic field and has a magnitude which depends on the material. The Voigt Vector can be measured experimentally [14] or can be determined from experimental measurements [15]. The tensor leads to the two circularly polarized normal modes which have dielectric constants

$$\varepsilon_\pm = \varepsilon \left(1 \pm \vec{Q} \cdot \hat{k} \right) \qquad \text{eq. 2.13}$$

where $\mathbf{k}$ is the unit vector in the light propagation direction and the two signal refer to two circular waves. The circular modes travel with different velocities and attenuate differently in the magnetic material, this phenomena can be described by the reflective index n as (with the relation $n^2 = \varepsilon$)

$$n_\pm = n \left(1 \pm \frac{1}{2} \vec{Q} \cdot \hat{k} \right) = \sqrt{\varepsilon} \left(1 \pm \frac{iQ_z}{2\varepsilon} \right). \qquad \text{eq. 2.14}$$

for the perpendicular incident light on the surface. The emerging waves therefore combine to yield a rotated axis of polarization and also an ellipticity, the different attenuations lead to the polarization of the light that emerges being slightly elliptical.

The Kerr rotation angle (θ_k) can be estimated for multi layer samples. In our case, and for *in-situ* experiments four layers have to be taken into account: solution, magnetic thin film, 33 ML of Au(111) and Si(111). Visnovsky et al. demonstrated in detail how to calculate θ_k for multilayer system[14]. The adapted formula for our case is

$$\theta_k \approx \frac{4\pi}{\lambda} \frac{t_M n_{solution} n_M^2 Q_z}{n_{solution}^2 - n_{Au}^2} \frac{r_{solution/Au}\left(1 + r_{Au/Si}e^{-i4\pi n_{Au}t_{Au}/\lambda}\right)^2}{\left(1 + r_{solution/Au}r_{Au/Si}e^{-i4\pi n_{Au}t_{Au}/\lambda}\right)\left(r_{solution/Au} + r_{Au/Si}e^{-i4\pi n_{Au}t_{Au}/\lambda}\right)} \qquad \text{eq. 2.15}$$

Where $n_{solution}$, n_M and n_{Au} is the index of solution, the magnetic material (M = Fe or Ni or FeNi) and Au, respectively, $r_{solution/Au}$, $n_{Au/Si}$ is the reflection coefficient of the interface solution/Au and Au/Si, t_M is the thickness of deposited magnetic metal and λ the wavelength ($\lambda = 633$ nm).

2.4.2 In situ MOKE

For *in situ* MOKE measurements the sample is installed in an electrochemical cell, which scheme is presented in Figure 2.16. Its dimensions are: height 22 mm, width 40 mm and depth 5 mm. The cell thickness is a compromise between two constraints: (i) it must be as thin as possible to minimize the MOKE signal of water, (ii) it must be thick enough to avoid electrochemistry in thin layer geometry. A good compromise is a thickness of 5 mm with a continuous flow of the electrolyte. The volume of the cell is 2 mL. Our counter electrode (Pt wire of diameter 0,5 mm) is placed at the outlet of the cell to pump eventual reaction by products that could contaminate the sample surface. The solution flow is due to gravity forces; the flux is about 2.0 mL/min. With this system it is further possible to change the solution composition in the course of a measurement, for instance to deposit a capping film.
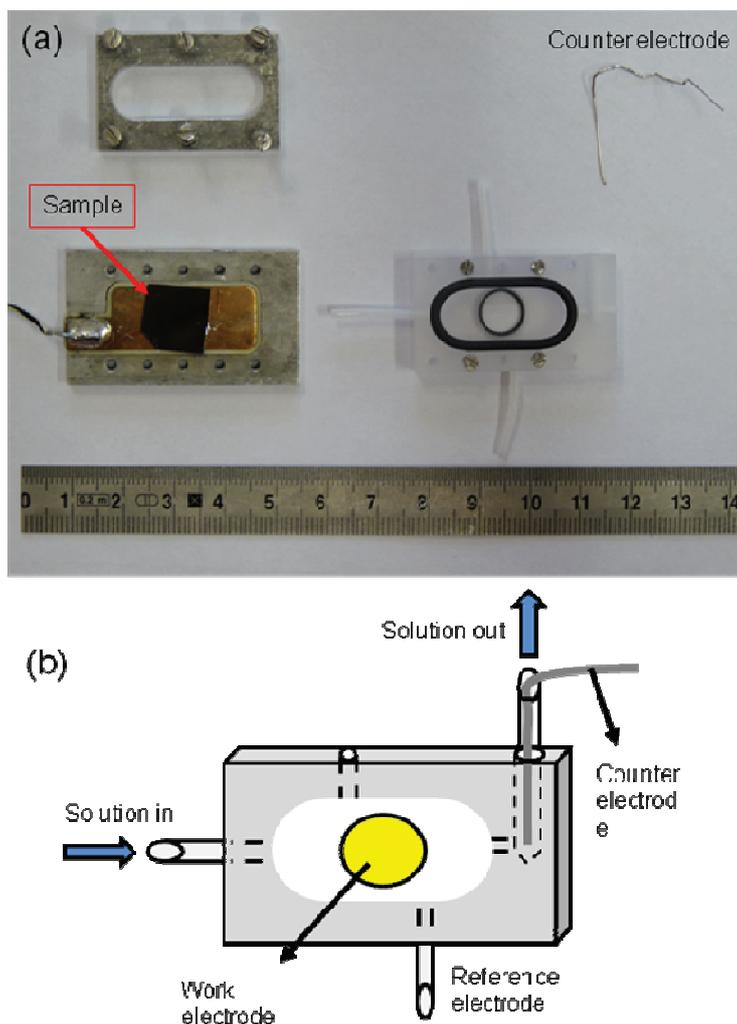
Figure 2.16 – (a) Photo and (b) the schema of *In situ* MOKE electrochemical flow cell. The counter electrode is in the outlet channel to eliminate contaminations.

2.5 Preparation of Au(111)/Si(111) substrate.

The Au(111)/Si(111) substrate is obtained by electrochemical deposition, and is the main substrate used in this thesis. Here we briefly describe the substrate preparation, for more details see ref [16,17]. The samples were cleaved from the 5 inch commercial silicon (111) wafer (Siltronix, France), with one side polished, in to samples of dimension 1.2 x 1.2 cm^2. The silicon has a miscut of $\alpha = 0.2°$ towards (11-2) (see Figure 2.17). Given the distance between successive (111) planes of 0.31 nm, the terrace width is expected to be equal to 88,8 nm.
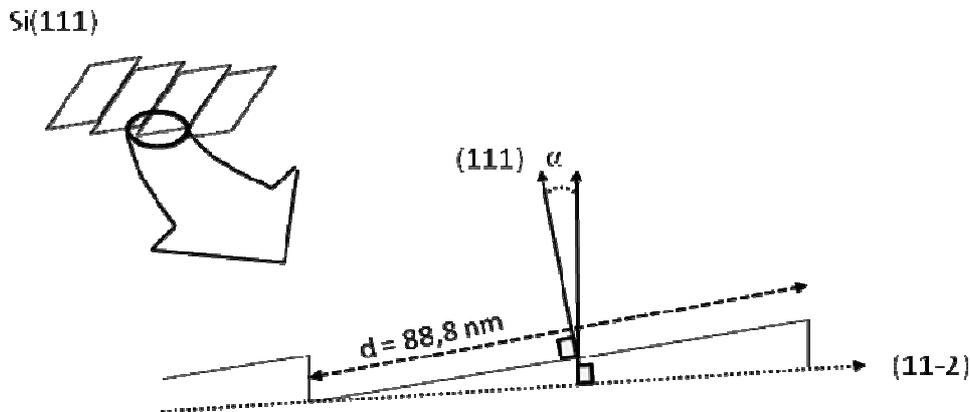
Figure 2.17 - Silicon miscut representation for an angle α equal to 0,2°.

Before gold deposition, the silicon sample is cleaned in a boiling Pirana solution (2:1 H_2SO_4:H_2O_2). After rinsing in ultrapure water, the samples are etched in 40 % NH_4F solution with a few grams of ammonium sulfite ((NH_4)$_2SO_3$·H_2O) to remove dissolved oxygen and therefore terrace pitting[18]. After another ultrapure water rinse, the Si(111) surface is H terminated, and is ready for gold deposition. The electrochemical gold deposition is performed at -2 VMSE in an aqueous solution containing:

$$0.1 \text{ M } K_2SO_4 + 1 \text{ mM KCl} + 1 \text{ mM } H_2SO_4 + 0.1 \text{ mM HAuCl}_4$$
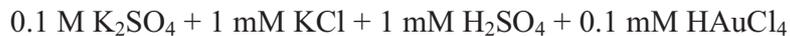
the pH of this solution is 3.5 – 4. Au deposition is performed with a rotating working electrode (1750 rpm). The counter electrode is Au. The reference electrode is in contact with the solution by a salt bridge containing 0.1 M of K_2SO_4.

Figure 2.18 (a) shows the Kel F cylinder with an internal metallic contact used as a sample holder (the Ohmic contact between the metallic contact and the sample is made by InGa) and Figure 2.18 (b) shown the front view of sample holder with electrochemical tape and the exposed Si surface. Once mounted, the sample is immersed in the solution. With a deposition rate of 0,22 Mono-Layers per second (ML/s), the sample stays immersed in the electrochemical solution for 150 seconds. 33 Au ML are deposited. Figure 2. 19 (a) shows an Atomic Force Microscope (AFM) image of the Si(111) surface just after etching and (b) the surface of 33 ML of Au on the etched Si surface. The Si(111) surface presents the expected vicinal structure with uniformly separated parallel steps which height is close to 0.3 nm. The Au deposit (image b) present a long range modulation associated with screw dislocation growth. Monatomic steps (.23

nm) are visible in this image, in agreement with the (111) orientation of the film derived from X-ray diffraction. Note the absence of grain boundaries in this film. More explanation about Au growth may be found in refs. [16,17].
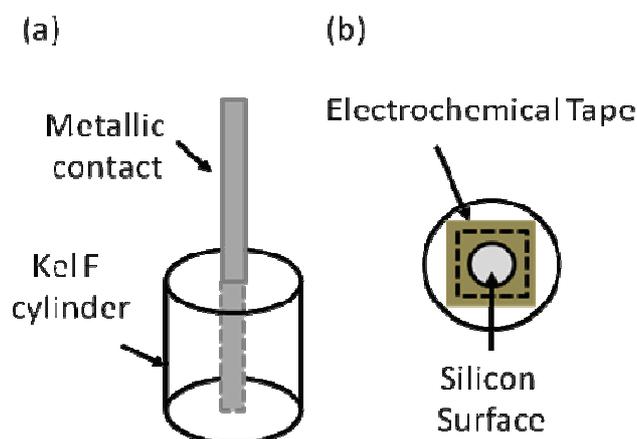
Figure 2.18 – (a) Scheme of the sample holder. The metallic rod, which also serves as electric contact, is inserted into a Kel F cylinder. (b) Front view of the mounted sample after: the edges of the Si sample are protected with an electrolytic scotch tape in order to expose the polished Si surface only. A back ohmic contact is formed between the rear side of the sample and the stainless steel rod.
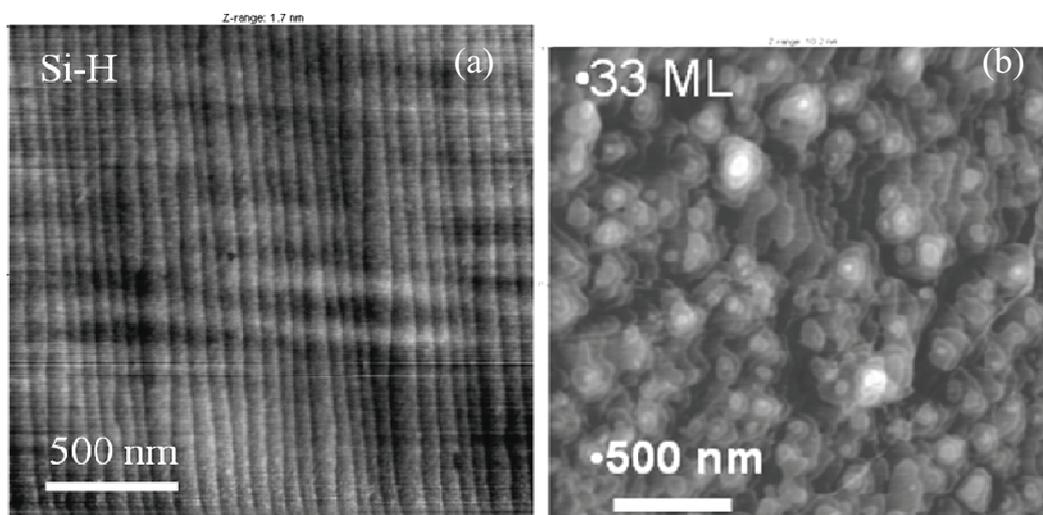
Figure 2. 19 - (a) AFM image showing the topography of the H-terminated Si(111) surface before Au deposition; (b) Same as (a) after deposition of a 33 ML – thick Au film (U = -2 V).

Au/Si(111)x-ray diffraction:

Figure 2.20(a) shows the x-ray diffraction of the single crystal of Si(111), with detector angles set to $\theta_i = 0.6^o$, $\delta = 9.353^o$, and $\gamma = 26.98^o$, to observe the crystallographic planes (11-1), (1-11) and (-111). Fig. 2.20b is the XRD diagram of a 33 ML Au(111) layer on /Si(111), with detector angles set to $\theta_i = 0.6^o$, $\delta = 12.466^o$, and $\gamma = 36.39^o$, to study the crystallographic planes (11-1), (1-11) and (-111) of gold. For the perfect single crystal (Figure 2.20 (a)) only a presence of three peaks of diffraction, provide by the family planes [-111], is observed with the same intensity. These three diffracted peaks are given by the threefold geometry of fcc (111) surface direction. X-ray diffraction of Au provide six peaks with distinct three largest peaks and three smaller peak, for the same family plane [-111], i.e. three smaller peak which follows the Si lattice orientation and the other three peak which has the lattice orientation turned 180° in relation to the Si crystal orientation. These observations are fully consistent with previous works.[19],[17] It is out of the scope of this thesis to explain all the details about AU/Si growth and structure. As a whole Fig. 2.20 indicate that the Au buffer layer is in excellent epitaxy with Si(111).
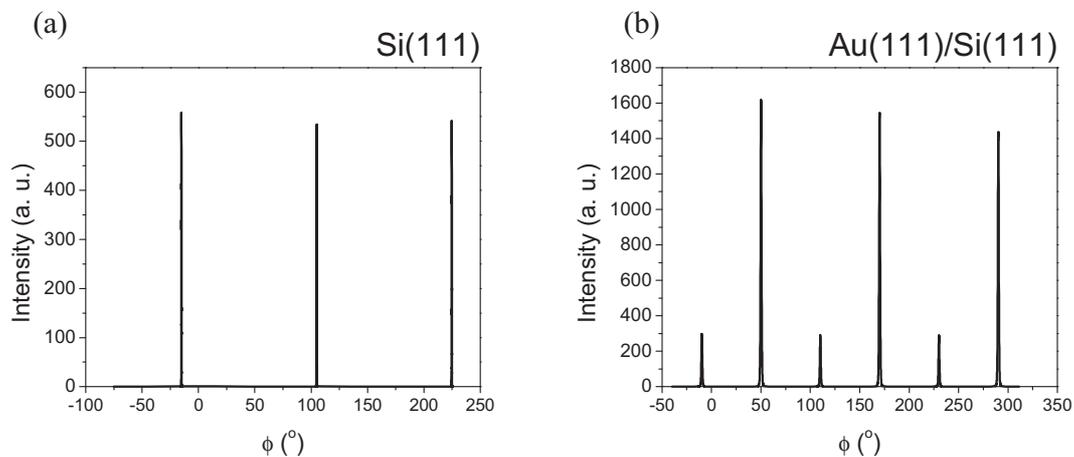
Figure 2.20 - X-ray diffraction diagram (Φ-scans) of (a) Si(111) wafer and (b) Au(111)/Si(111) electrodeposited at -2 VMSE. The incident angle is 0.6°.

2.6 Bibliography:

[1] Allen J. Bard, Faulkner, Larry R., *Electrochemical methods : fundamentals and applications*. (New York, 1980), p.718 p.

[2] D. M. Kolb, "Reconstruction phenomena at metal-electrolyte interfaces," Prog. Surf. Sci. **51** (2), 109-173 (1996).

[3] "CRC handbook of chemistry and physics," (1977).

[4] J. O'M Bockris and Shahed U. M. joint author Khan, *Quantum electrochemistry / John O'M. Bockris and Shahed U. M. Khan*. (Plenum Press, New York :, 1979).

[5] H. Brune, in *Encyclopedia of Materials: Science of Technology, Sect. 1.9, Physical Properties of Thin Films and Artificial Multilayers*

edited by K. Samwer (Pergamon press, 2001), pp. 3683-3693; E. Budevski, G. Staikov, and W. J. Lorenz, *Electrochemical phase formation and growth*. (VCH, Weinheim, 1996); T. Michely and J. Krug, *Islands, Mounds, and Adatoms: Patterns and Processes in Crystal Growth Far from Equilibrium*. (Springer, Berlin, 2004).

[6] K. Krug, J. Stettner, and O. M. Magnussen, "In Situ Surface X-Ray Diffraction Studies of Homoepitaxial Electrochemical Growth on Au(100)," Phys. Rev. Lett. **96** (24), 246101-246104 (2006).

[7] Samuel K. Allison Arthur H. Compton, *X-rays in theory and experiments*. (1950).

[8] L. G. Parratt, "Surface Studies of Solids by Total Reflection of X-Rays," Physical Review **95** (2), 359 (1954).

[9] A. Guinier, *Théorie et technique de la Radiocristallofgraphie*. (Paris, 1964).

[10] S. Brauer, G. B. Stephenson, and M. Sutton, "Perfect Crystals in the Asymmetric Bragg Geometry as Optical Elements for Coherent X-ray Beams," Journal of Synchrotron Radiation **2** (4), 163-173 (1995).

[11] Dale E. Sayers, Edward A. Stern, and Farrel W. Lytle, "New Technique for Investigating Noncrystalline Structures: Fourier Analysis of the Extended X-Ray—Absorption Fine Structure," Phys. Rev. Lett. **27** (18), 1204 (1971).

[12] D. C. Koningsberger and R. Prins, *X-Ray Absorption, principles, applications, techniques of EXAFS, SEXAFS abd XANES*. (John Wiley & Sons, 1976).

[13] J. J. Rehr, J. Mustre de Leon, S. I. Zabinsky et al., "Theoretical x-ray absorption fine structure standards," Journal of the American Chemical Society **113** (14), 5135-5140 (2002); J. J. Rehr and R. C. Albers, "Theoretical approaches to x-ray absorption fine structure," Reviews of Modern Physics **72** (3), 621 (2000).

[14] Å ViÅ¡Å^ovskÃ½, M. Nývlt, V. Prosser et al., "Polar magneto-optics in simple ultrathin-magnetic-film structures," Physical Review B **52** (2), 1090 (1995).

[15] Z. Q. Qiu and S. D. Bader, "Surface magneto-optic Kerr effect," Review of Scientific Instruments **71** (3), 1243-1255 (2000).

[16] P. Prod'homme, F. Maroun, R. Cortes et al., "Electrochemical growth of ultraflat Au (111) epitaxial buffer layers on H-Si (111)," Appl. Phys. Lett. **93** (17), 3 (2008).

[17] S. Warren, P. Prod'homme, F. Maroun et al., "Electrochemical Au deposition on stepped Si(1 1 1)-H surfaces: 3D versus 2D growth studied by AFM and X-ray diffraction," Surface Science **603** (9), 1212-1220 (2009).

[18] Philippe Allongue, Catherine Henry de Villeneuve, Sylvie Morin et al., "The preparation of flat H-Si(111) surfaces in 40% NH4F revisited," Electrochimica Acta **45** (28), 4591-4598 (2000).

[19] P. Prod'homme, F. Maroun, R. Cortes et al., "Electrochemical growth of ultraflat Au(111) epitaxial buffer layers on H--Si(111)," Applied Physics Letters **93** (17), 171901 (2008); P. Prod'homme, F. Maroun, R. Cortes et al., "Preparation, characterization and magneto-optical investigations of electrodeposited Co/Au films," J. Magn. Magn. Mater. **315** (1), 26-38 (2007).

Chapter 3

Electrochemical growth and *in situ* magnetism

of ultrathin film Fe/Au(111)

3.1 Introduction

Theoretical works[1] predicted that the magnetic moment per atom in iron strongly varies with the atomic volume. This group found a complex behavior for fcc iron, with either an antiferromagnetic state or a HS phase upon lattice expansion and a HS phase upon contraction (see related data in the review paper published by Himpsel and co-authors[2]). Iron appears therefore to be a complex material from a magnetic viewpoint. These results have motivated numerous experimental studies in which iron has been deposited in the form of an epitaxial ultrathin film to modify its crystal structure (fcc vs bcc) and lattice parameter by deposition on single crystal surfaces with different orientations and lattice constants.
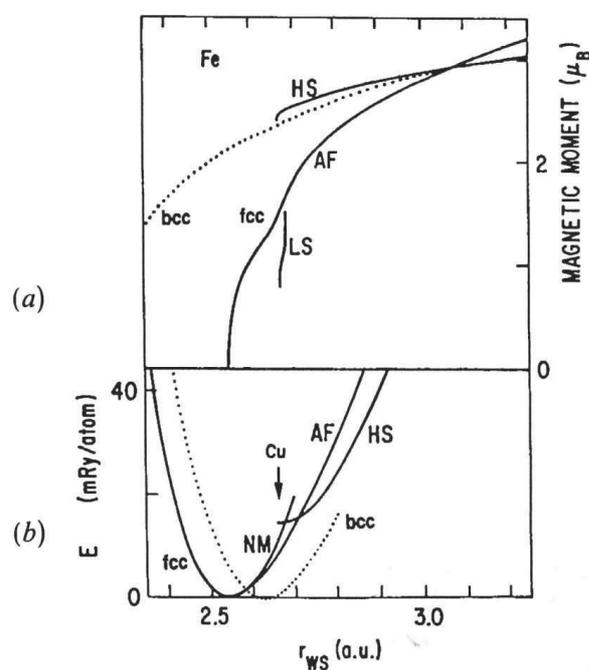

Fig. 3.1 - Magnetic moment and total energy versus atomic distance (1 a. u. = 0.53 Å) for iron in a fcc phase (solid line) and bcc phase (dashed line) calculated by first-principles for different magnetic configuration; curve NM = non-magnetic, HS = high-spin ferromagnetic, AF = anti ferromagnetic, LS = low-spin ferromagnetic. Ref. [2].

A literature survey reveals that iron was deposited on Cu(111)[3,4] and (001)[5], Pt(111)[6,7,8], Au(111) [9-13] and (100)[14], W(110) [15,16,17]. Most of the cited studies employed thermal deposition in the UHV. Only a few ones employed pulsed laser deposition (PLD) and compared the impact of the growth method[3,18,19]. On (111) substrates, results showed that pseudomorphic fcc (111) iron is initially formed before a structural phase transition occurs and bcc Fe(110) appears. Different growth models were proposed. From a magnetism viewpoint, results also showed that the moment per atom, the anisotropy of epitaxial Fe layer crucially depends on the surface symmetry, the surface lattice parameter and, for a given system, on the growth method.

There are surprisingly only few studies of *pure* iron electrodeposition although while there is a vast literature about electrodeposition of iron containing alloys. Pure iron thin films were deposited on semiconductors (Si and GaAs)[20,21,22]. Ultrathin films were electrodeposited on Cu(001)[23] and Au(111).[24,25],[26] The last studies provided STM observations as well as magnetic characterizations. On Cu(001) it was found that Fe growth relatively 2D and that the first atomic layers are probably perpendicularly magnetized since no LMOKE signal was detected.[23] On Au(111), a layer by layer growth was observed by *in si*tu STM[26] and a clear spin reorientation transition (out of plane → in plane) was found around 2 ML from AGFM measurements[24]. Structural information were however missing.

This chapter presents a combined structural and magnetic study of iron electrochemical growth on Au(111) using ex situ XRD and EXAFS, *in situ* STM and *in situ* PMOKE and LMOKE measurements.

3.2 Growth mechanisms and structure

3.2.1 Voltammetry and growth rate

Cyclic voltammetry (CV) was performed as explained in section 2.1.2 figure 3.2 presents a typical CV of a Au(111)/Si(111) electrode recorded in a 0.5 mM FeSO$_4$ solution in 0.1 M K$_2$SO$_4$ + 1 mM H$_2$SO$_4$ + 1 mM KCl as supporting electrolyte. This composition corresponds to a modified Watts bath containing. Its pH is 3-4. Starting from -0.2 V the potential was scanned negatively towards -1.5 V before being reversed and scanned back up to -0.2 V. Several cathodic (i.e. negative) and anodic (i.e. positive) peaks of current, hereafter labeled C$_i$/A$_i$ can be identified (for all of Nernst potential sees Table 2.1):

- Peak C1 at -0.65 V is associated to the oxygen reduction on Au(111) ($O_2 + H_2O + 2e^- \rightarrow HO_2^- + OH^-$). The solution was not deareated.

- Peak C2 at -1.15 V is assigned to the reduction of protons in solutions ($H^+ + e^- \rightarrow \frac{1}{2} H_2$) also called hydrogen evolution reaction (HER). In fact a CV measured in the supporting electrolyte (i.e. in the absence of iron species) presents the same peak C2.

- Peaks C3 (-1.44 V) is related to iron deposition ($Fe^{2+} + 2e^- \rightarrow Fe^0$) and peak A1 (-1.2 V) to the dissolution of the iron film ($Fe^0 \rightarrow Fe^{2+} + 2e^-$) which had been deposited during the potential sweep. A simple way to verify this assignment is changing the cathodic end of the CV. Making it more positive than -1.35 V lets disappear peak A1. This value approximately corresponds to the onset potential for Fe nucleation on Au(111).
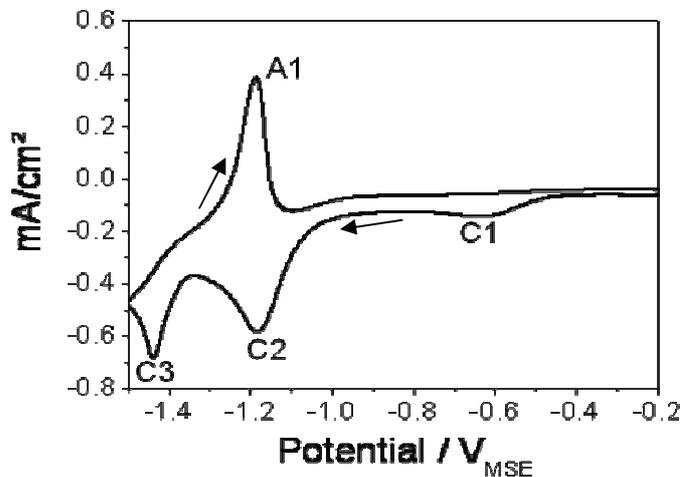
Figure 3.2: CV of a Au(111)/Si(111) electrode in a Fe 0.5 mM solution. The potential was scanned from -0.2 V towards -1.5 V and back to -0.2 V at a rate of 20 mV/s. See text for the assignment of peaks. The reference electrode is a mercury sulfate electrode (MSE).

In practice, deposition is performed under potentiostatic condition, i.e. at a fixed potential, because this method enables controlling the nucleation and growth modes [27]. The entire potential program, which will be used in MOKE experiments, is depicted in figure 3.3. It consists of 3 phases which aim at depositing and determining the average film thickness t_M (M = Fe, Ni):

- In phase I a step of potential from -0.2 V to $U_{Dep} < -1.35$ V to deposit the film. The deposition time is adjusted to obtain the desired thickness.

- In phase II, the potential is stepped to -1.3V for 5s. This is to rapidly stop the deposition. This potential, hereafter called *stabilization* potential, must be carefully chosen such that not only the deposition is stopped but also that no dissolution occurs. The value of the

stabilization potential depends on the metal which is deposited and its determination is particularly important in MOKE experiments where the layer thickness must sometimes be kept constant for several minutes.

- In phase III, the potential is swept from the stabilization potential (here -1.3 V) to -0.2V to strip off the deposited film.

In the present experiment of Fe deposition, U = - 1.5 V. Therefore H^+ are reduced together with Fe^{2+} cations (see figure 3.2). Since both species are in nearly the same concentration (0.5 mM) the fast decay of the electrochemical current mainly reflects the electrochemical consumption H^+ close to the surface. This depletes the solution in protons and the associated current decreases. The reaction becomes limited by transport of protons from solution towards the surface. Of course, the same process is occurring in parallel for Fe^{2+}. However the associated current is smaller than the one associated with protons because the later diffuse much faster than Fe^{2+}. As a consequence it is not possible to determine t_M from the measure of the cathodic charge. The value of t_M may however be obtained by integrating the anodic charge by assuming that the current is uniquely arising from the reaction $Fe^0 \rightarrow Fe^{2+} + 2e$ [27]. The conversion anodic charge to t_M is obtained using Faraday's law:

$$t_M = \frac{QM}{zF\rho}$$
(eq. 3.1)

where t_M is the *average* thickness, Q_A is the charge exchanged (C/cm²), M is the molar mass (g/mol), z is the valence number (z = 2 for fe and Ni), F = 96500 C is the Faraday's constant and ρ is the density of the metal considered (g/cm³). Table 3.1 lists the anodic charge corresponding to one monolayer of the different metals deposited in this work. Layers are assumed to be relaxed. Different orientations are considered for iron.

Table 3.1: Value of the anodic charge Q_A corresponding to the dissolution of 1 ML of various metallic layers.

metal	Charge Q_A (mC/cm^2)
Ni(111)	0.59
γ-Fe(111)	0.59
α-Fe(110)	0.56
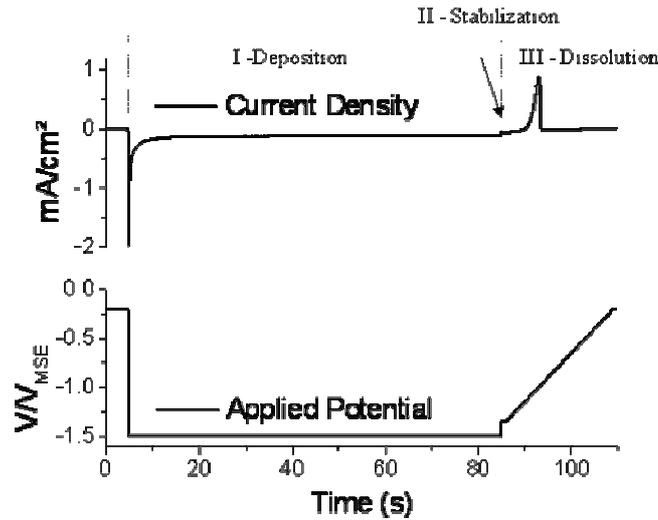
Figure 3.3: Potential program and corresponding electrochemical current transient measured in the case of Fe/Au(111) deposition. Phases 1 – 3 refer to deposition (U = -1.5 V), stabilization (U = -1.3 V) and dissolution of the film (ramp of potential, sweep rate 10 mV/s). The *average* metal thickness is determined from the anodic charge measured under the peak in phase 3 using Faraday's law (Eq. 3.1)

Figure 3.4 plots the variations of t_{Fe} as a function of deposition time at various deposition potentials U = -1.35, -1.4, -1.5 and -1.6 V. The potential dependence of other plots expresses that the rate of electrochemical reduction of Fe^{2+} cations exponentially increases towards more negative potentials (see Eq. 2.3 in Chapter 2.1.2). This graph confirms also that U = -1.35 V is close to the onset potential for iron growth, since the thickness never exceeds 0.1 ML. The fact that plots overlap for U < -1.5 V, means that the reaction becomes ultimately limited by mass transport of Fe^{2+} in solution at sufficiently negative potentials. This is again in agreement with expectations. One nevertheless notices in this case that the plots present two slopes, i.e. the growth rate change in the course of deposition. The crossover between the two deposition regimes, obtained by intersecting the two straight lines, corresponds to a critical iron thickness t_{Fe}^c ~ 1 ML. A similar phenomenon is observed with Ni (see later) and was also reported Co/Au(111) growth [27]. In the later case t_{Co}^c ~ 2 ML was assigned to the fact that cobalt growth begins with the formation of a biatomic layer. STM imaging will show (see section 3.2.3) that t_{Fe}^c ~ 1 ML is associated with the formation of one complete iron monolayer prior to multilayer growth.

To summarize this section, iron deposition at U < -1.5 V is limited by mass transport. Between 0 and 1 ML, the growth rate is 0.2 ML/s and above 1 ML it is 0.05 ML/s. These values are small enough to allow us controlling the final thickness to a fraction of ML with sufficient precision. For U = -1.4 V and -1.35 V, the growth rate is 0.018 ML/s and 0.0015 ML/s, respectively.
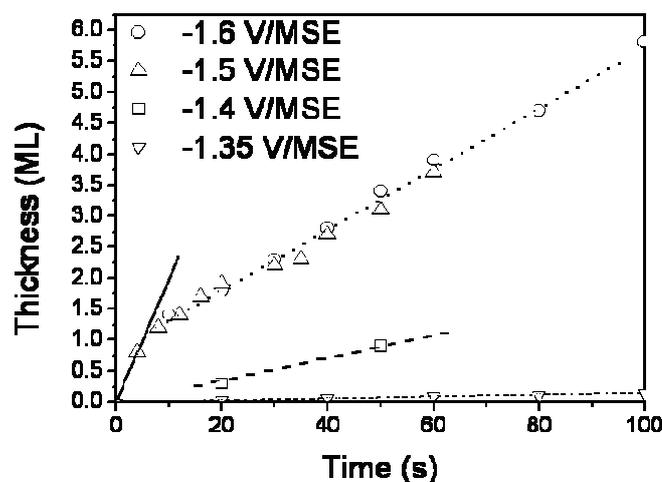
Figure 3.4: Time dependence of average thickness of for Fe/Au(111) layer deposited using the method described in Fig. 3. U = -1.35 V (down triangle), -1.4 V (square), -1.5 V (up triangle) and -1.6 V (circles).Note the potential dependence of plots for U > -1.5 V. For U < -1.5 V growth becomes limited by mass transport in solution. A 0.5 mM Fe solution concentration is used.

3.2.2 Structural characterizations:

a) In situ STM:

The electrochemical growth Fe/Au(111) has been studied by STM in the past in our group [28,29]. We present and reexamine below some past observations before showing a few new and complementary observations which were acquired by Corentin Cougaud during his stay in the group in the framework of his practical work at IFIS (Orsay).

Figures 3.5a-b are two *in situ* STM images (1200 Å x 1400 Å) acquired while stepping the sample potential from -0.8 V to -1.5 V in the course of the first image. The slow tip scanning direction is indicated next to the images. Before deposition (lower part of image a), the Au(111) present an imperfect 22x√3 surface reconstruction, which is however useful to determine the in plane crystallographic directions. The figures in images are the local thickness of the layer in ML. It should be mentioned the tip potential was transiently shifted negatively that to allow iron deposition and minimize tip shielding. This explains that the first few x-scans are not useable after the potential step. Clearly enough, however, image (a) gives evidence of the formation of an iron monolayer (see more detail below), composed of anisotropic features in the very initial stages (see examples highlighted by a few arrows),

which expand laterally and coalesce. The 1st ML is nearly complete at the top of image (a). Islands of the second Ml have also nucleated. In image (b) the growth of the 2nd atomic plane has considerably progressed and a few island of the 3rd ML are visible. As a whole these images indicate that Fe/Au(111) electrochemical growth is essentially a layer by layer process at this potential. Image (c) is a zoom of the topography image to highlight the presence of some lines of contrast across the topmost (i.e. 3rd) iron layer. Image (d) is an attempt to better evidence these low corrugation features by representing the derivative of image (c) along the x-scan. Arrows are outlining some of the above mentioned lines. The corrugation is less than 0.3 Å.
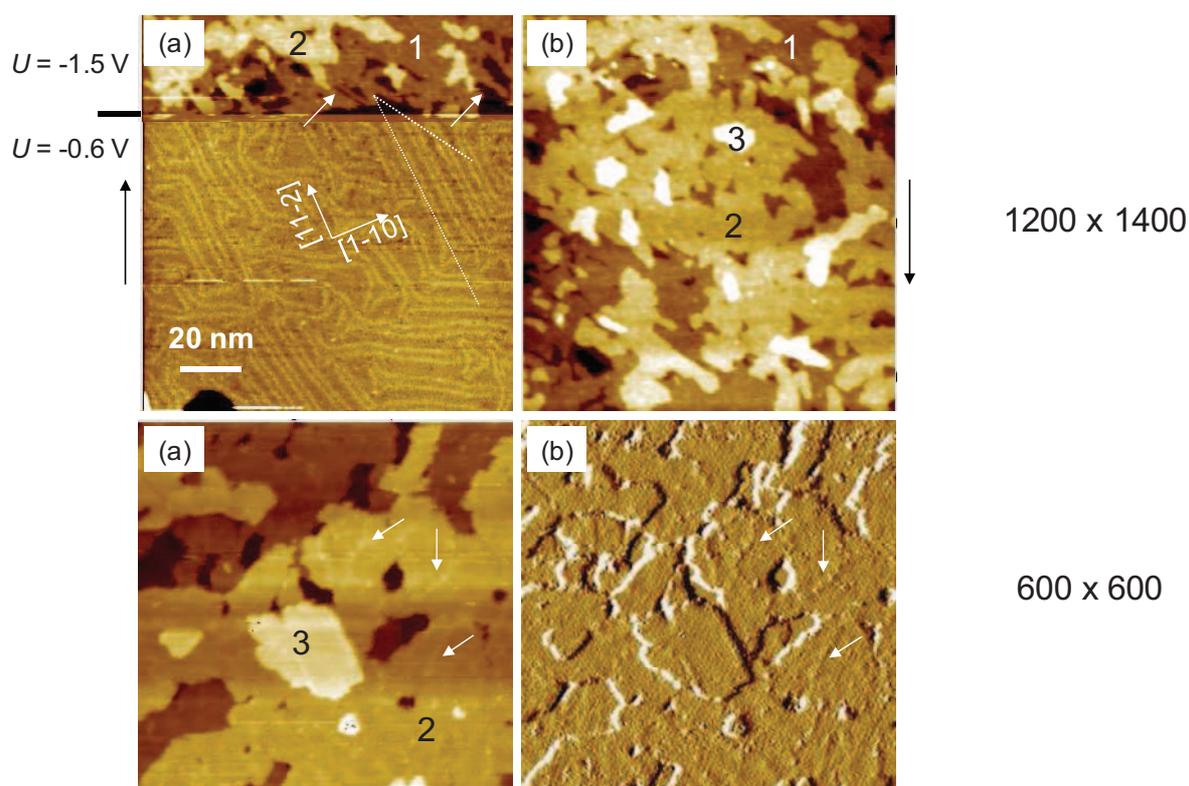
Figure 3.5: (a-b) Successive *in situ* STM images (1200 Å x 1400 Å) recorded while stepping the potential from -0.8 V to -1.5 V to initiate Fe growth on reconstructed Au(111). Arrows next to images indicate the slow tip scanning direction. Figures in images are the local thickness (in ML). The in plane Au(111) crystallographic directions are deduced from the reconstruction pattern. (c-d) Topography and differentiated images showing the absence of moiré pattern on the topmost iron layer. Notice however the presence of lines of very shallow corrugation (0.3 Å).

To study in greater details the structure of the first iron monolayer, the tip was retracted to reduce the shielding of the surface and approximately one monolayer deposited. Figure 3.6a shows the topography (840 Å x 840 Å) and the cross section of a Fe layer grown at a potential -1.55 V for 1.5s. The surface coverage is 0.7 ML. Figure 3.6b is showing the

dissolution of this layer at -0.6 V. At this potential (see figure 3.2) the dissolution is quite fast as it occurs in a few x-scans. These images call for several remarks:

- On average, the edges of the vacancy islands are oriented in preferred preferential directions with nearly 3 fold symmetry. Unfortunately the in plane crystallographic directions of the gold substrate could not be imaged.

- The STM height of the iron monolayer (figure 3.6b) is 2.6 Å (see cross section c).

- One notices a large density of nm-sized protrusions in the 1st Fe monolayer (figure 3.6a) and occasionally lines of contrast.

- Dissolution leaves *initially* a large density of nm-sized islands on the surface, which height is 2 Å (see cross section d). This suggests that they are mainly, if not totally, composed of gold since Fe is highly unstable at this potential. In support of this hypothesis, we noticed a mechanism of Ostwald ripening with a decrease of the islands density and an increase of the island size.
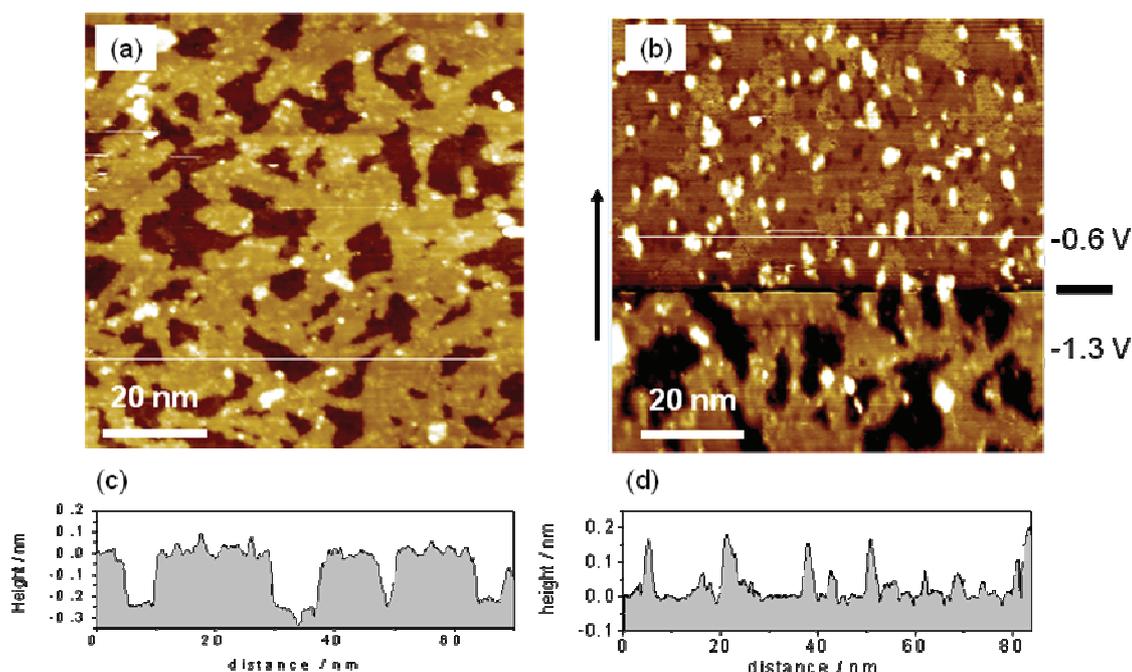
Figure 3.6: (a) *in situ* **STM images (840 Å x 540 Å) of 0.7 ML Fe film grown in 1.5 s at -1.55 V with the tip retracted. The film was stabilized at -1.3 V for imaging. (c) Cross section along the white line in (a) showing that the iron monolayer is ~ 2.6 Å high as measured with respect to Au(111). (b)** *in situ* **STM image (840 Å x 840 Å) showing the dissolution of the 0.7 ML Fe film shown in (a). The sample potential is -1.3 V in the lower part of the image and -0.6 V in the upper part. Note the presence of a large density of nm-sized islands after iron stripping. (d) Cross sections of the surface as marked on image (b).**

Figure 3.7 shows an iron deposit obtained at -1.3 V in 1s using the same procedure as for the previous figure. At this potential the film grows 3D because the islands are several atomic planes in height and it is difficult to resolve at the same time the substrate and the

deposit. In image (a) the image contrast is adjusted to resolve the complete topography and in image (b) it is adjusted to resolve the topography of the Au(111) surface. Its reconstruction pattern is severely disturbed. This is attributed this to the fact that this film was deposited a too short time after stripping of the preceding one (see figure 3.6). It is emphasized that the observed 3D growth is the result of the low applied potential and not of the Au(111) imperfect structure. In fact, deposition at -1.5 V on a perturbed Au(111) surface leads to a 2D layer as in figure 3.6. The cross sections (c and d) evidence that the height of the lower part of the central island is 6.6 Å with respect o the Au(111) surface. The height of additional atomic layers is 2Å. Here again, one notices a certain degree of anisotropy in the growth since the edges of the islands are aligned along 3 preferential directions. One also notices some lines of contrast, with a very shallow corrugation (<< 1 Å), on the topmost atomic plane of the central island (figure 3.7e). Similar features have been reported in the case of TD Fe/Pt(111) layers and assigned to the creation of misfit dislocations associated with partial strain relief.[8]
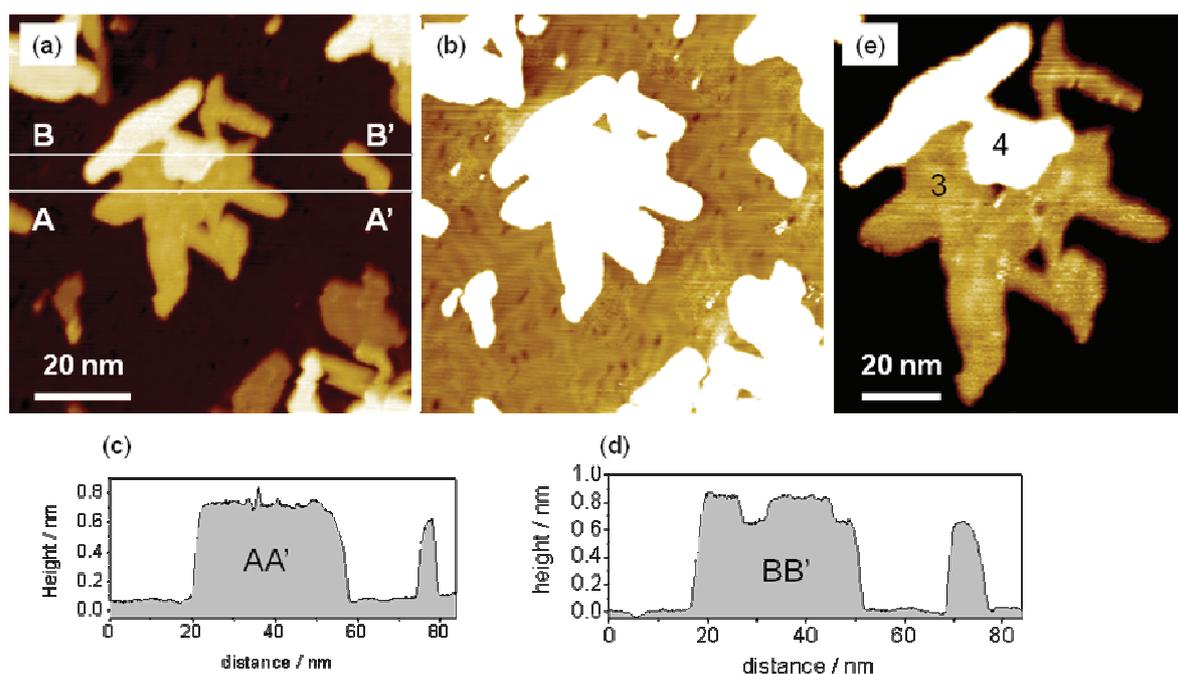

Figure 3.7: (a) *in situ* STM image (840 Å x 840 Å) of a Fe/Au(111) film grown in 1s at -1.3 V with the tip retracted. The film was stabilized at -1.3 V for imaging. (b) Same as (a) with a different image contrast to resolve the Au(111) reconstruction. (c-d) Cross section along the lines AA' and BB' showing that the iron islands consist of several atomic planes. (e) (450 Å x 510 Å) zoom on central island to evidence lines of contrast on the top of islands.

Before closing this paragraph, we would like to comment the step height of 2.6 Å found for the 1st iron monolayer and 2 Å for subsequent atomic planes (measured with respect

to Fe). The discrepancy with previous determinations (2.1 Å)[26] is assigned to the better accuracy of the present determination as compared to experiment in figure 3.5. The present step height is also larger than the ~ 2.1 Å reported for the 1st Fe ML obtained by thermal deposition on Au(111) in the UHV.[9] The *large* step height measured in this work indicates either (i) a tunneling barrier Φ_T that is *smaller* on Fe than on Au and/or (ii) an *enhanced* local density of state (LDOS) on the iron monolayer. In other words the first iron monolayer presents unique electronic effects, which we are probably related to its structure.

b) X-Ray diffraction

All of the x-ray diffraction measurements were carried out *ex situ*. Samples thicker than 6 ML, the measurements were carried out at our laboratory using the custom X-ray bench. After deposition, the samples were protected against oxidation by supplying a CO-saturated solution in order to adsorb CO on the magnetic film. CO is indeed strongly adsorbed on iron group metals (Fe, Co, Ni)[30]. The CO monolayer prevents oxidation of the magnetic film during transfer in ambient air. It stabilizes completely the film as soon as it is placed into the chamber purged with dried atmosphere during XRD measurements. See section 2.2.1 for more experimental details. Samples thinner than 5-6 ML were characterized on DiffAbs line, at Soleil Synchrotron (Gif sur Yvette, France), with D. Thaudières. In this case the magnetic layer was covered an ultrathin gold layer right after deposition to avoid oxidation of the magnetic film. The procedure is similar to the one reported earlier [31]. At the end of deposition the film is set at the stabilization potential (-1.3 V for Fe/Au); the iron solution is then diluted with the supporting electrolyte while keeping the Fe/Au(111) sample at its stabilization potential. Gold chloride (HAuCl4) is then added to the solution so as to reach a 1 mM concentration in gold species and the potential is quickly stepped to -1.6 V to deposit a smooth gold layer in 100 s. The resulting thickness of the top gold layer is ~10 ML.

We looked after the presence of fcc Fe(111) by setting the detector at the proper position but could not find any evidence for this phase in films characterized at the laboratory, i.e. films thicker than 5-6 ML.

We next looked after Fe(110) since UHV-studies have all reported that this is the preferential orientation on (111) oriented substrates. Figure 3.8 presents a typical X-ray diffraction spectrum of a 18 ML-thick Fe/Au(111) measured with an incident angle 0.6° and the detector positioned at $\gamma = 39.84°$ (azimuth) and $\delta = 22.15°$ (height). The wavelength is 1.54 Å (CuKα). There are 12 peaks grouped in 6 pairs. Within a pair, peaks are separated by

~10.52° and pairs of peaks are 60° apart. The peaks at Φ = -9.02°, 61°, 171° and 241° are respectively assigned to (101), (011), (01-1) and (10-1) planes of bcc Fe(110) since they agree very well with crystallographic calculation which predicts peaks at -9.62°, 60.91°, 170.38° and 240.91° in absence of elastic strains. We hence conclude that the iron film is bcc Fe(110) and that it is in epitaxy with Au(111). Given the definition of the origin of Φ angles (see section 2.2) and the peak position of the Au(111) layer (see Fig. 2.15) the epitaxial relationship is therefore Fe(110)<001> ll Au(111)<1-10> (see later Fig. 3.12).
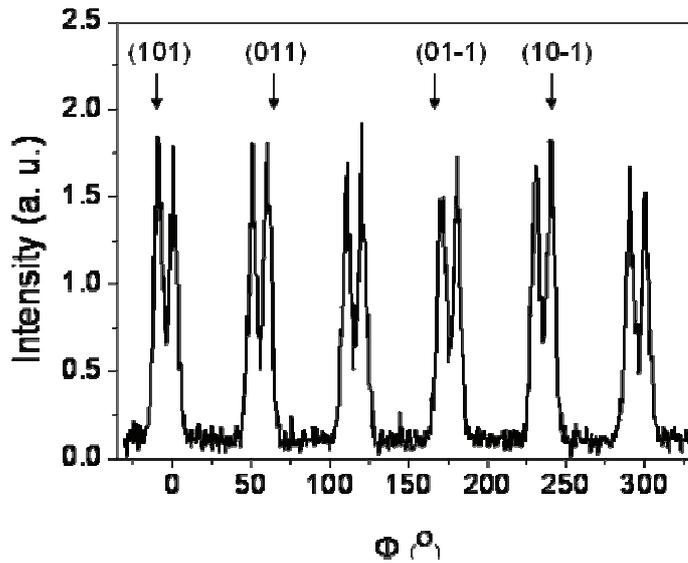
Figure 3.8: X-ray diffraction spectrum of a 18 ML-thick Fe/Au(111) layer deposited at -1.4 V. The incident angle is 0.6° and the detector position γ = 39.84° and δ = 22.15° (λ = 1.54 Å). The four peaks marked with an arrow are consistent with the epitaxial relationship Fe(110)<001> ll Au(111)<1-10>. The other peaks arise from the three fold rotation of the Fe(110) lattice on the Au(111).

Figure 3.9 shows XRD measurements, performed at SOLEIL (λ = 1.7712 Å, *E* = 7 keV), with Au(~5nm)/Fe(X)/Au(111) structures, where X = 5 ML (figure 3.9a) and 3 ML (figure 3.9b). The iron thickness was *a posteriori* carefully calibrated from Fe fluorescence measurements using all of samples. Given the incidence angle 0.6° and the detector position (azimuth = 46.70° and height = 25.665°), the peaks at -3.82° (resp. 4.65°) in figure 3.9a is equivalent to the one measured at -9.02° (res. -0.77°) in Fig. 3.8. The difference in Φ-value stems from the different wavelength used at SOLEL. This demonstrates that a 5 ML-thick iron deposit is a bcc Fe(110) layer with the epitaxial relationship defined above. The only difference between the spectra in figure 3.8 and figure 3.9 is the value of the separation angle ΔΦ = 8.5° between the two peaks. The FWHM is ~5.9°. The 3 ML film (Fig. 3.9b) gives a

more complex spectrum. However, one may confidently decompose it into three contributions: two peaks centered at -3.03° and 3.399° (FWHM ~5.8°) plus a central one at -0.13° (FWHM ~2.9°). The two lateral peaks are equivalent to the ones found in Fig. 3.9a. The central peak is consistent with Au(-10*l*) rod. It was checked that the intensity of peaks decreases with decreasing the incidence angle because the top gold layer absorbs the X-rays (a spectrum is measurable even below the critical angle of gold ~0.66° at 7 keV; suggesting that the gold capping layer is rough). The 3 ML-thick iron layer (Fig. 3.9b) presents therefore the same bcc Fe(111) structure in epitaxy with Au(111), with however a separation angle ΔΦ = 6.45° and the FWHM is ~5.9°.
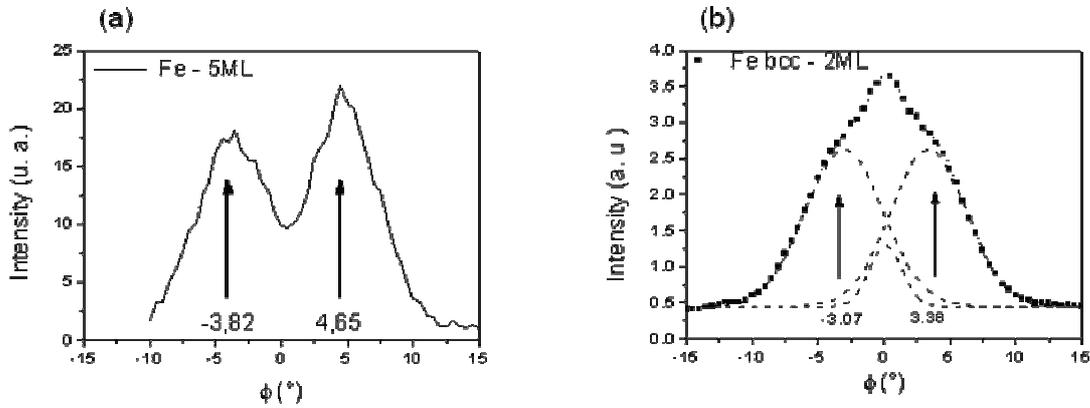
Figure 3.9: Narrow X-ray diffraction spectra around Φ = 0° of a 5 ML (a) and 3 ML (b) thick Fe/Au(111) layers capped with 10 ML of Au. Measurement performed at SOLEIL (λ= 1.7712 Å, E = 7 keV). The iron layers was deposited at -1.5 V. The incident angle is 0.6° and the detector position γ = 46.70° and □ = 25.665°. The spectra can be decomposed into 3 peaks: the central one is related to Au(-10l) rod. The two others are related to bcc Fe(110) as in figure 3.8. These are consistent with the epitaxial relationship Fe(110)<001> ll Au(111)<1-10>.

An intriguing result is that the FWHM remains close to 6° whatever the layer thickness. See figures 3.8 and 3.9. This behavior is at variance of the case of Co/Au(111) or Ni/Au(111), see next chapter), for which FWHM decreases with increasing thickness.[32] To gain insights into this phenomenon other diffraction lines were investigated with a 40 ML-thick film. Table 3.2 collects the FWHM data corresponding to different lines. Injecting these parameters into the analytical relationship below that relates FWHM (expressed in radians) with the in plane mosaicity (*m*), lateral grain size (*L*) and grain thickness (*t*):

$$\Delta^2\phi = m^2 \sin^2\alpha \; + \; (\lambda/L)^2 \frac{\sin^2\alpha}{\sin^2\gamma} \; + \; (\lambda/t)^2 \frac{\tan^2\delta \; \sin^2\alpha}{\sin^2\gamma}$$

We conclude that the FWHM mostly arises from the in plane mosaicity of the iron layer *m* = 9 ± 0.8°. All other contributions are negligible.

Table 3.2: Value of FWHM measured for a selection of diffracting planes. A CO passivated 40 ML-thick Fe/Au(111) film was used. All angles are given in degrees. α is the angle between the (hkl) planes and (110) plane

(hkl)	FWHM	α	γ	δ
(101)	8.31	60	22.336	39.75
(200)	7.84	45	49.471	49.47
(-112)	7.32	54.74	49.471	78.15
(1-10)	8.08	90	0	44.67

c) Ex situ EXAFS:

All EXAFS measurements were carried out with the same sample used on DiffAbs line at Soleil Synchrotron (Gif Sur Yvette, France). The incident angle was 0.6° and the beam polarization was parallel to the surface as shown in figure 3.10a. As measured absorption spectra were transformed into χ(k) spectra as explained in section 2.2.2. Figure 3.10b-c presents the XAFS spectra of a 3 ML (b) and 5 ML (c) Fe/Au(111) layers. Each spectrum is the average of 3 spectra to improve the signal to noise ratio. The two spectra resemble each other very strongly except for a smaller amplitude of oscillations in the case of the thinnest layer. Comparison with theoretical EXAFS spectra of a relaxed bcc Fe(110) (figure 3.10d) and fcc Fe(111) (figure 3.10e) suggests that the studied films present the bcc Fe(110) structure, in agreement with XRD. More detailed simulations will be presented in the discussion.
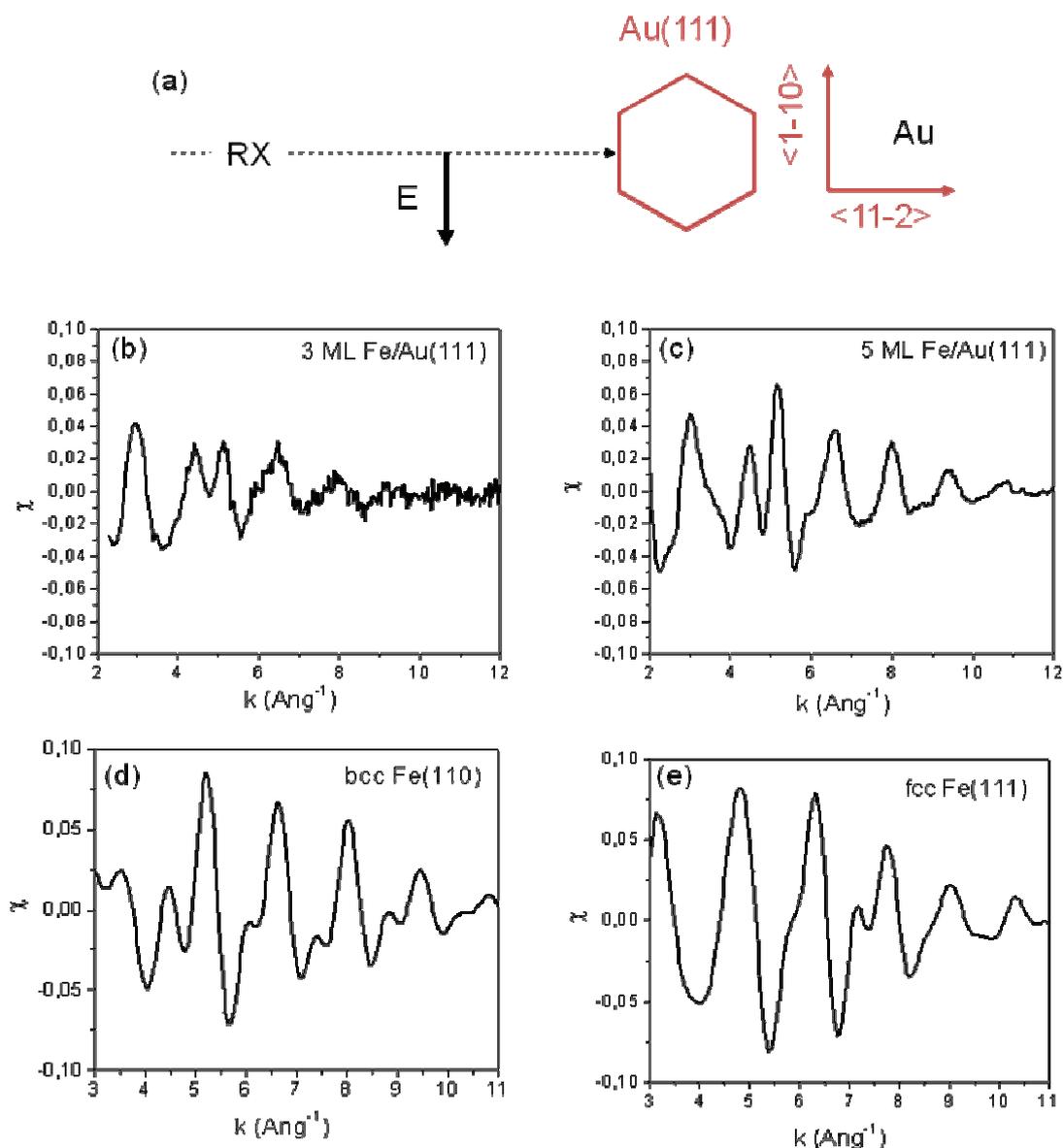
Figure 3.10: (a) Experimental orientation of polarization with respect to Au(111)/Si(111) substrate. Experimental χ(k) spectra for a 3 ML (b) and a 5 ML (b) thick electrodeposited Fe/Au(111) layer (U = -1.5 V) capped with 5 nm of gold. (d-e) calculated spectra of bcc Fe(110) and fcc Fe(111).

3.2.3 Discussion:

Several studies reported a structural phase transition fcc (111) → bcc (110) upon thermal deposition of iron on (111) oriented surfaces. The initial fcc layer is pseudomorphic whatever the substrate lattice parameter. This was not a strong surprise for the system Fe/Ni(111),[33] because the quite small lattice mismatch (1%). The Fe/Cu(111) system, for which the lattice mismatch is 10%, was investigated in very great details and several groups nevertheless observed the above mentioned phase transition[34,4]. In the case of Fe/Au(111)[9]

Chapter 3 – Electrochemical growth and *in situ* magnetism of ultrathin film Fe/Au(111)

and Fe/Pt(111)[8] STM observations have also been interpreted in light of a structural phase transition, although the mismatch is even larger than on copper (14%). Partial strain relief was observed upon growth of the second atomic plane on Pt(111).[8] More recent XRD study confirms that a strained fcc phase is formed before the entire layer relaxes into bcc iron.[13]

a) Nucleation and growth modes:

Our *in situ* STM observations allow to conclude that Fe/Au(111) is nearly a layer by layer process (see figures 3.5 – 3.6) provided a sufficiently negative potential is applied. For $U < -1.5$ V, the homogenous nucleation of one atomic plane thick Fe islands is in fact followed by their lateral expansion. Next atomic planes are growth atop of the first plane. This growth process is different from UHV-STM studies of Fe/Au(111) thermal deposition (TD). In this case the growth is rather 3D than truly 2D because the nucleation is driven by preferential nucleation of nm-islands at the elbows of the Au(111) surface reconstruction.[10],[9] Electrodeposition of Fe on Au(111) resembles, at least in the initial stages only, very strongly to room temperature TD of Fe/Pt(111).[8] However, after completion of the first monolayer, Fe/Fe diffusion and interlayer transport seem severely hindered in the UHV, leading rapidly to multilayer islands. In our case the growth remains a layer by layer process up to several monolayers. One important result of the present work is the demonstration that the growth method has a strong impact on growth.

b) Structure of Fe/Au(111) films thinner than 3 ML.

Unlike for Co or Ni/Au(111) layers, the topography of Fe/Au(111) films is quite smooth on the atomic scale between 1 and 4 ML. See figures 3.5 to 3.7. The surface displays no moiré pattern indicative of a mismatch between the surface and layer lattices. Rather, the smoothness of the iron layer strongly suggests *pseudomorphism*. Given the hexagonal symmetry of the Au(111) surface, the first iron ML can presents an hexagonal symmetry. It is a highly strained pseudomorphic fcc-like Fe(111), even though defining a crystal structure is not quite obvious when it is only 1ML-thick. Pseudomorphism might explain the observed large *apparent* thickness of the 1st ML (2.8 Å are measured against ~2 Å expected). In fact, pulling apart atoms tends to narrow the *d*-band which induces an increased LDOS at Fermi level as compared to a relaxed layer. This conclusion is in accordance with the works cites in introduction of this paragraph in which it was found that TD of iron leads to a pseudomorphic monolayer on various substrates spanning a wide range of lattice parameters: the lattice parameter ranges from 2.5 Å for Ni(111) to 2.79 Å for Pt(111) and 2.88 Å for Au(111).

Above 1 ML, the surface topography of the topmost planes is still smooth on the atomic scale. On resolves some lines of contrast which are running across the surface planes. The associated corrugation is well below 1 Å. See figure 3.5c and figure 3.7. The presence of these features on multilayer islands is taken as an indication of a *partial* strain relaxation. Similar observations were reported on Fe/Pt(111) multilayers in the UHV and attributed to lattice misfit dislocations.[8] We hence conclude that a partial lattice relaxation above 1 ML. It is unfortunately impossible to determine the amount of strain relief because the misfit dislocations do not form an ordered network.

The above discussion supposes that the interface is highly strained (14%) during the growth of the 1st and 2nd monolayers. This must have an impact on the interface structure. Do we have evidence for such huge elastic strains? A first hint is given by figure 3.6b. The fact that Au islands are imaged after Fe dissolution could be simply attributed to the lifting of the 22x√3 Au(111) surface reconstruction. The lifting of the surface reconstruction "liberates" about 4% of the Au top most atoms and creates monatomic islands. The surface coverage of the Au islands in figure 3.6b is however larger than 4%. Therefore we rather infer that the Au islands arise from *localized intermixing* at the Fe/Au(111) interface, in analogy with the observations reported upon the stripping of electrodeposited Co/Au(111) layers.[27] In the case of Co/Au it could be demonstrated that the islands result from a place exchange between Co and Au atoms leading to either an alloy or a Co atoms trapped below a skin of Au atoms as depicted in figure 3.11b. In fact, incorporating "big" atoms (Au) into a Co layer under tensile stress should release the strains (Co is strained by 4.5%). Upon stripping the Co layer, these peculiar phases of the film are electrochemically more stable than pure cobalt. This is why nm-islands were systematically at potentials close but above the dissolution onset potential of cobalt. Trapped Co atoms could be dissolved by applying a sufficiently positive potential. This mechanism was supported by counter experiments with Ni, which is totally relaxed (see next chapter). And in fact stripping Ni/Au(111) layers does not leave islands on the surface. To summarize, the partial release of elastic strains at the Co/Au(111) interface occurs via a place exchange mechanism (i.e. *intermixing*) and leads to the observation of nm-islands upon Co stripping.

In the present work, the applied potential is too positive with respect to the onset of Fe dissolution. This is why the islands in Fig. 3.6b are composed of pure gold. A supplementary proof of their chemical nature is given by the Ostwald ripening observed at longer times after Fe dissolution (Au atoms are much more mobile than iron ones). Given the experimental

conditions we infer that the Au atoms, which were place exchanged with Fe atoms as depicted in Fig. 3.11b, undergo very short atomic displacements only, on the time scale the fast iron dissolution. Namely, the trapped Fe atoms are stripped off thanks to small atomic displacements of the neighboring Au atoms, which agglomerate into compact nm-sized Au islands such as the ones in figure 3.6b. Under this assumption, the uniform spatial and the narrow size distribution of the Au islands indicate a *localized* intermixing in analogy with the case of Co/Au(111). We note in passing that such a place exchange mechanism could be responsible for the nm-sized protrusions in the 1st Fe monolayer (figure 3.6a).
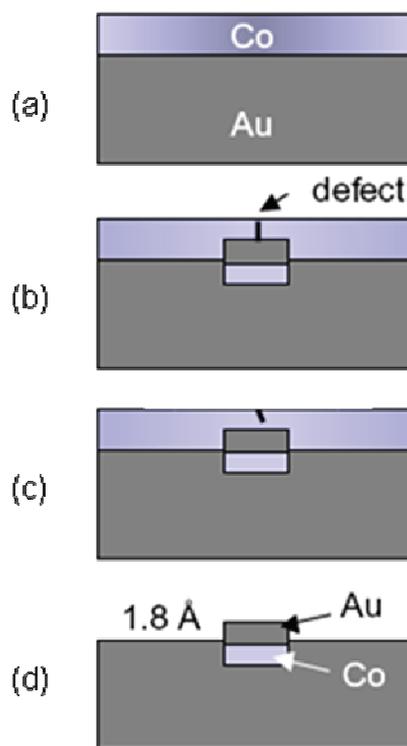
Fig. 3.11: (a-c) schematic model relating local intermixing and strain relief at electrodeposited Co/Au(111) layers. (d) After Co stripping at moderately potential leaves nm-islands left on the surface. They are electrochemically more stable than *pure* Co due to place exchange and/or alloying. Adapted from ref.[27]. Applying a more positive potential would dissolve the Co islands leaving pure Au islands.

c) Structure and epitaxial relationship of Fe/Au(111) thicker than 3ML.

The X-ray diffraction data provide direct insights into the long range structure of the iron layers thicker than 3 ML. They pertain to the formation of bcc Fe(110) as majority phase at this thickness and it is interesting to note that this critical thickness corresponds to the completion of the first bcc (110) unit cell. If fcc Fe(111) is coexisting, the related domains must be too small to diffract. Hence the main epitaxial relationship is Fe(110)<-110> ‖

Au(111)<11-2> as explained by figure 3.12 where we show atomic models of the Au(111) and Fe(110) surfaces. There is an excellent lattice matching between the Au-Au spacing is 2.88 Å along $[1-10]_{Au}$ and the Fe-Fe spacing is 2.86 Å along $[001]_{Fe}$. Such simple geometrical considerations provide a good reason for the epitaxial relationship found experimentally although there is a huge mismatch of 24% along $[1-10]_{Fe}$ and $[11-2]_{Au}$: In figure 3.12a the two lattices have been represented with Fe atoms on top of Au atoms. In reality the Fe atoms are most probably positioned in hollow sites. Figure 3.12b and c show that the elementary Fe(110) unit cell may be orientated in three equivalent directions on Au(111), which explains that 12 peaks are found in the XRD spectrum of figure 3.8. As discussed above the FWHM of peaks may be assigned to in plane mosaicity (6-7°).
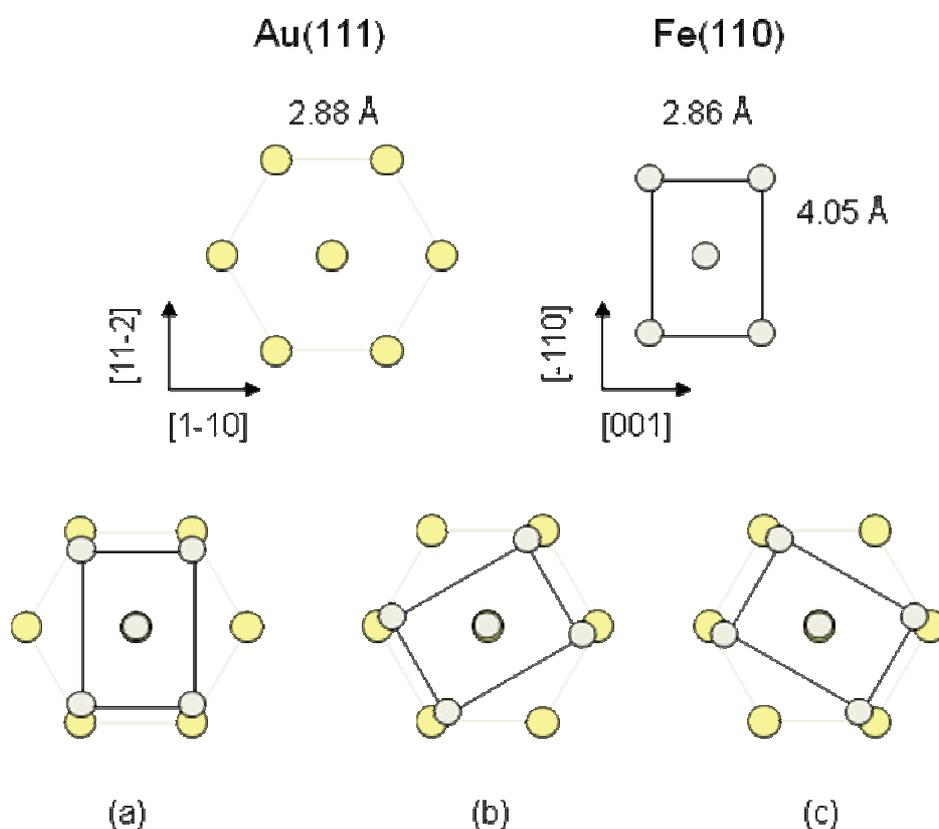
Figure 3.12: Atomic structure of Au(111) and bcc Fe(110) oriented surfaces. Scheme (a) corresponds to the epitaxial relationship Fe(110)<001> ‖ Au(111)<1-10> derived from the XRD pattern in figure 3.8. Schemes (b-c) are the two other possible arrangements for the Fe(110) lattice on Au(111), which explains that 12 peaks are observed in figure 3.8.

Apart of giving the epitaxial relationship, the present XRD data provide also insights into a strain relaxation of the iron layer. In fact the separation angle ΔΦ measured in figures 3.8 and 3.9 may be assigned, form crystallographic calculation, to the amount of uniaxial

strain ε along the <-110> direction ($\varepsilon_{<-110>}$) of Fe. For a relaxed bcc Fe(110) layer $\Delta\Phi$ = 10.52° and it decreases with increasing($\varepsilon_{<-110>}$. Figures 3.13a-b plot the calculated positions of (101) and (011) bcc Fe(110) diffraction peaks and their separation angle $\Delta\Phi$ as a function of $\varepsilon_{<-110>}$. In Figure 3.15 we have combined experimental measurements and calculation to plot the thickness dependence of $\Delta\Phi$ (left hand side vertical scale) and strain (right hand side vertical scale). Clearly, our data reveal a progressive strain relation along <-110>$_{Fe}$ of the bcc Fe(110) lattice, from 8% (3 ML) to 2% (8 ML). ε is close to zero above 10 ML. This strain relaxation will be important in discussing the magnetic state of layers.
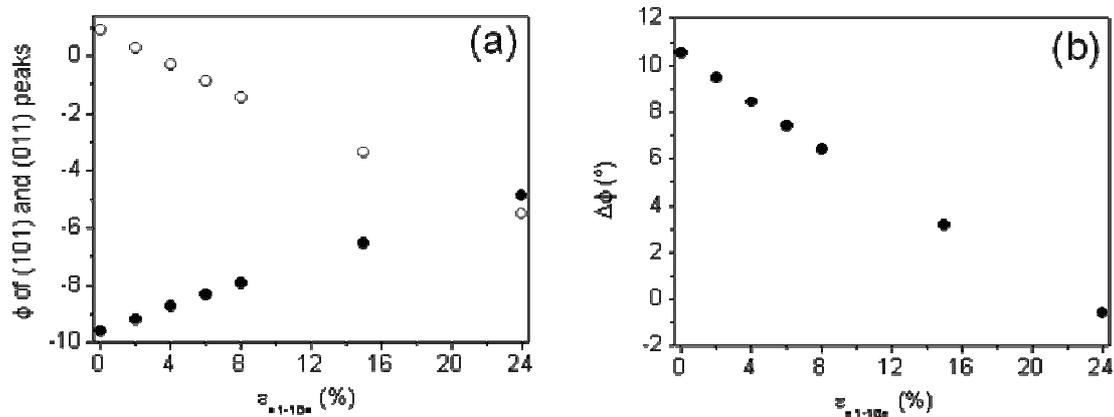
Figure 3.13: (a) Calculated Φ angle of (101) and (011) diffraction peaks as a function variations of the uniaxial strain $\varepsilon_{<-110>}$ along <-110>. (b) Corresponding variations of the separation angle $\Delta\Phi$.
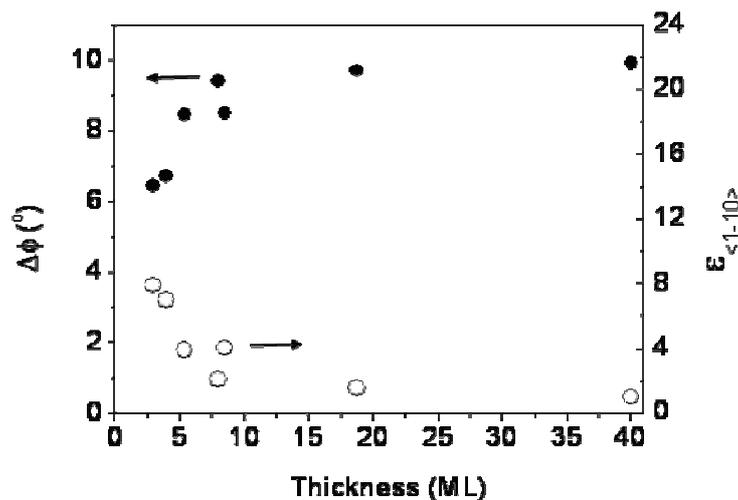
Figure 3.14: Thickness dependence of the uniaxial $\varepsilon_{<-110>}$ in electrodeposited bcc Fe(110)/Au(111) layers (U = -1.5 V). The left hand side vertical axis gives the angle separation $\Delta\Phi$, and the right hand side vertical axis gives the respective strain $\varepsilon_{<-110>}$ in the <-110> direction.

EXAFS provides complementary insights into the local atomic environment, in particular to evidence the presence of phases with domains that are too small to be identified by XRD. Exploiting EXAFS spectra is much more demanding than exploiting XRD as this requires simulation (see section 2.3). We briefly recall here that theoretical EXAFS spectra are the *average* of EXAFS spectra calculated for emitting atoms placed in each of the atomic layer composing one film. In our configuration, one supplementary difficulty was the fact that the bcc Fe(110) unit cell is not isotropic in the plane. To avoid calculating spectra for several beam polarizations, in order to account for the 3-fold rotation of grains (figure 3.10a), we used an *in plane circular polarization*. We checked that this is equivalent to considering the 3 possible Fe(110) in plane orientations. Such a precaution was unnecessary to calculate spectra of fcc iron, which structure is isotropic in all directions of space.

The last columns in Table 3.3 give the parameters corresponding to best fit with experimental curves. ΔN is the relative variation of the number of nearest neighbors with respect to the supposed structure; σ (Debye Weller) defines the static disorder (in addition to thermal disorder accounted for FEFF). ΔE_0 serves to adjust the energy scale on experiment one. This parameter should be less than 3 eV. Chi^2 should be as small as possible.

**Table 3.3: EXAFS calculation assuming different layer structures. The last columns give the parameters corresponding to best fit with experimental curves. See text for the definition of parameters.**

sample	structure	ΔN / %	σ / pm	ΔE_0 / eV	Chi^2
5ML	Relaxed bcc (110)	-25	7.5	1.3	238
		-10*	9.8	1.3	248
		0*	10.9	1.3	264
	Bcc (110) with uniaxial strains:				
	ε<1-10> = 4%, ε<110> = -2%	+16	9	-2.3	345
		0*	7	-2.3	356
3ML	Relaxed bcc (110)	-51	11.7	1.6*	546
	Bcc (110) with uniaxial strains:	-+54	16.5	2.6	287
	ε<1-10> = 5.5%, ε<110> = -2.75%	0*	12.5	2.6	313
	ε<1-10> = 7.9%, ε<110> = -3.95%	0*	12.4	2.6	456
	Relaxed bcc (110) + fcc(111) : 70 : 30	-36	11.2	1.6	364

Analyzing the 5 ML-thick sample was expected to be simpler since one is far from the supposed structural phase transition fcc (111) → bcc (110). The comparison between experiment and calculation is nevertheless not perfect over the whole range of k-values is one assumes a relaxed bcc Fe(110) (figure 3.15a). The best fit yields ΔN = -25%, which is quite large and looks unrealistic. It should be noticed that ΔN and σ are strongly coupled parameters. Namely, a nearly equivalent fit (i.e. a same chi^2) is obtained by fixing ΔN to a more realistic (smaller) value and by slightly increasing σ (compare the first 3 lines in Table 3.3). Calculated plots (not shown) are in fact hardly distinguishable. This result means that the disorder may be accounted in different ways. To be consistent with XRD we attempted fits with uniaxially strained bcc Fe(110) film: we considered a unixial lateral expansion $\varepsilon_{<-110>}$ = 4%, (see Fig. 3.14) and accounting for a vertical compression $\varepsilon_{<110>}$ = -2% because of the tensor of deformations.[35] Fig. 3.15c and Table 3.3 show that the fit is not improved. Several studies about Co/Au(111) layers have reported a similar discrepancy: significant tensile stress was found by XRD or STM but not by EXAFS as far as strains are concerned.[36],[28]
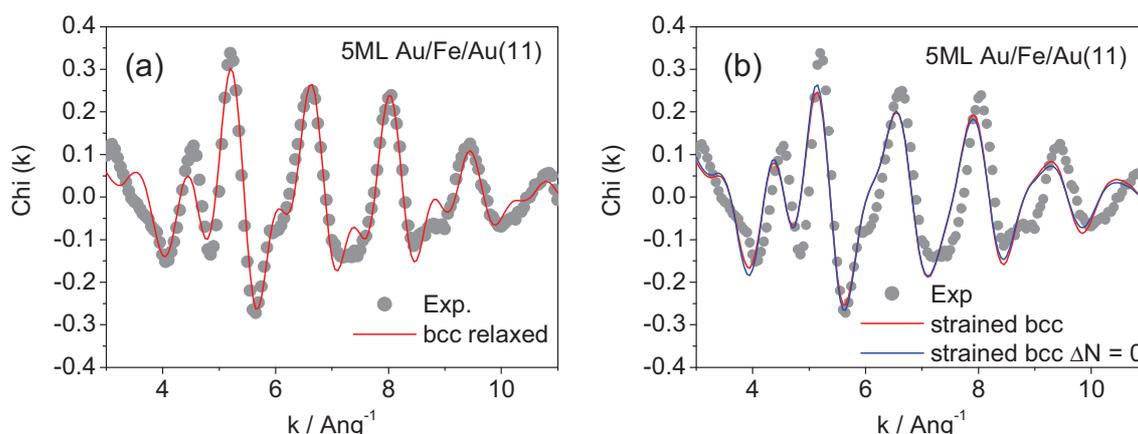
Figure 3.15: Comparison between experimental (symbols) and theoretical (solid lines) EXAFS spectra in the case of the 5 ML-thick Fe/Au(111) sample electrodeposited at U = -1.5 V and capped with 5 nm of gold. Calculations neglect the presence of Au atoms at interfaces. (a) Best fit for a relaxed bcc Fe(110) structure; (b) best fit for a uniaxial stress ε<-110> = 4% and vertical compression ε<110> = -2%. Corresponding parameters are given in Table 3.3.

In the case of the 3 ML–thick sample, the first four hypothesis listed in Table 3.3 for this sample indicate that assuming a pure bcc Fe(110) requires introducing uniaxial strains. Fig. 3.16a demonstrates that the agreement between the experimental and calculated curves is better for $\varepsilon_{<-110>}$ = 5.5% (red curve) than for $\varepsilon_{<-110>}$ = 7.9% -blue curve) which is the value found by XRD (Fig. 3.14). Once again the strains derived from EXAFS appear smaller than

the one derived from XRD. We also attempted considering a mixture of the bcc Fe(110) and fcc Fe(111) phases. To simplify only relaxed phases were assumed. A good fit (see Fig. 3.16b) gives a volume ratio bcc:fcc (70:30) with a chi^2 similar to the one assuming a pure bcc Fe(110) structure with uniaxial stress $\varepsilon_{<-110>}$ = 5/5% (see Table 3.3). Looking at Fig. 3.16, assuming a mixture of bcc and fcc phases better accounts for the experimental spectrum at high k-values while the other assumption fits better the spectrum at low k-values. It is therefore difficult to give a definitive conclusion and more work would be necessary.
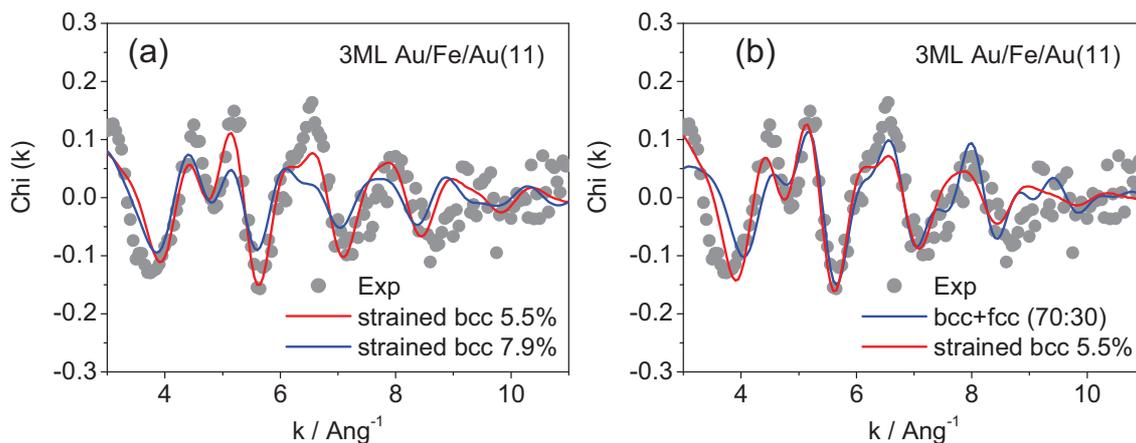
Figure 3.16: Same as in Fig. 3.15 but for 3 ML of iron. (a) Best fit for a strained bcc Fe(110) structure with ε<-110> = 5.5% (red line) and (ε<-110> = 7.9% (blue line). The vertical compression is equal to -2.75% and -3.95% respectively; (b) Blue line is the fit for a mixture of relaxed bcc Fe(110) and fcc Fe(111) phases in vol. ratio 70:30. The red line is the same as in (a). Corresponding parameters are given in Table 3.3.

3.2.4 Conclusions:

Fe/Au(111) electrochemical growth is a monolayer by monolayer growth process and that a structural phase transition *strained* fcc (111) → *strained* bcc (110) fits with very well STM observations. The first monolayer is indeed fcc-like (hexagonal in plane symmetry) as it is pseudomorphic and the huge interfacial stress (14%) induces localized intermixing. The growth of the next atomic plane leads to partial strain in relation with formation of lattice misfit dislocations. Between 2 and 3 ML, the film structure become bcc with the (110) orientation and the epitaxial relationship is Fe(110)<001> ∥ Au(111)<1-10>. The entire film changes of crystallographic structure. The fact that EXAFS analysis requires introducing significant *disorder* in the structure to fit the data, suggests that the real layer structure is probably distorted with respect to idealized ones.

3.3 Magnetic properties of Fe/Au(111) layers

3.3.1 *In situ* MOKE measurements

MOKE measurements were performed with the electrochemical in situ cell (see chapter 2 figure 2.16), with the constant solution flux of 2 mL/min (see section 2.3.2) and with the magnetic field applied perpendicular (PMOKE) and parallel (LMOKE) to the sample surface. A freshly prepared Au(111)/Si(111) substrate was used to start the experiment with a clean surface (see section 2.1.6). The *in situ* MOKE cell was carefully cleaned prior to use.

A typical real time *in situ* MOKE experiment is shown in figure 3.17. The potential program is similar to the one in figure 3.3, with three phases - deposition (I), stabilization (II) and stripping (III). The panels display the potential profile (a), the corresponding current transient (b) and the variations of surface reflectivity (c). The total film thickness is 4 ML in this experiment (the anodic charge measured under the current peak in panel (b) is converted into an average thickness as explained in section 3.2.1). The large signal to noise ratio in panel (c) demonstrates that the sensitivity of $\Delta R_0/R$ is well below 1 ML (see figure 3.17c for the definition of $\Delta R_0/R$).
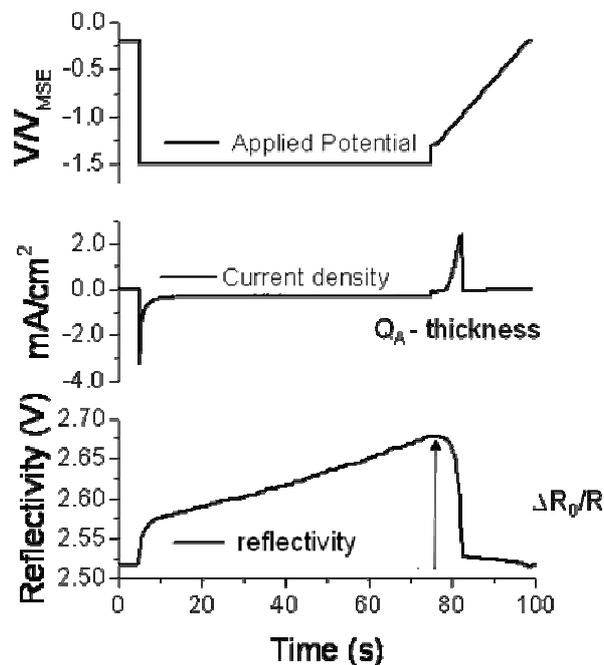
Fig. 3.17: Typical potential program during MOKE experiments (a). Corresponding transients of current (b) and reflectivity (c). The deposition potential is U = -1.5 V (phase I). 4 ML Fe/Au(111) film were deposited in this example.

We repeated the sequence in Fig; 3.17 with increasing deposition time t_D to establish correlations between $\Delta R_0/R$ and the average iron thickness. One example of result is presented in Fig. 3.18. We used a polynomial fit of the data, imposing a constant term equal to zero. For instance the solid line in figure 3.18 is given by the equation below. This expression was used to convert the time-scale of the experiment into a *thickness* scale. It should be noted that the polynomial coefficients slightly vary from experiments to experiments. For this reason thickness - $\Delta R_0/R$ correlations were analyzed each time for a better accuracy:

$$t_{Fe} = 40*(\Delta R/R_0) + 2019*(\Delta R/R_0)^2 + 12024*(\Delta R/R_0)^3 \qquad \text{(Eq. 3.2)}$$
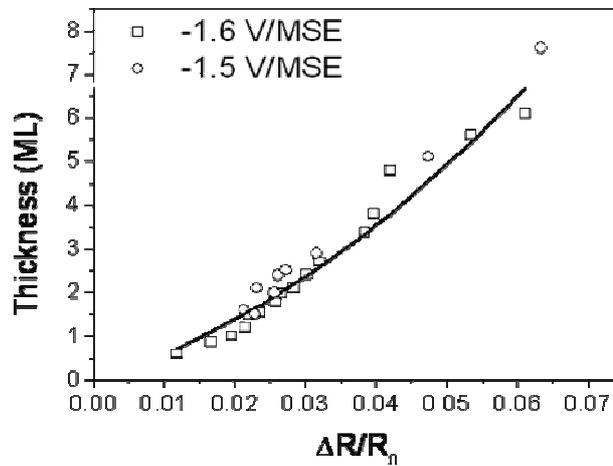
Fig. 3.18: Correlation between ΔR0/R (symbols) and Fe average thickness. The iron films were deposited at -1.5 and -1.6 V/MSE. The line is a polynomial fit of data (see eq. 3.2).

During the whole time sequence shown in figure 3.17, an ac magnetic field was applied to the sample so as to record magnetization curves at a rate of 2/s (500 data point / curve) during growth and dissolution of the iron layer. Selected $M – H$ loops are presented in figure 3.19. We obtain closed hysteresis cycles, i.e. with last points are overlapping the first ones within the noise level, which means that the thickness did not vary too fast. In practice the growth rate must be < 0.2 ML/s. In the case of iron, it is adjusted by the solution concentration since one needs applying U = -1.5 V to obtain a 2D growth (see section 3.2). The time given next of each magnetization curve is the deposition time. From the complete sequence of $M – H$ curves (2 per second), we extract the magnetic moment measured at one field (typically H = 600 Oe to saturate the sample in initial stages, see below), the coercive field H_C and the ratio $M_R/M(H = 600$ Oe). With two hysteresis loops per second (2 HL/s) the

time resolution is 2 data points per second or 1 data point per 0.025 ML (growth rate ~0.05 ML/s).
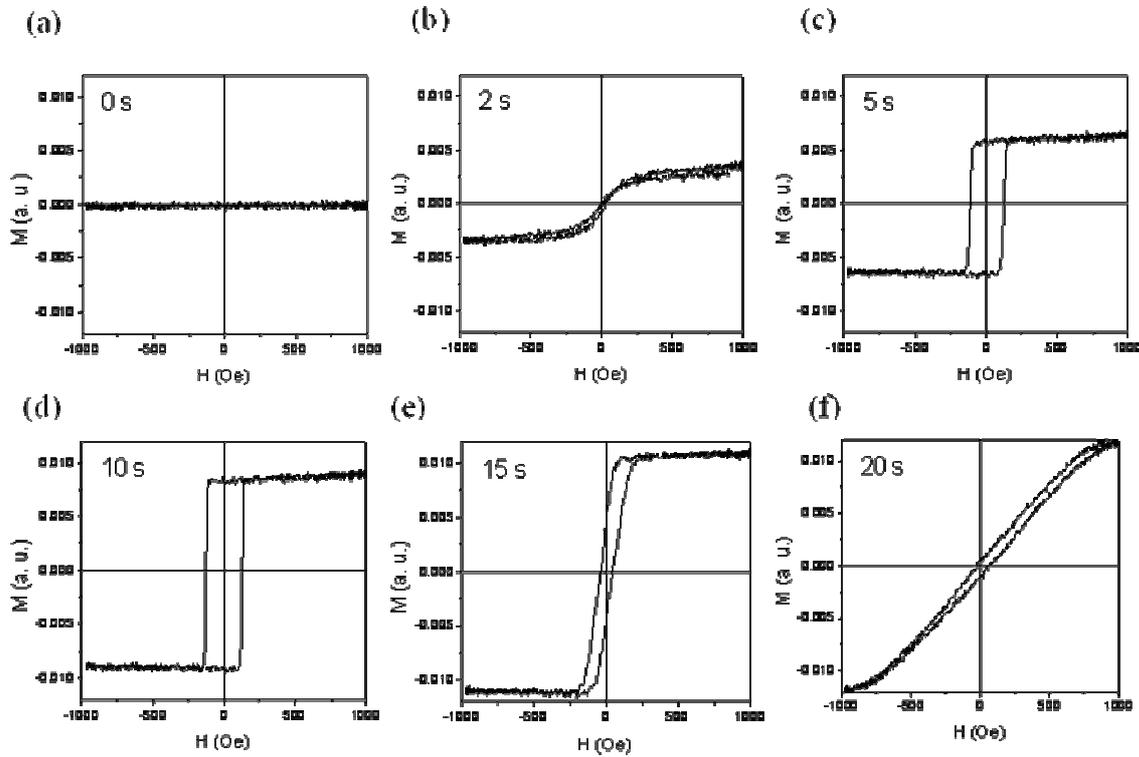
Fig. 3.19: Selected magnetization curves extracted from a complete sequence recorded at a rate of 2 curves / second during Fe growth on Au (a) – (f) the time of deposition is inset each cycle, and the 0 time means a cycle just before the deposition.

Figure 3.20 shows typical magnetic data for Fe/Au(111) layers grown at U = -1.5 V. These data readily demonstrate that a spin reorientation transition occurs around 2.2 ML, since the remanence is total between 1 and 2.2 ML and falls to zero at 2.8 ML, which is close to the thickness at the maximum of M. To ensure that the magnetization anisotropy is indeed exclusively perpendicular to the surface until 2.2 ML, the experiments was repeated in a LMOKE configuration. Figure 3.21a compares the thickness dependence of magnetic moment measured at H = 600 Oe in P- (open symbols) and L-MOKE (filled symbols). In figure 3.21b are plotted the corresponding thickness dependence of $M_R/M_{600\ Oe}$ as a function of thickness using the same symbols for P- and L-MOKE. The anti correlation between the plots in figure 3.21 proves that the magnetization is strictly perpendicular in initial stages of growth before the easy axis rotates towards in the plane direction.
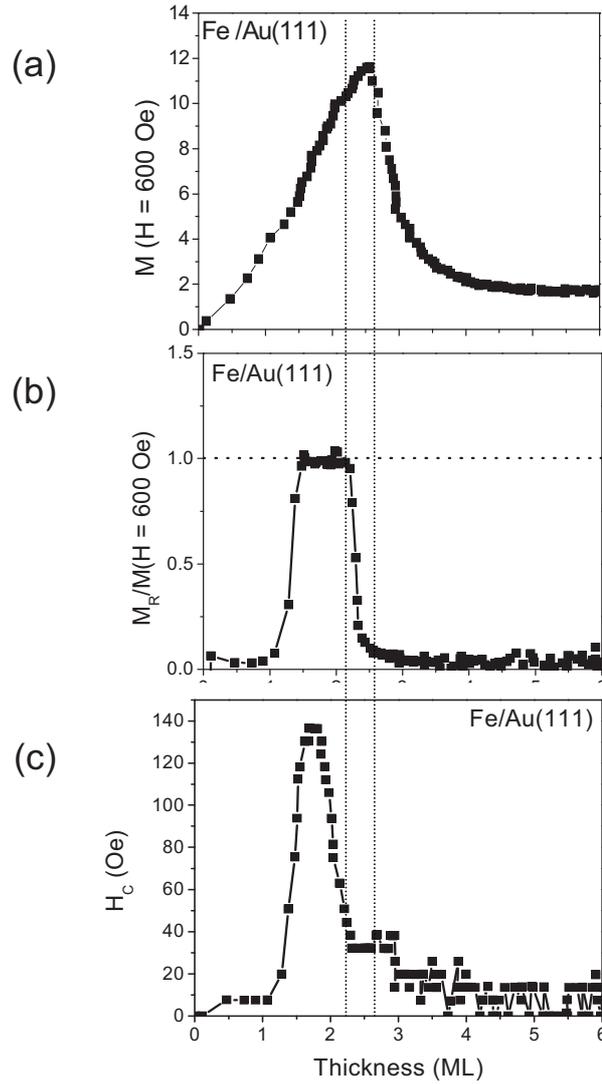
Fig. 3.20: Thickness dependence of the (a) magnetic moment measured at *H* = 600 Oe, of (b) M_R/M and (c) coercive field *H*_C. Vertical dashed line mark critical thicknesses: Up to 2.2 ML the easy axis starts is strictly out of plane; At 2.8 ML, the easy axis is in plane as zero remenence is achieved. Between these tow thicknesses the easy axis is inclined.
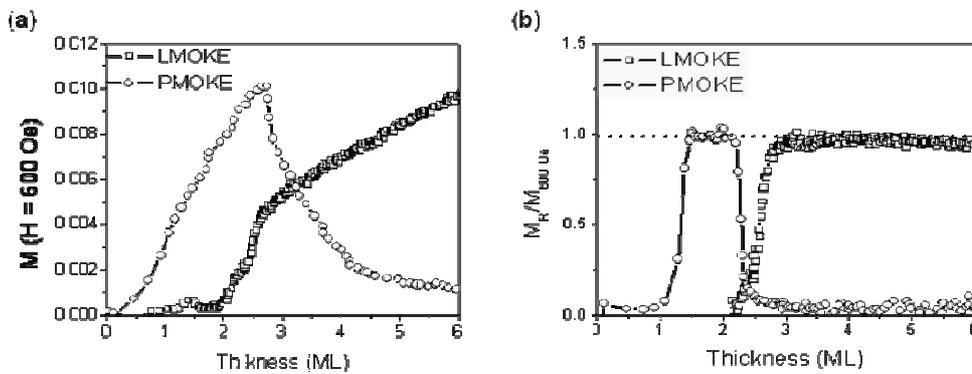
Fig. 3.21: Thickness dependence of the magnetic moment measured at *H* = 600 Oe in P- (open symbols) and L-MOKE (filled symbols); (b) same for M_R/M. Note the anti correlation of plots, which means that *M* is strictly perpendicular up to 2.2 ML. Above 2.8 ML, the easy axis in the surface plane.

3.3.2 Discussion.

From the above P- and L-MOKE measurements we may consider four thickness domains, which are strongly correlated to the film structure.

- For $0 < t_{Fe} < 1$ ML, the layer is perpendicularly magnetized even though the remenence is nearly zero. At this thickness the iron monolayer is pseudomorphic.

- For $1 < t_{Fe} < 2.2$ ML, a long range magnetic order is well established with a strong perpendicular anisotropy as proved by perfectly square magnetization curves. At this thickness partial strain relaxation is observed by STM.

- For $2.2 < t_{Fe} < 2.8$ ML, the easy axis begins to deviate from out of plane orientation but is not totally in the plane of the surface. We will call $t^* = 2.2$ ML, the critical thickness of SRT.

- Region 4: $t_{Fe} > 2.8$ ML, the easy axis lies in the plane of the surface. In this thickness range, the bcc Fe(110) growth is established undergoes progressive strains relaxation (figure 3.15).

a) Model used to account for the spin reorientation transition:

One easy axis of a fcc-like Fe(111) is normal to the surface. In Fe(110) one direction is in plane and two are by 45° off the surface normal. Combining them into one axis perpendicular to the (110) plane, we can simplify the analysis of data by considering a uniaxial anisotropy during the entire growth Fe/Au(111). We therefore used the model of Bruno and Chappert, which is described in Ref. [28], to treat the data. Briefly, we recall that the total magnetic energy (per volume unit) is the sum of the dipolar energy E_d, magneto crystalline energy E_{mc}, interface energy E_s and Zeeman energy E_z, given respectively by;

$$E_D = -2\pi M_S^2 \sin^2 \theta \qquad \text{(Eq. 3.3)}$$

$$E_{mc} = K_1 \sin^2 \theta + K_2 \sin^4 \theta + ... \qquad \text{(Eq. 3.4)}$$

$$E_S = K_S \sin^2 \theta / t_{Fe} \qquad \text{(Eq. 3.5)}$$

$$E_Z = -HM_S \cos^2 \theta \qquad \text{(Eq. 3.6)}$$

where θ is the angle between M and the surface normal. M_s is the saturation magnetization, K_1 and K_2 are the magneto crystalline constants, K_S is an interface constant, H is the applied magnetic field (perpendicular to the surface) and t_{Fe} is the film thickness. Negative anisotropy constants contribute to put the magnetization parallel to the surface and positive anisotropy constants contribute to keep the magnetization perpendicular to the surface. Total energy minimization ($E_T (\theta) = E_d + E_{mc} + E_s + E_z$) gives:

$$2\cos\theta\sin\theta\left[K_{eff} + 2K_S \sin^2\theta + HM_S/(2\cos\theta)\right] = 0 \qquad \text{(Eq. 3.7)}$$

with

$$K_{eff} = K_1 - 2\pi M_S^2 + K_S/t_{Fe} \qquad \text{(Eq. 3.8)}$$

where K_{eff} is the effective anisotropy constant. K_{eff} can also be written as

$$K_{eff} = -2K_2 \sin^2\theta - HM_S/(2\cos\theta) \qquad \text{(Eq. 3.9)}$$

From eq. 3.8 plotting $K_{eff} * t_{Fe}$ vs t_{Fe} should give a straight line at sufficiently large film thickness, the slope of which being equal to K_1 - $2\pi M_s^2$ and the constant at $t = 0$ gives K_s. The determination of K_{eff} requires the knowledge of θ (see Eq. 3.9). Recalling that cos $\theta = M/M_S$, this requires determining M_S, which is impossible with our set-up in PMOKE configuration when the film is in plane magnetized.

b) Thickness dependence of the magnetic moment:

It seems realistic to consider that our bcc Fe(110) layers present a saturation moment close to the bulk value M_S^{bcc} = 1714 emu (or μ = 2.2 μ_B) [37] and a K_1 ~7.10^6 erg/cm^3 as soon as they are *thicker* than 4-5 ML. In fact the strains are largely released (Fig. 3.14) and the Curie temperature of Fe films is ~0.8 $T_C(\infty)$ = 840 K ($T_C(\infty)$ = 1044 K for bcc iron) [38] (see Fig. 3.22). The question arises however concerning the magnetic moment below 3ML. Below this critical thickness, the Fe/Au(111) presents indeed a strained fcc structure. We used the procedure explained in Fig. 3.23 to calibrate the MOKE signal and determine the M_S value below ~3 ML.
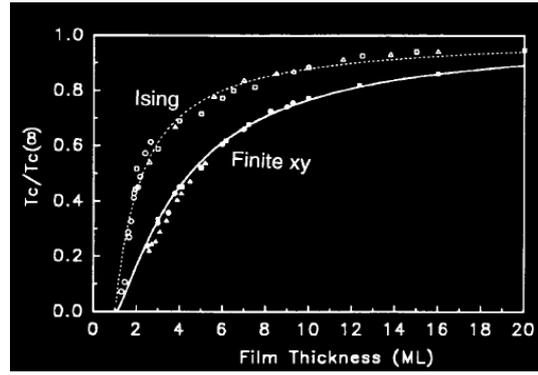
Figure 3.22: Figure taken from Ref. [2] showing the experimental decrease of Curie temperature (symbols) with the number of monolayers in films of different materials and with different orientations. For more details are available in Ref. [39]. Data points corresponding to Fe(110)/Ag(111) are among those of the "Ising" curve.

To calculate K_{eff}^{bcc} of bcc iron layers we need cos (θ) (see eq. 3.9). Since our PMOKE set-up is unable to saturate in plane magnetized layers, we must *a priori* assume an effective magnetization at saturation $M_S^{eff} = P*t_{Fe}$ expressed in arbitrary units (see Fig. 3.23a). This allows calculating $\cos(\theta) = M(600\ \text{Oe})/ M_S^{eff}$. Injecting the thickness dependence of $\cos(\theta)$ into eq. 3.9 and taking $M_S^{bcc} = 1714$ emu, K_{eff} is determined as a function of the film thickness (we neglect the contribution of K_2 in Eq. 3.9). Plotting $K_{eff} * t_{Fe}$ vs t_{Fe} gives a straight line (Fig. 3.23b) which slope is $K_1 - 2\pi M_s^2$ and intercept is K_S for $t_{Fe} = 0$. Repeating the procedure for other P-value we plotted in Fig. 3.23c, the relationship between the determined K_1-value and P (filled symbols, left hand side scale) and K_S and P (open symbols, right hand side scale). From Fig. 3.23c, the right value of P is 0.0032, because this gives $K_1 \sim 7.10^6$ erg/cm³, which is the tabulated value for bcc iron. This way we can calibrate the MOKE signal $P = 0.0032$ is equivalent to $M_S = 1714$ emu or 2.2 μ_B. This calibration holds for the considered experiment and it must be performed for each experiment.

Our Fe/Au(111) layers are strictly perpendicularly magnetized in the thickness range 1 < t_{Fe} < 2.2 ML (Fig. 3.20-3.21), The sample is saturated for $H = 600$ Oe. Between 2.2 ML and 2.8 ML (Fig. 3.20e) the layer is still saturated at H = 600 Oe although the easy axis of magnetization begins to rotate. The slope of the left hand side flank of the peak is $P = 0.0035$ (blue line in Fig. 3.23a). We hence deduce that $\mu \sim (0.0035/0.0032)* \mu^{bcc} = 2.4$ μ_B.

The value $\mu^{bcc} = 2.4$ μ_B corresponds to the moment per atom of a 1 – 2 ML Fe film at at room temperature. This can suggests a HS fcc iron phase or a strained bcc. However to compare it with predictions (see Fig. 3.1) we must correct it from the reduction of the Curie temperature. To this end we can use the relationship $\mu(RT)/\mu_B(0\ K) = (1-T/T_C)^\beta$ in which the

exponent β depends on the dimensionality of the system.[2] Fig. 3.22 gives $T_C \sim 500$ K for a 2 ML film ($T_C/T_C(\infty) \sim 0.5$), a value close to the 430 K measured in vacuum for 2.8 ML Fe/Au(111) film,[12] The key question concerns the β-value. In three dimensions β ~ 0.33 and in two dimensions span a range 0.125 (Ising model) - 0.23 (Heisenberg model). A value β = 0.30 ± 0.02 was experimentally determined for γ-Fe/Cu multilayers[38] which fits with the 3D case and probably does not apply to our films which are 1-2 ML-thick. Taking $T_C = 500$ K and assuming that β = 0.137 (this value was found by Bader et al. for Fe/Ag(111) films, see reference cited in the review Ref.[2]), the formula above yields $\mu(RT)/\mu_B(0$ K$) = 0.90$. Hence we find a moment per atom that is surprisingly close to the accepted value 2.7 μ_B for the HS phase of strained fcc (111) and bcc (110) strained. This is consistent with the formation of a highly strained Fe(111) layer between 1 and 2 ML.
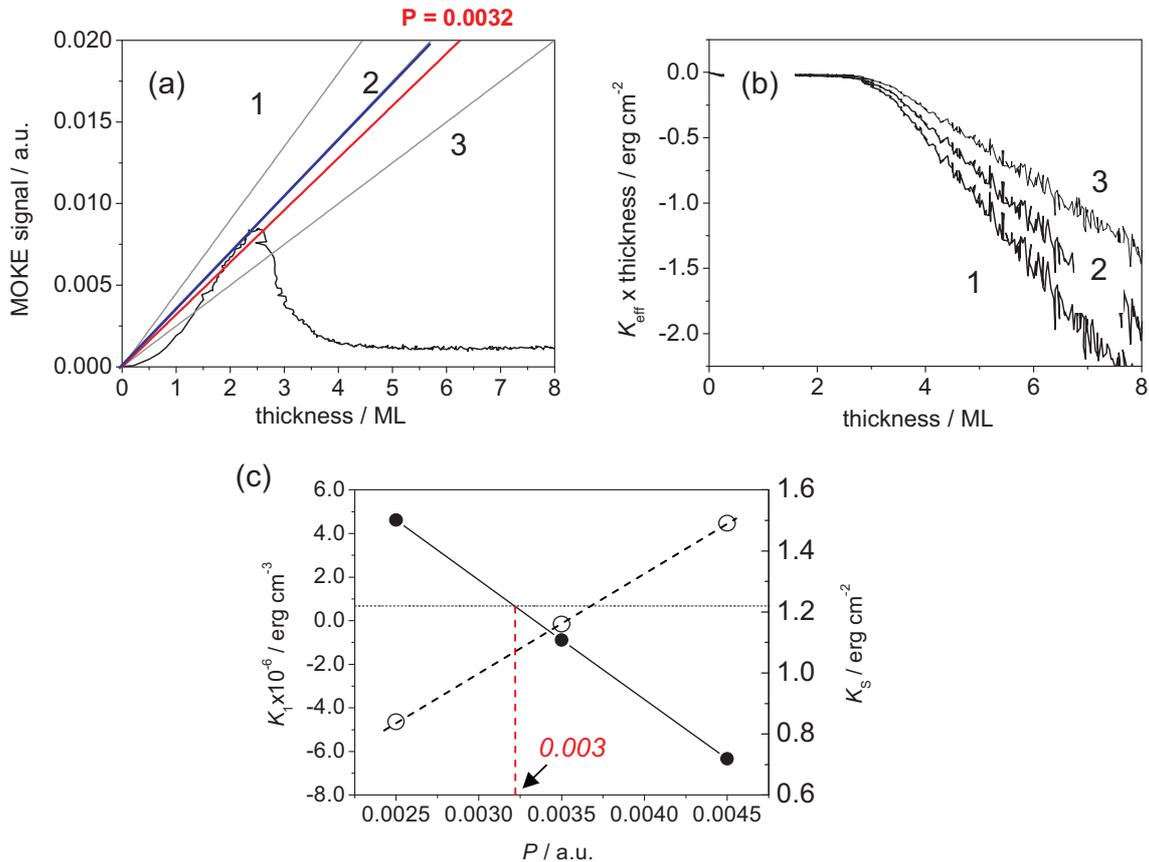
Figure 3.23: procedure used to calibrate the MOKE signal into a magnetic moment. (a) Plot $M - t_{Fe}$ as in Fig. 3.21. Straight lines 1- 3 have a slope P = 0.0045, 0.0035 and 0.0025 respectively. (b) Plot of $K_{eff}*t_{Fe}$ versus t_{Fe} for different P-values (curves 1 – 3 correspond to the P-values given in (a)). (c) Corresponding values of K_1 and K_S. The relevant slope P is 0.0032 (red line in (a) to obtain $K_1 \sim 7.10^6$ erg/cm³ in (c) which the bulk value of bcc iron. The corresponding $K_S \sim 1.1$ erg/cm². In this experiment the calibration is P = 0.0032 $\leftrightarrow \mu^{bcc} \sim 2.2$ μ_B. Because the rise of the left hand side of the peak in (a) has a slope 0.0035 (blue line) one deduces μ (below 2.8 ML) ~ 2.4 μ_B. See text for more explanation.

c) Interface anisotropy constants:

Figure 3.23 yields K_S = 1.1 erg/cm^2. This value, corresponds to the contribution of both the nearly *relaxed* Fe(110)/Au(111) and the Fe(110)/solution interfaces to PMA. From an experimental viewpoint, capping the Fe/Au(111) layer with Au or Cu leads to an in plane magnetization. For layers thicker than 3 ML, a K_S-value ~ 1 erg/cm^2 was found for the Au or Cu/Fe/Au interface prepared either by electrodepositiond[26] or thermal deposition.[41] Assuming that the top and bottom interface are equivalent, one deduces K_S^{Fe-Au} ~ 0.55 erg/cm^2 for the Au/bcc Fe interface, either obtained by TD or electrodeposition.

Below ~3 ML, the layer adopts a strained fcc structure and the overall anisotropy is characterized by the critical thickness t^* = 2.2 ML. This critical thickness may be translated into a constant K_S = 0.96 erg/cm^2 by injecting M_S = 1870 emu (μ = 2.4 μ_B, see above) in Eq. 3.8 and neglecting K_1. Since K_S^{Fe-Au} is the same at either TD or ED Fe/Au(111) layers (see above), we deduce K_S^{Fe-Sol} ~ 0.96 – 0.55 = 0.41 erg/cm^2. In UHV, using t^* ~ 2.8 ML[12,41] gives an overall K_S = 1.27 erg/cm^3. Therefore K_S^{Fe-UHV} = 1.27 – 0.55 = 0.72 erg/cm^2. Hence both the Fe/solution and Fe/vacuum interface give a positive contribution to anisotropy. This result is at variance of the case Co/Au(111), for which K_S^{Co-Sol} < 0.[42] In this case the *d*-band of cobalt is probably affected by water molecules. This is not the case for Fe(111).

d) Magnetic state below 1 ML:

Above 1.4 ML, electrodeposited Fe/Au(111) layers present a long range magnetic order as the Curie temperature is above RT. See the magnetization curves with full remanence (Figure 3.19 and 3.20). Below 1 ML, the absence of remanence together with a somewhat reduced moment must be attributed to a further decrease of T_C (Fig. 3.22). There is nevertheless long range ferromagnetic ordering, which is at reverse of observation with TD Fe layers on Au(111) and other substrates. Several facts may concur to this difference:

  - (i) The magnetic moment of the strained fcc phase. Although there is no quantitative indication of the moment value in the case of TD Fe/Au(111) layers, we note that Fe/Cu(111) is a LS phase in the monolayer range.[3]

  - (ii) The film morphology. The above STM observations (figure 3.6) demonstrate that a 0.7 ML Fe layer is continuous, whereas a TD layer on Au(111) is composed of nm islands due to specific nucleation at surface dislocations.[9] The specific morphology of ED layers favors magnetic ordering.

3.3.3 Conclusions

Electrodeposited (ED) Fe/Au(111) layers are ferromagnetic at room temperature down to a fraction of a monolayer, even though the absence of remanence suggests a reduced Curie temperature below 1 ML. As soon as the thickness exceeds 1 ML T_C rises above room temperature as full remanence is observed. A clear PMA is observed up to 2.2 ML, with perfectly square magnetization curves. The magnetic moment per atom ~2.4 μ_B corresponds, after correction from the reduced T_C, to the HS phase of fcc iron. Above 2.2 ML a progressive rotation of the easy axis is observed towards in plane direction. The anisotropy constant of the Fe/Au(111) interface is $K_S^{Fe\text{-}Au}$ ~ 0.55 erg/cm^2 and that of the Fe/solution interface is $K_S^{Fe\text{-}Au}$ ~ 0.41 erg/cm^2.

3.4 General conclusion about Fe/Au layers:

The structure "solution/Fe/Au(111)" undergoes a clear SRT around t^* ~ 2.2 ML which could be coupled with the structural phase transition fcc Fe(111) → bcc Fe(110). The magnetic moment is nearly constant and equal to 2.4 μ_B below t^*. This value, corrected from the reduced T_C, corresponds to HS strained fcc iron phase with U = 2.7 μ_B. The strong interface anisotropy arises from the Fe/Au *and* the Fe/solution interfaces. Above 3 ML, the layer becomes bcc Fe(110) and is in plane magnetized with a magnetic moment 2.2 μ_B.

3.5 Bibliography

[1]   V. L. Moruzzi, P. M. Marcus, and J. Kübler, "Magnetovolume instabilities and ferromagnetism versus antiferromagnetism in bulk fcc iron and manganese," Phys. Rev. B **39** (10), 6957 (1989).

[2]   F. J. Himpsel, J. E. Ortega, G. J. Mankey et al., "Magnetic nanostructures," Advances in Physics **47** (4), 511 - 597 (1998).

[3]   P. Ohresser, J. Shen, J. Barthel et al., "Growth, structure, and magnetism of fcc Fe ultrathin films on Cu(111) by pulsed laser deposition," Phys. Rev. B **59** (5), 3696 (1999).

[4]   A. Biedermann, W. Rupp, M. Schmid et al., "Coexistence of fcc- and bcc-like crystal structures in ultrathin Fe films grown on Cu(111)," Physical Review B (Condensed Matter and Materials Physics) **73** (16), 165418 (2006).

[5]   J. Giergiel, J. Shen, J. Woltersdorf et al., "Growth and morphology of ultrathin Fe films on Cu(001)," Physical Review B **52** (11), 8528 (1995).

[6]   M. Tsujikawa, A. Hosokawa, and T. Oda, "Magnetic anisotropies of iron on the Pt(111) surface," Journal of Physics: Condensed Matter **19** (36), 365208 (2007).

[7]   Cheng Ruihua, S. D. Bader, and F. Y. Fradin, 2008 (unpublished).

[8]   D. Repetto, T. Y. Lee, S. Rusponi et al., "Structure and magnetism of atomically thin Fe layers on flat and vicinal Pt surfaces," Phys. Rev. B **74** (5) (2006).

[9]   A. J. Stroscio, D. T. Pierce, R. A. Dragoset et al., "Microscopic aspects of the initial growth of metastable fcc iron on Au(111)," The Journal of Vacuum Science and Technology A **10**, 1981-1985 (1992).

[10]   Bert Voigtländer, Gerhard Meyer, and Nabil M. Amer, "Epitaxial growth of Fe on Au(111): a scanning tunneling microscopy investigation," Surf. Sci. **255** (3), L529-L535 (1991).

[11]   G. Lugert, W. Robl, L. Pfau et al., "Magnetic anisotropy and film structure in ultrathin Fe films on Au(111)," Journal of Magnetism and Magnetic Materials **121** (1-3), 498-502 (1993).

[12]   O. Toulemonde, V. Petrov, A. Nait Abdi et al., "Magnetic anisotropies of ultrathin Fe films on Au(111) as function of iron thickness and gold capping," **95**, 7345 (2004).

[13]   D. T. Dekadjevi, B. J. Hickey, S. Brown et al., "Structural phase transition of Fe grown on Au(111)," Phys. Rev. B **71** (5), 054108 (2005).

[14]   Tetsuo Okuyama, "Crystallographic and Magnetic Properties of Fe/Au(001) and Fe/Au(111) Superlattice Films," Japanese Joournal of Applied Physics **30**, 2053-2057 (1991).

[15]   H. J. Elmers, J. Hauschild, and U. Gradmann, "Onset of perpendicular magnetization in nanostripe arrays of Fe on stepped W(110) surfaces," Phys. Rev. B **59** (5), 3688 (1999).

[16]   S. Forster, G. Baum, M. Muller et al., "Oxygen adsorption on Fe/W(110) and Co/W(110) thin films: Surface magnetic properties," Phys. Rev. B **66** (13) (2002).

[17]   K. von Bergmann, M. Bode, and R. Wiesendanger, "Coverage-dependent spin reorientation transition temperature of the Fe double-layer on W(110) observed by scanning tunneling microscopy," Journal of Magnetism and Magnetic Materials **305** (2), 279-283 (2006).

[18]   Georg Rauchbauer, Andreas Buchsbaum, Hannes Schiechl et al., "Ultra-thin Fe films grown on Cu by pulsed laser deposition: Intermixing and bcc-like structures," Surf. Sci. **602** (8), 1589-1598 (2008); J. Shen, Zheng Gai, and J. Kirschner, "Growth and

magnetism of metallic thin films and multilayers by pulsed-laser deposition," Surf. Sci. Rep. **52** (5-6), 163-218 (2004).

[19] H. Schiechl, G. Rauchbauer, A. Biedermann et al., "Growth of ultrathin Fe films on Cu(1 1 1) by pulsed laser deposition," Surf. Sci. **594** (1-3), 120-131 (2005).

[20] J. Zarpellon, H. F. Jurca, J. J. Klein et al., "Iron Silicide Formation from Fe Thin-Film Electrodeposition on Hydrogen-Terminated Si(111)," J. Electrochem. Soc. **152** (12), C808-C812 (2005).

[21] Bao Zhi Liang and L. Kavanagh Karen, "Epitaxial Fe/GaAs via electrochemistry," J. Appl. Phys. **98** (6), 066103 (2005).

[22] Y. K. Liu, C. Scheck, R. Schad et al., "Epitaxial Growth of Fe Films on n-Type GaAs by Electrodeposition," Electrochemical and Solid-State Letters **7** (9), D11-D13 (2004).

[23] W. Schindler, O. Schneider, and J. Kirschner, 1997 (unpublished).

[24] A. Gundel, A. Morrone, J. E. Schmidt et al., "Magnetic properties of electro deposited Fe/Au(111) layers: in situ AGFM measurements," Journal of Magnetism and Magnetic Materials **226**, 1616-1617 (2001).

[25] A. Gundel, T. Devolder, C. Chappert et al., "Electrodeposition of Fe/Au(111) ultrathin layers with perpendicular magnetic anisotropy," Physica B-Condensed Matter **354** (1-4), 282-285 (2004).

[26] L. Cagnon, Université Paris Sud, 2000.

[27] P. Allongue, L. Cagnon, C. Gomes et al., "Electrodeposition of Co and Ni/Au(1 1 1) ultrathin layers. Part I: nucleation and growth mechanisms from in situ STM," Surface Science **557** (1-3), 41-56 (2004).

[28] L. Cagnon, T. Devolder, R. Cortes et al., "Enhanced interface perpendicular magnetic anisotropy in electrodeposited Co/Au(111) layers," Physical Review B **63** (10), 104419 (2001).

[29] A. Gundel, L. Cagnon, C. Gomes et al., "In-situ magnetic measurements of electrodeposited ultrathin Co, Ni and Fe/Au(111) layers," Phys. Chem. Chem. Phys. **3** (16), 3330-3335 (2001); A. Gündel, T. Devolder, C. Chappert et al., "Electrodeposition of Fe/Au(1 1 1) ultrathin layers with perpendicular magnetic anisotropy," Physica B: Condensed Matter **354** (1-4), 282-285 (2004).

[30] A. R. Cuesta and G. Zgrablich, "KINETICS AND ENERGETICS OF ADSORPTION FOR THE CO/K/NI(110) SYSTEM," Surface Science **275** (1-2), L636-L639 (1992).

[31] P. Prod'homme, F. Maroun, R. Cortès et al., "Preparation, characterization and magneto-optical investigations of electrodeposited Co/Au films," Journal of Magnetism and Magnetic Materials **315** (1), 26-38 (2007).

[32] P. Prod'homme, F. Maroun, R. Cortes et al., "Preparation, characterization and magneto-optical investigations of electrodeposited Co/Au films," J. Magn. Magn. Mater. **315** (1), 26-38 (2007).

[33] G. C. Gazzadi, F. Bruno, R. Capelli et al., "Structural transition in Fe ultrathin epitaxial films grown on Ni(111)," Physical Review B **65** (20), 205417 (2002).

[34] J. Shen, P. Ohresser, Ch V. Mohan et al., "Magnetic Moment of fcc Fe(111) Ultrathin Films by Ultrafast Deposition on Cu(111)," Phys. Rev. Lett. **80** (9), 1980 (1998).

[35] D. Sander, "The correlation between mechanical stress and magnetic anisotropy in ultrathin films," Reports on Progress in Physics **62** (5), 809-858 (1999).

[36] N. Marsot, R. Belkhou, H. Magnan et al., "Structure and local order in Co magnetic thin films on Au(111): A surface EXAFS study," Phys. Rev. B **59** (4), 3135 (1999).

[37] E. P. Wohlfarth, "Ferro-magnetic Materals," **Volume 1**.

[38] B. Sadeh Y. Yamada, C. Lee, M. Doi and M. Matsui, "Magnetic Critical Behavior of γ-Fe/Cu Multilayer," Journal of the Magnetics Society of Japan **23**, 575-577 (1999).

[39]   F. Huang, M. T. Kief, G. J. Mankey et al., "Magnetism in the few-monolayers limit: A surface magneto-optic Kerr-effect study of the magnetic behavior of ultrathin films of Co, Ni, and Co-Ni alloys on Cu(100) and Cu(111)," Phys. Rev. B **49** (6), 3962 (1994).

[40]   F. J. Himpsel, J. E. Ortega, G. J. Mankey et al., "Magnetic nanostructures," Adv. Phys. **47** (4), 511-597 (1998).

[41]   C. Chappert, P. Bruno, B. Bartenlian et al., "Magnetic anisotropy and interlayer exchange coupling in Fe(110) / Au(111) ultrathin films," Journal of Magnetism and Magnetic Materials **148** (1-2), 165-166 (1995).

[42]   Philippe Allongue, Fouad Maroun, Hugo F. Jurca et al., "Magnetism of electrodeposited ultrathin layers: Challenges and opportunities," Surface Science **603** (10-12), 1831-1840 (2009).

Chapter 4

Electrochemical growth and *in situ* magnetism

of ultrathin film Ni/Au(111) and Fe/Ni/Au(111)

4.1 Introduction

In this chapter we study the influence of inserting a Ni(111) layer between Fe and Au(111) to study the influence of strains on the magnetic anisotropy and moment in the initial stages of the growth. This study is also a preliminary step towards the study of more complex systems such as electrodeposited FeNi alloy layers on Au(111) (see next chapter). In FeNi alloys, both "lateral" as well as "vertical" magnetic exchange interactions are involved, which are related to hybridization of different atomic orbital.

While Ni/Au(111) electrodeposition been recently investigated by a few groups[1,2] which showed that growth proceeds in a layer by layer fashion at sufficiently negative potential, there is no electrochemical work available concerning Fe/Ni growth. Only a few experimental UHV studies of Fe/Ni(111) growth are available in literature.[3,4,5] They all evidence that growth begins with formation of a pseudomorphic monolayer and that a structural phase transition fcc Fe (111) → bcc Fe(111) occurs around 2 ML. A few theoretical studies about the structure and magnetism are also available.[6]

Before dealing with the main subject of this chapter, we briefly present a few original data about Ni/Au(111) electrochemical growth that are necessary to this work. We put emphasis on the magnetic properties at very low thickness. The main body of this chapter is Fe electrodeposition on Ni/Au(111) to discuss magnetic interactions between the two magnetic layers.

4.2 Structure and magnetism of Ni/Au(111): Results and discussion

4.2.1 Ni/Au(111) growth

Figure 4.1 presents the cyclic voltammogram (CV) of a Au(111)/Si(111) electrode in contact with a 0.5 mM $NiSO_4$ solution in 0.1 M K_2SO_4 + 1 mM H_2SO_4 + 1 mM KCl as supporting electrolyte. Starting from -0.2 V the potential was scanned negatively towards -1.5 V before being reversed and scanned back up to -0.2 V. Unlike for iron (Fig. 3.2) there is only one cathodic peak which is centered at -1.15 V. In the case of Ni/Au deposition, the reduction of protons in solutions ($H^+ + e^- \rightarrow \frac{1}{2} H_2$) occurs in parallel with nickel deposition ($Ni^{2+} + 2e^- \rightarrow Ni^0$). In other words the two peaks C1 and C2 found with iron merge into single and broad cathodic wave. The anodic peak A2 (-0.75 V) is assigned to the dissolution of the nickel film ($Ni^0 \rightarrow Ni^{2+} + 2e^-$) which had been deposited during the negative going potential sweep. Using the deposition procedure described in section 3.2.1 and applying the stripping method to determine the film thickness (see Table 3.1 for the conversion anodic charge to average thickness), we have plotted in Fig. 4.2 the variations of t_{Ni} as a function of deposition time at various deposition potentials U = -1.35, -1.4 and -1.5 V. All plots may be approximated by two straight lines which intersect for t_{Ni} ~1ML, which is similar to the case of Fe/Au(111). At short deposition time, the deposition rate (given by the slope of the plot) is nearly independent of the applied potential (0.1 ML/s). For longer deposition times, the deposition increases with more negative applied potential, in agreement with expectations. Values range between 0.027 and 0.09 ML/s.

In Figure 4.3 we present a XRD diagram of 20 ML-thick Ni/Au(111) layer passivated by CO adsorption. The incidence angle is 0.6° and the detector parameters (γ = 14.44° and θ = 42.56°). The peaks at -6.36°, 113.77° and 233.9° are consistent with (-111), (1-11) and (11-1) nickel planes, which implies the epitaxial relationship Ni(111)<11-2> ‖ Au(111) <11-2>. The three other peaks arise from the 6-fold symmetry of the surface and they correspond to the same structure but rotated by 180°. Notice that the intensity of the two families of peaks are scaling with that of the Au(111)/Si(111) substrate (see chapter 2.2.1). This point was not father investigated. We also characterized at SOLEIL Au/Ni(2 and 5 ML)/Au(111) structures (see Fig.

4.3b and c), The diagram of the 5 ML-thick film is identical to that of the thicker layer. For the 2 ML-thick film one remarks that the two families of peaks have the same intensity. Looking into more details these diagram, we find that the FWHM of peaks decreases from 3.2° to 1.2° between 2 and 20 ML. From the peak position in each diagram we also infer a small lattice expansion, which decays from 1.5% (2 ML) to 0.42 % (5ML and above). The comparison of experimental and calculated EXAFS spectra (Fig. 4.4) confirms the fcc structure of the 5 ML Ni layer.
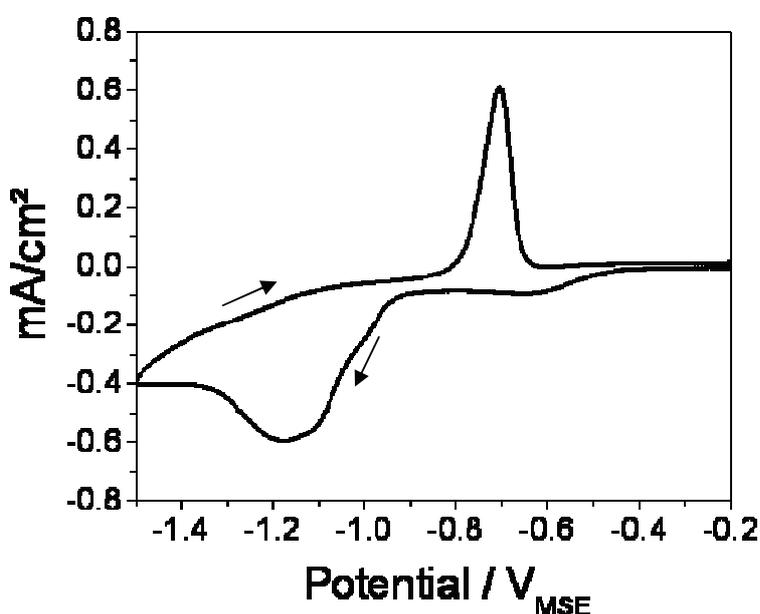
Figure 4.1 : CV of a Au(111)/Si(111) electrode in a Ni 0.5 mM solution. The potential was scanned from -0.2 V towards -1.5 V and back to -0.2 V at a rate of 50 mV/s. See text for the assignment of peaks. The reference electrode is a mercury sulfate electrode (MSE).
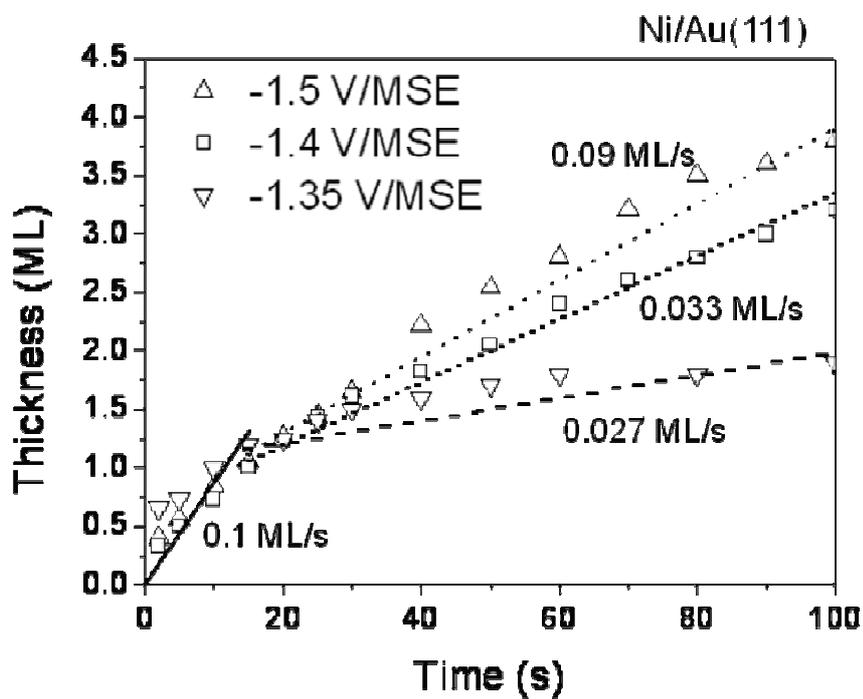
Figure 4.2: Variations of the Ni average thickness as a function of deposition time. The applied potential is -1.35 V (down triangle), -1.4 V (square), -1.5 V (up triangle) and -1.6 V (circles). The solution is a 0.5 mM NiSO$_4$ (see text for exact bath composition). Potentials are quoted versus MSE.
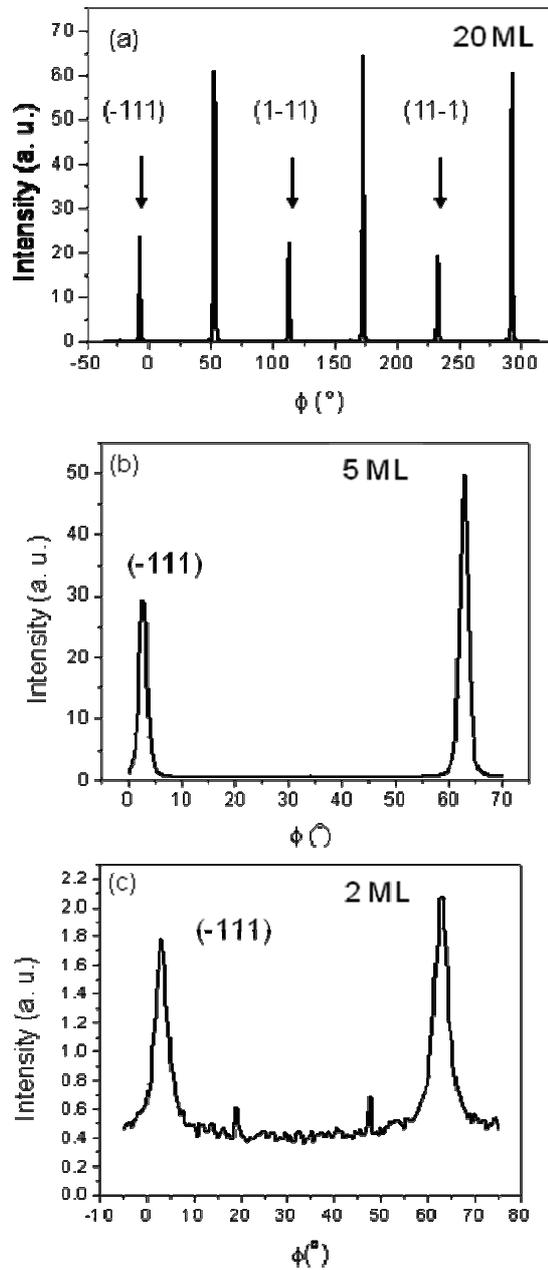
Figure 4.3: (a) X-ray diffraction diagram for a 20 ML-thick Ni(111)/Au(111) layer electrodeposited at U **= -1.3 V. peak assignment is indicated in the figure. The detector was positioned in the Bragg condition for (11-1) planes for the wavelength is** λ **= 1.54 Å. (b-c) Narrow XRD scans for Au(10ML)/Ni/Au(111) structures with a Ni thickness of 5 and 2 ML (deposition potential** U **= -1.5 V). The spectra were obtained at SOLEIL with** λ **= 1.7712 Å,** E **= 7 keV, which explains that the Φ-value for the (-111) peak. Is shifted with respect to (a).**
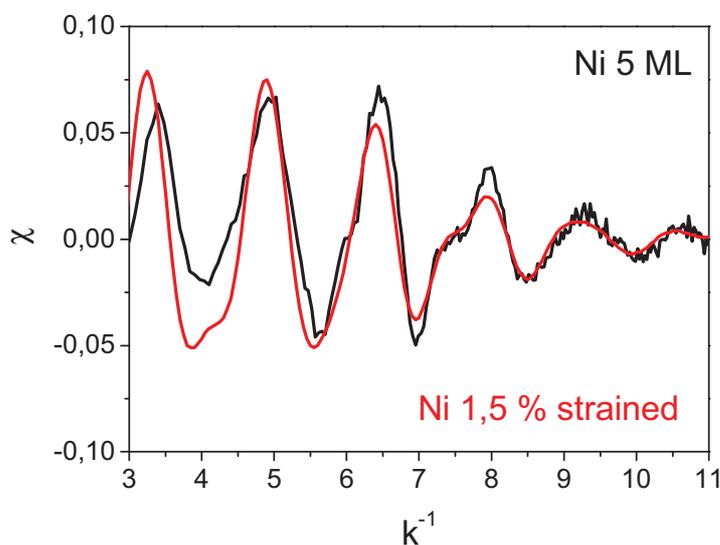
Figure 4.4: EXAFS spectrum of the sample characterized in the 5 ML-thick Ni layer sandwiched between Au. Experimental data (black line) and simulation of Ni 5 ML dilated 1.5% (red line) sandwiched by gold.

The above data are consistent with previous *in situ* STM observations[2] an example of which is presented in Figure 4.3. This image confirms that the first Ni monolayer grows 2D and is completed before the next atomic plane nucleates. Growth continues in a layer by layer mode. The numbers in the image are the local film thickness expressed in atomic planes. Also quite characteristics of the topography of Ni/Au(111) layers, is the periodic hexagonal long range corrugation (period ~21 Å) visible on terraces which arises from the mismatch between Ni(111) and Au(111) in plane lattices. The period ~21 Å means residual strain ~ 1.5%, which has a perfect agreement with the above XRD characterizations. As a whole *relaxed* Ni(111) layers are growing in epitaxy with Au(111). Very important to this work, the growth rate is compatible with experimental requirements for MOKE measurements and obtaining one monolayer is very easy because of the decrease of the growth rate in the multilayer regime, which is consistent with previous measurements.[2]
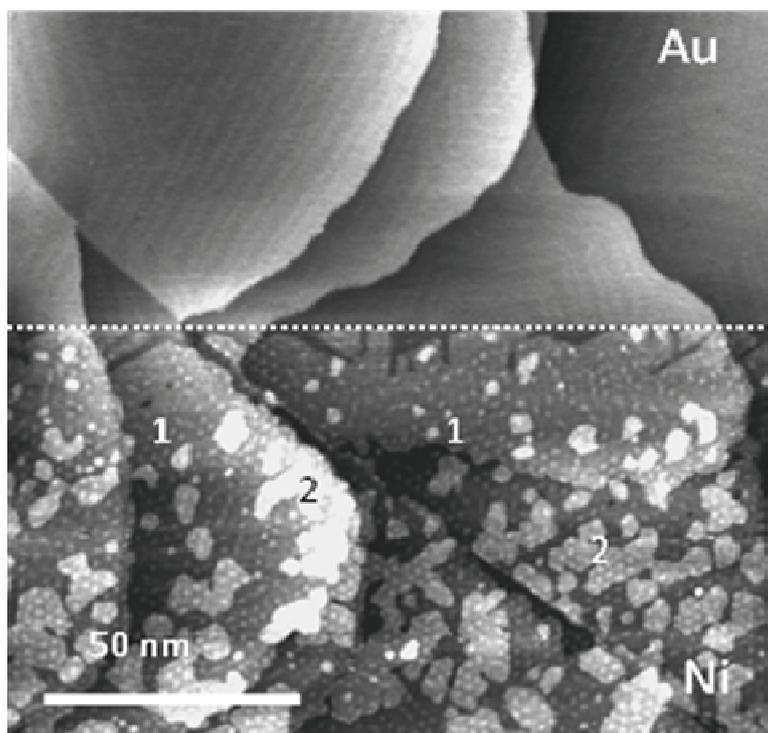
Figure 4.5: *In situ* **STM observation of Ni/Au(111) growth at** U = -1.3 V_{MSE} **in a 1mM mM NiSO$_4$ solution. After Ref.** [2]**.**

4.2.2 Magnetic properties

In LMOKE we obtain almost square hysteresis loops (data not shown) after an "induction" time of Ni deposition. PMOKE hysteresis loops are always reversible linear loops. Figure 4.6 summarizes *in situ* MOKE results by plotting the thickness dependence of the magnetization measured at a fixed field H = 600 Oe in LMOKE (Fig. 4.6a) and PMOKE (Fig. 4.6b). These plots evidence that no magnetization is measurable below 2 ML. This is consistent with the thickness dependence of the Curie temperature of thermally deposited Ni layers in vacuum (see Fig. 3.22).[7] T_C is in fact close to RT for 2ML-thick TD Ni films. Between 2 and 8 ML, M// increases but without full remanence and $M\perp$ is hardly measurable. The magnetization of the film is not yet total. This is only *above* 8 ML that the parallel component M// becomes strictly proportional to Ni thickness since the straight line intersects the origin. Full remanence is also achieved (Fig. 4.6a, open symbols). LMOKE and PMOKE results indicate therefore that

layers thicker than 8 ML are *fully* magnetized. In other words the absence of magnetism below 2ML does not correspond to a so called dead magnetic layer. In the case of a dead magnetic layer, the straight line would not intersect the origin.

Figure 4.7 compares the thickness dependence of the magnetic moment (symbols, data expressed in a.u.) with theory. The solid line (red) was calculated by combining the expressions $\mu(RT)/\mu_B(0\ K) = (1-T/T_C)^\beta$ and $T_C/T_C(\infty) = 1 - (n_0/n)^{\lambda}$.[8], with $\beta = 0.3$,[9] $n_0 = 1$ ML and $\lambda \sim 1.5$. There is an obvious disagreement between theory and experiment for Ni thickness smaller than ~6 ML. This suggests that a supplementary phenomenon occurs at the electrochemical interface. A likely explanation is H-*absorption* since Ni electrodeposition occurs in parallel with the reduction of protons (Fig. 4.1) a reaction which produces H-species susceptible to be incorporated into the nickel matrix in the initial stages[10]. H-incorporation seems to be responsible for a further decrease of the magnetic moment[10].
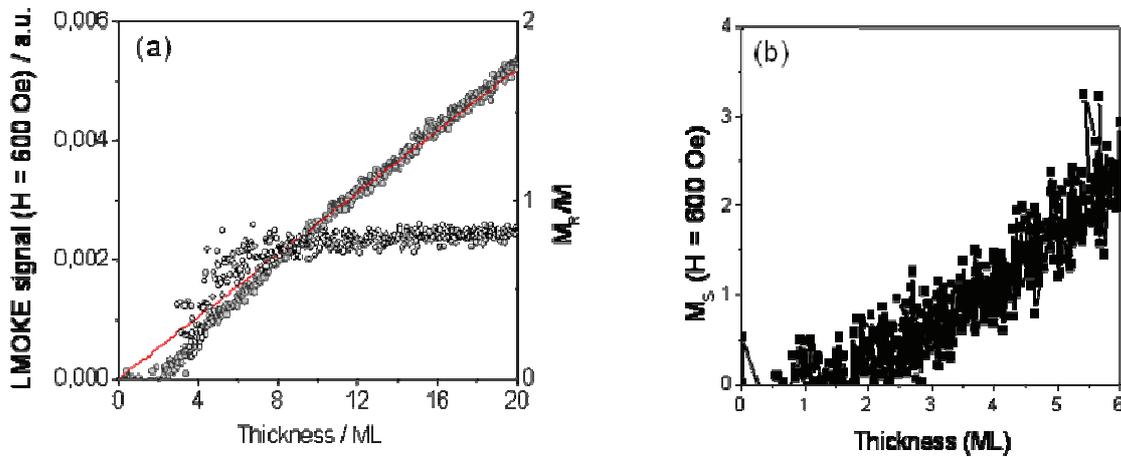
Figure 4.6: *In situ* **MOKE. (a) LMOKE: thickness dependence of $M//$ and M_R/M_{600}. (b) PMOKE: thickness dependence of $M\perp$. The magnetization components M// and $M\perp$ are measured at $H = 600$ Oe. The deposition potential is $U = -1.5$ V$_{MSE}$.**
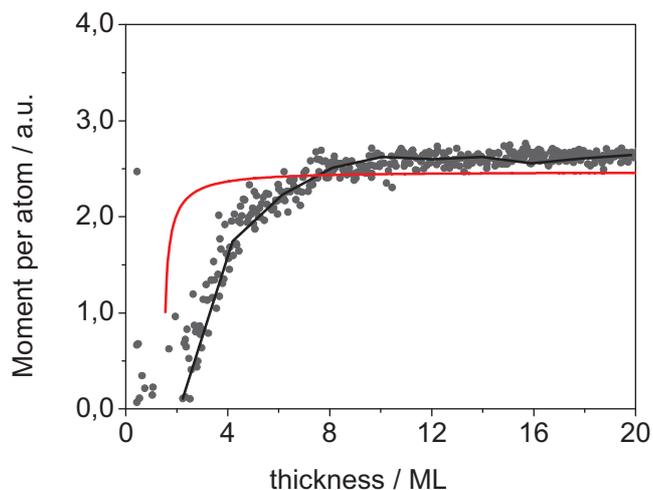
Figure 4.7: Comparison between experimental (symbols) and theoretical (red solid line) thickness dependence of the magnetic moment of a growing Ni/Au(111) layer.

4.2.3 Conclusions

In conclusion, electrodeposited Ni/Au(111) layers grow 2D. They are Ni(111) layers with nearly no elastic strains in epitaxy with Au(111). Below 2 ML, layers are not ferromagnetic at room temperature. Full ferromagnetism is established above 8 ML only. At this thickness there is a strong in plane anisotropy. Between 2 and 8 ML, H-absorption probably slows down the increase of the magnetic moment with respect to expectations.

4.3 Structure and magnetism of Fe/Ni/Au(111) layers

4.3.1 Growth mechanism and structure

a) Growth rate:

The Ni(111) layer was deposited as explained in the previous section. Its thickness was adjusted to the desired value. After deposition, it was stabilized by applying $U = -1.1$ V while flushing the MOKE cell with the supporting electrolyte for 15 min (flow rate 2 mL/min). Only then, the solution containing 0.5 mM of Fe was continuously passed. In what follows the

potential is kept < -1.1 V to avoid Ni dissolution. Figure 4.8 compares the cyclic voltammograms (CV) of a Au(111) (dashed line) and Ni(1ML)/Au(111) (solid line) electrodes in the 0.5 mM FeSO$_4$ solution used in chapter 3. To avoid Ni dissolution the potential excursion was restricted to U < -1.1 V. The peak assignment is the same as in Fig. 3.2. Peaks C3/A1 stand for Fe deposition/dissolution and peak C2 for HER. One notices two important differences between the two substrates:

- Peak C2 is not quite visible at the Ni/Au electrode. This is because the solution is *depleted* in protons close to the electrode surface. Protons are indeed continuously reduced since the potential is maintained negative of -1.1 V.

- Peaks C3/A1 are shifted in the potential scale from one curve to the other. This indicates that Fe deposition is *slower* on Ni/Au than on bare Au. Fe dissolution is also *slower* from Ni/Au than from bare Au. As a consequence of these changes we adapted the potential routine used in MOKE experiments to be certain that all the iron was dissolved at -1.1 V. As shown in Fig. 4.9, an anodic charge is measured after the potential reached -1.1 V.
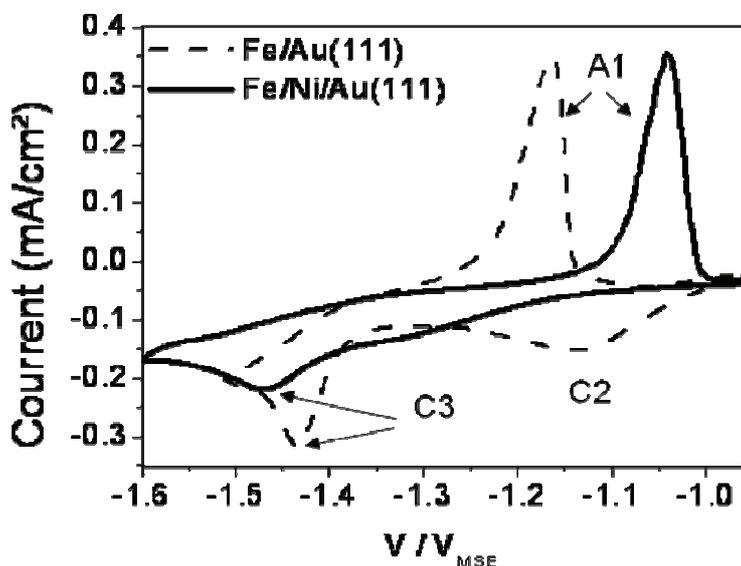
Figure 4.8: Cyclic-voltamograms of Fe/Au(111) (dashed line) and Fe/Ni/Au(111) (solid line) electrodes in the iron containing solution (0.5 mM FeSO$_4$). Potentials are measured versus MSE. The sweep rate is 50 mV/s.
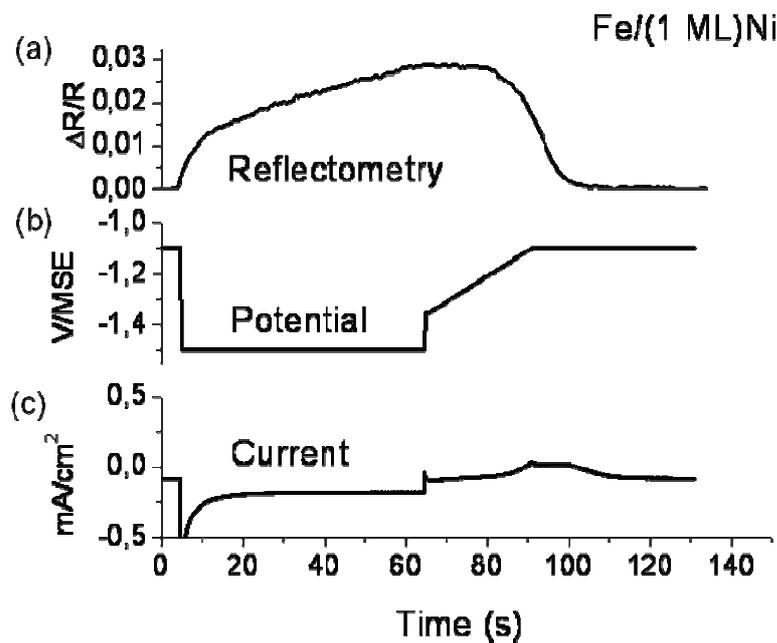
Figure 4.9: Time dependence of the surface reflectivity (a), potential (b) and current (c) during Fe deposition on Ni/Au(111) at *U* = -1.5V. The Fe dissolution occurs when the Ni equilibrium potential was applied.
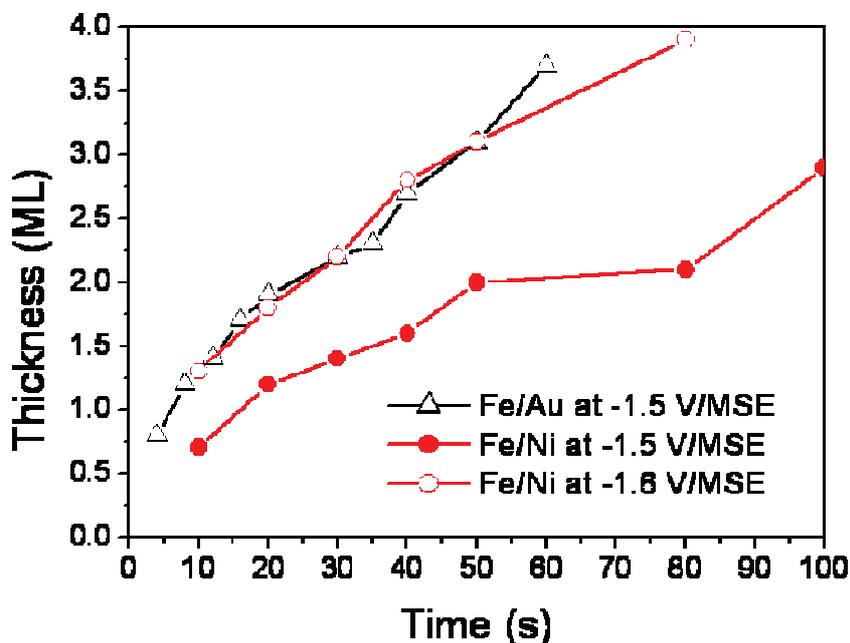
Figure 4.10: Variations of the iron thickness as a function of deposition time. Red symbols correspond to Fe/Ni/Au(111) deposition at -1.5 V (filled circles) and -1.6 V (open circles). Black symbols refer to Fe/Au deposition at -1.5 V. The reference of potential is MSE.

Figure 4.10 shows the variations of the iron thickness (determined using the stripping method) as a function of deposition time on Fe/Au (black symbols) and Fe/Ni/Au(111) (red symbols). Comparing data for U = -1.5 V confirms that the kinetics of deposition is slower on a Ni covered Au(111) surface than on bare Au(111). One needs to apply U = -1.6 V to achieve a comparable deposition rate.

b) Morphology:

Figure 4.11 shows two *in situ* STM images of the Ni/Au(111) electrode before (a) and after (b) iron deposition. The Ni layer was deposited at U = -1.24 V in 19s and to image it, the potential was -1.1 V. The average Ni thickness is 1.2 ML and one recognizes the characteristic moiré structure, even though the tip resolution was not excellent. The light gray islands

90

correspond to the second Ni monolayer. After exchange of the Ni solution with the iron, iron was deposited at $U = $ -1.5 V in 30s. The Fe/Ni film was imaged at -1.36 V. A smooth morphology is maintained. As a whole a lateral expansion of the previous islands is observed, this means that a Fe monolayer has preferentially nucleated at the Ni step edges. Iron growth is therefore essentially 2D on Ni(111). The coverage in this image is estimated to be ~0.7 ML.

1.2ML Ni(111)/Au(111)　　0.7 ML Fe/Ni(1ML)/Au(111)

Fe
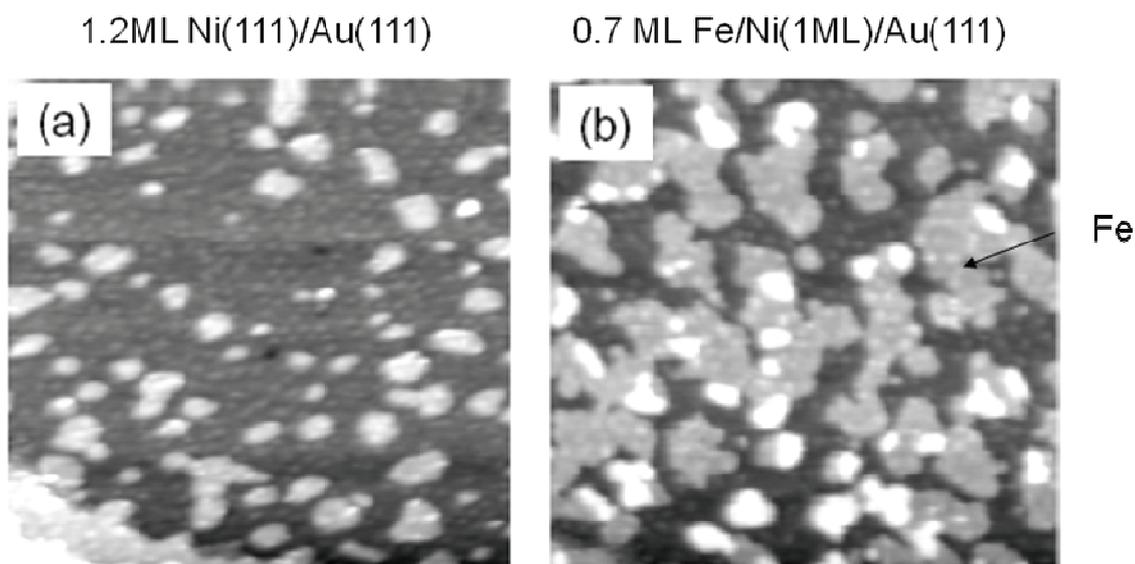
Figure 4.11 – *In situ* STM images (a) Ni/Au(111) deposited at *U* = -1.24 V in 19s and to image it, the potential was -1.2 V, and (b) 0,7 ML of Fe/Ni/Au(111) deposited at *U* = -1.5 V in 30s and imaged at -1.36 V. Iron growth is therefore essentially 2D on Ni(111).

c) Structure

The sample studied by x-ray diffraction at SOLEIL ($\lambda = 1.7712$ Å, $E = 7$ keV) was a 3ML Fe film deposited at -1.5 V on Ni(1ML)/Au(111). It was covered by 10 ML of Au. Figure 4.12 presents the XRD diagram obtained in the same conditions as in Fig. 3.9 (incidence angle 0.6°, detector angles $\gamma = 46.70°$ and $\delta = 25.665°$). As in Fig. 3.9c, the peak can be decomposed into three components. The central peak is again assigned to gold (10l) [11], and two satellite peaks at $\Phi = 53.54°$ and 65° are assigned to bcc Fe(110) with the same in plane orientation Fe(110)<001> || Au(111)<1-10> as the one shown in Fig. 3.12. Because the Ni interlayer is in epitaxy with Au(111), without any in plane rotation of its lattice, we conclude that the bcc Fe(110) film is in epitaxy with the Ni(111) according to the relationship Fe(110)<001> ||

91

Ni(111)<1-10> (Fig. 4.13). The difference with respect to the case of Fe/Au(111) layers concerns the separation angle $\Delta\Phi = 10.78°$ in Fig. 4.12. We hence conclude that the elastic strains are essentially relaxed, which is remarkably different from the case of Fe/Au for which strains amounted to ~8% at a comparable Fe thickness (see Fig. 3.14).
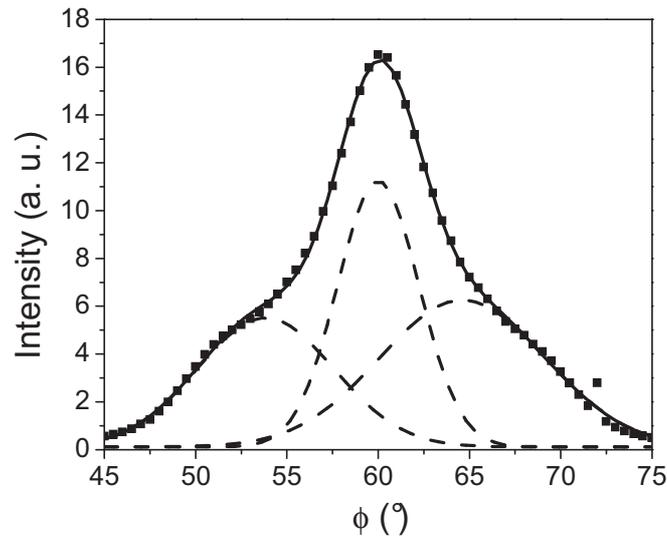
Figure 4.12: Narrow X-ray diffraction spectra of a 3 ML thick Fe layer deposited at -1.5 V on Ni(1ML)/Au(111). Measurement performed at SOLEIL (λ= 1.7712 Å, E = 7 keV). The incident angle is 0.6° and the detector position γ = 46.70° and δ = 25.665°. The spectra is decomposed into 3 peaks: the central one is related to Au(10l) rod. The two others are related to bcc Fe(110). These are consistent with the epitaxial relationship Fe(110)<001> ll Ni(111)<1-10>. The separation angle $\Delta\Phi$ = 10.78° measured between the two Fe related peaks indicates that the iron layer is unstrained.
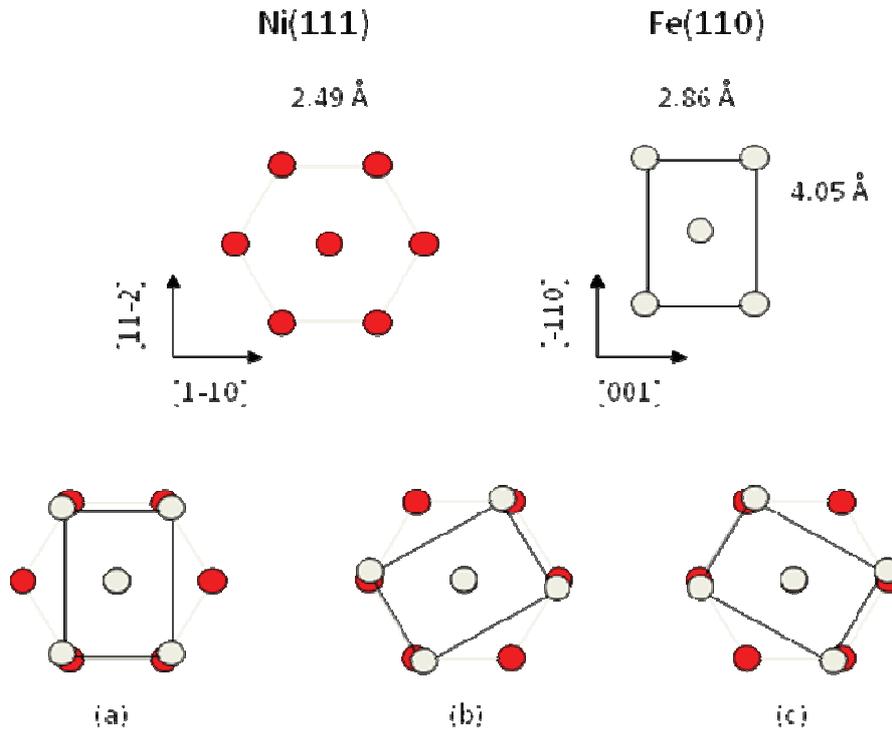
Figure 4.13: Atomic structure of Ni(111) and bcc Fe(110) oriented surfaces. Scheme (a) corresponds to the epitaxial relationship Fe(110)<001> ‖ Ni(111)<1-10> derived from the XRD pattern in Fig. 4.12. Schemes (b-c) are the two other possible arrangements for the Fe(110) lattice on Ni(111).

Table 4.1: EXAFS calculation assuming different layer structures for the Fe(3 ML)/Ni(1 ML)/Au(111) sample. The last columns give the parameters corresponding to best fit with experimental curves. See text for the definition of parameters. Parameters with (*) are imposed.

layer	structure	ΔN / %	σ / pm	ΔE_0 / eV	Chi^2
Fe	3 ML Relaxed bcc Fe(110)	-40	7.5	4	458
		-20*	11	4	470
		0*	13	4.2	506
	3 ML relaxed bcc Fe(110) + fcc Fe (75 : 25)	-15.5	9	1.5	334
Ni	1 ML fcc Ni	-15	11.5	2	368
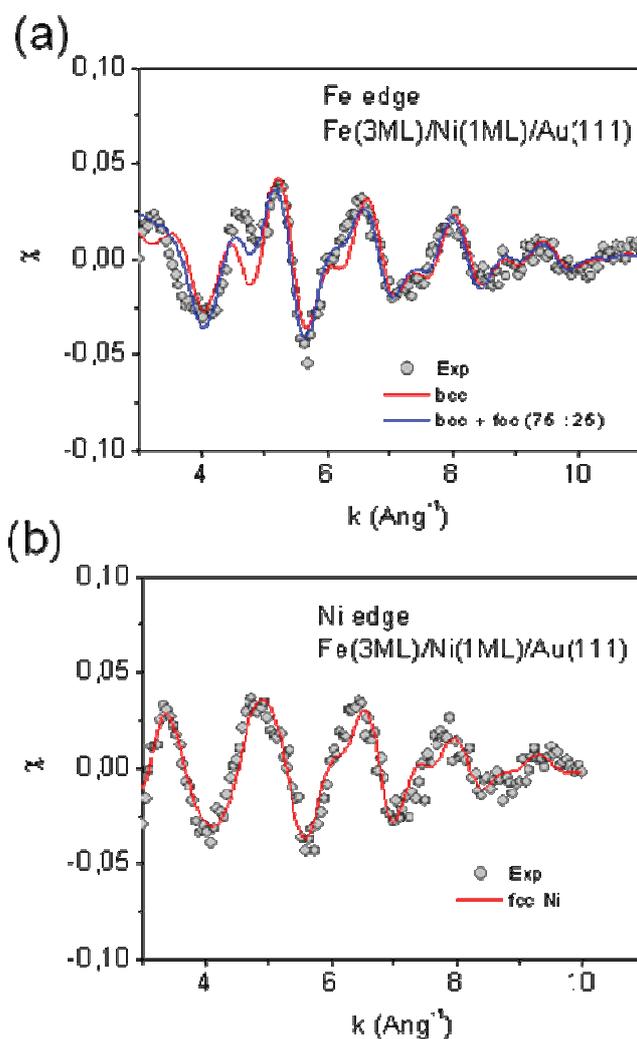
Figure 4.14: Comparison between experimental (symbols) and calculated (solid lines) EXAFS results for the Fe(3 ML)/Ni(1 ML)/Au(111) sample studied in Fig. 4.12. (a) Spectrum at Fe Kα edge; (b) Same at Ni Kα edge. In (a) the red curve is calculated for a pure and relaxed 3 ML-thick bcc Fe(110) layer; The blue curve, calculated for 3 ML-thick mixture (75:25) of bcc Fe(110) and fcc Fe(111), gives a better fit (see Table 4.1). In (b) the solid line is calculated for a pure and relaxed 1 ML-thick fcc Ni(111) layer.

The above sample was also investigated by EXAFS at Fe (Fig. 4.14a) and Ni (Fig. 4.14b) Kα edges. Table 4.1 lists the parameters derived from the fit. Results show that the iron layer is essentially bcc Fe(110) with the probable presence of fcc Fe(111) since this assumption significantly improves the chi^2. The Ni monolayer is well accounted for by a relaxed fcc Ni(111)

94

monolayer film. It should be noted that ΔN and s are still coupled parameters and that their rather large value express disorder.

d) Conclusions:

The results above indicate that Fe/Ni(111) growth is essentially a 2D process which leads to epitaxial *unstrained* bcc Fe(110) layers above 3 ML (see XRD Fig. 4.12 and EXAFS 4.13). The epitaxial relationship is Fe(110)<001> ‖ Ni(111)<1-10> . EXAFS suggests that the existence of a fcc phase below this thickness (Fig. 4.14a). Even though additional work is necessary, especially STM observations, we infer, in analogy with Fe/Au(111) growth (see Chapter 3), that fcc Fe(111) phase formation is plausible on Ni(111). We also recall that fcc Fe(111) is obtained by thermal deposition on Ni(111).[4] This result may look surprising since there is nearly no lattice mismatch between fcc Fe(111) and Ni(111). It is seems neverthelesss impossible to stabilize the fcc iron phase above 3 ML. We will see in the next paragraph whether the magnetic measurements yield complementary information about this point.

4.3.2 Magnetic properties of Fe/Ni/Au(111): results and discussion

P- and L-MOKE measurements were performed on Ni/Au(111) electrodes with different Ni coverages. Iron was deposited at U = -1.5 V/MSE from a 0.5 mM $FeSO_4$ solution. Before each experiment a few Fe deposits were characterized to have semi-quantitative calibration of the MOKE signal and thereby compare Fe/Au with Fe/Ni experiments.

The PMOKE measurements for Fe upon Ni are shown in the Figure 4.15. As discussed earlier these data indicate that a SRT perpendicular to in plane direction occurs again upon Fe on Ni/Au(111) electrochemical growth. One also notices a *downward* curvature of the M – thickness plot in the very initial stages of Fe/Ni/Au(111) growth, whereas it is upward during the initial stages of Fe/Au(111) growth (black curve in Fig. 4.15a). This means that the total magnetic moment is greater than with the Fe pure. Comparing the average slopes of the M – thickness peaks for Fe/Ni and Fe/Au below 2 ML, suggests that the Ni interlayer is perpendicularly

magnetized as soon as Fe is deposited. This piont will be discussed later. Looking at the variations of M_R/M_{600} (Fig. 4.15b) reveals that the presents of an Ni interlayer, even at subsurface coverage, shifts towards smaller thickness the onset thickness above which full premanece is obtained. For a Ni coverage equal or larger than 1 ML, full remanence occurs above 0.2 ML of ron. The same plots reveal a significant decrease of the iron critical thickness t^* (see Fig. 4.15b). The thickness dependence of LMOKE signal for Fe/Ni/Au(111) is plotted in Fig. 4.16a. In agreement with Fig. 4.15, there is no LMOKE signal below 1 ML because the magnetization is strictly perpendicular. Above ~1.5 ML the LMOKE signal is proportional to the amount of Fe deposited. Figure 4.16b presents the variations of the coercive field of 2.5 ML-thick iron films as a function of the thickness of the Ni interlayer.
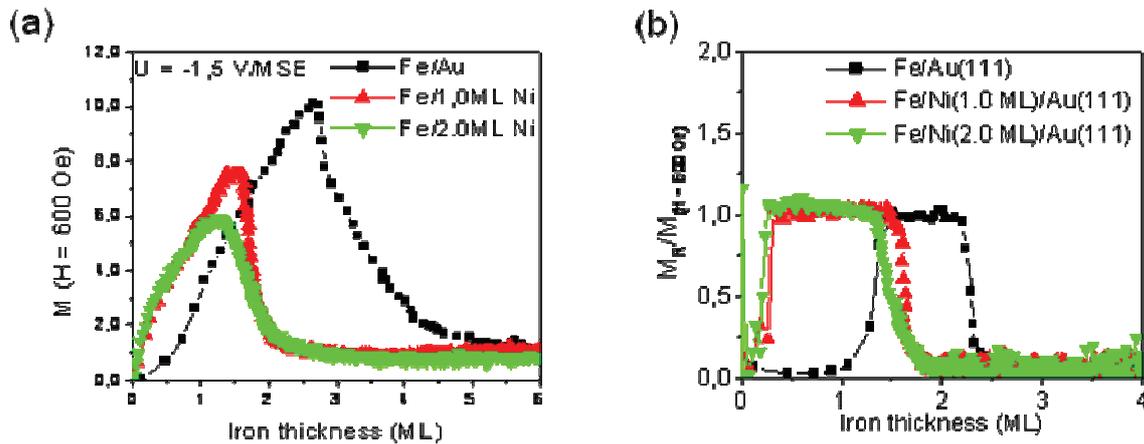
Figure 4.15: *in situ* **PMOKE results recorded during Fe deposition on Ni/Au(111): (a) thickness dependence of MOKE signal measured at H = 600 Oe. (b) Corresponding variations of $M_R/M_{600\ Oe}$ The deposition potential is U = -1.5 V_{MSE} as indicated in the figures. The Ni coverage is 0.6 ML (red curve), 1.0 ML (green curve) and 2.0 ML (blue curve). For comparison, the black curve corresponds to Fe/Au.**

Préciser iron thickness
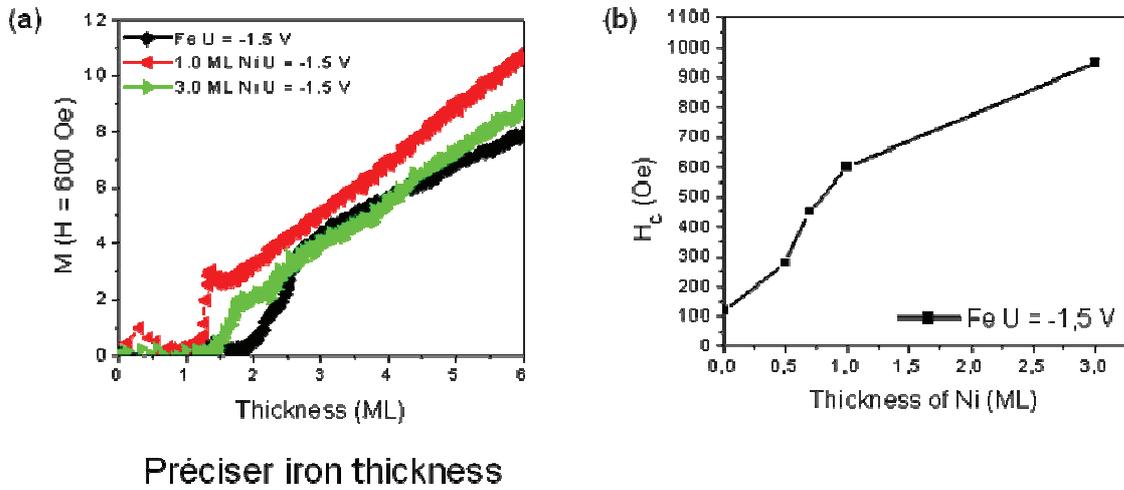
Figure 4.16: *In situ* **LMOKE results recorded during Fe deposition on Ni/Au(111): (a) thickness dependence of MOKE signal measured at** H **= 600 Oe. (b) orecive field** H_C **of 2.5 ML-thick fe layers deposited on Ni interlayers with increasing thickness The deposition potential is** U **= -1.5** V_{MSE}**.**
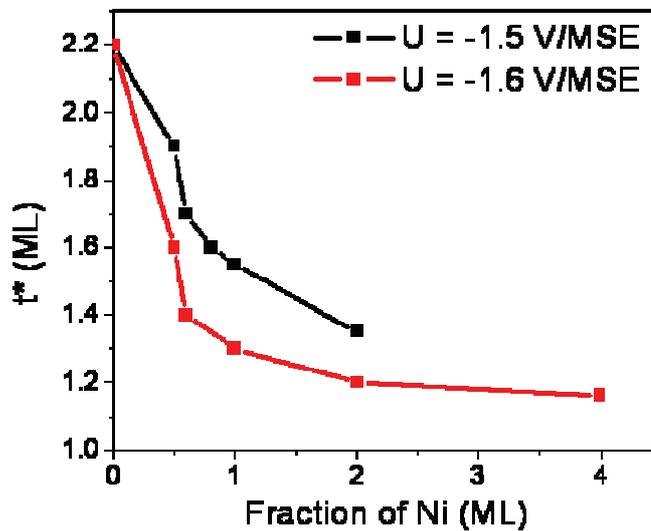
Figure 4.17 - Thickness of magnetic reorientation (t*) versus the ML of Ni as substrate. Exponential decrease is observed for both -1,5 and -1,6 V/MSE.

Figure 4.18 presents a specific LMOKE experiment intended to determine how many atomic planes of a thick in plane magnetized Ni layer may be perpendicularly magnetized upon Fe deposition on top of it. A 12 ML-thick Ni layer was first deposited ($U = -1.5$ V), giving rise to square magnetization curves (not shown). At the end of Ni deposition, the film was stabilized at -1.1 V and the $NiSO_4$ solution exchanged by the $FeSO_4$ solution. Fe deposition was then initiated by applying $U = -1.5$ V. at time t = 5s marked by the vertical line in the different panels of Fig. 4.18. Panels (a) to (c) respectively show the *time* dependence of the overall moment of the film measured for $H = 600$ Oe, of the ratio $M_R/M(H=600$ Oe) and of the coercive field H_C. A dip is clearly observed in curves in (a) and (b) in the very initial stages of Fe growth. The maximum corresponds to an iron thickness ~ 1.0 ML. At such a thickness the Fe/Ni is perpendicularly magnetized (Fig. 4.15). The reduction of the overall moment in Fig. 4.18a indicates therefore that a fraction of the Ni layer is perpendicularly magnetized. From the depth of the minimum, 3 ML are concerned. This interpretation is consistent with the corresponding dip in remanence. The dip in remanence (Fig. 4.18b) indicates indeed a transient rotation of the easy axis of magnetization towards out of plane direction. This experiment therefore confirms that the moment of the Ni monolayer in Fig. 4.18 is indeed magnetically coupled with the perpendicular moment of the iron layer below 1.5 ML. the large increase of the coercive field upon Fe deposition is quite surprising (Fig. 4.18c). The H_C value is indeed as large as 700 Oe, which than that of the 12 ML-thick Ni layer (150 Oe) or that of the pure Fe/Au layer (140 Oe) of comparable thickness (the Fe thickness is estimated to be 3,0 ML at the end of the experiment presented in Fig. 4.18). This unexpected behavior would deserve additional characterization and was not further investigated. It outlines a specific magnetization reversal mechanism.
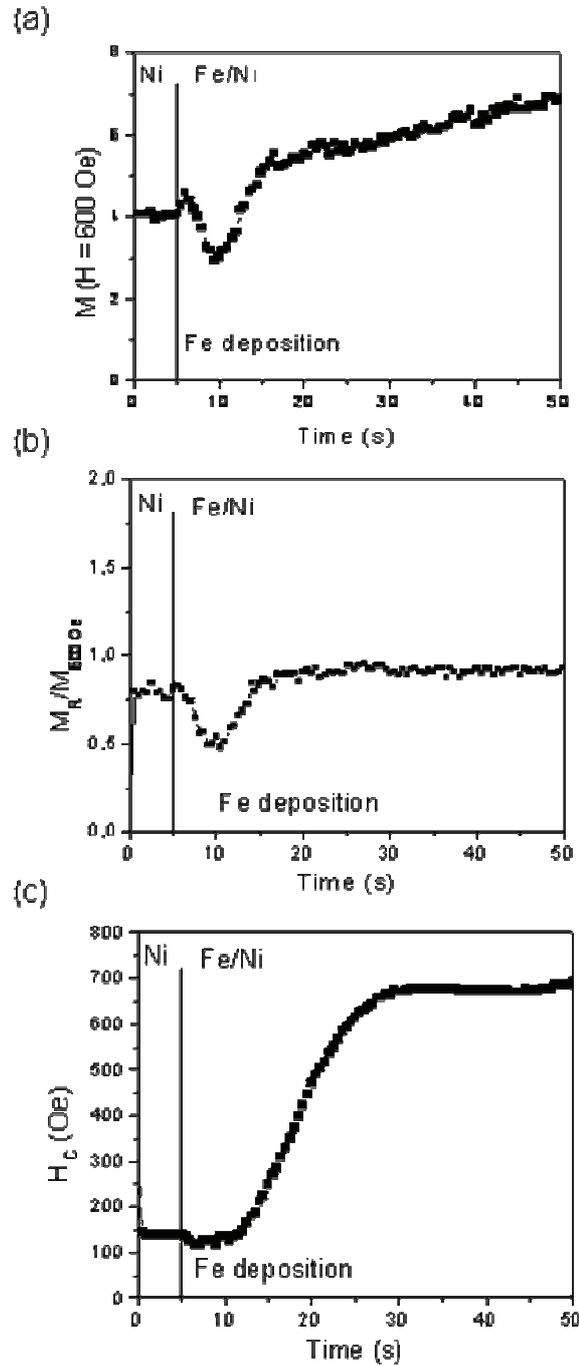
Figure 4.18 – Real time LMOKE experiment showing the influence of depositing a Fe layer on a 12 ML-thick Ni/Au(111) substrate. Fe is deposited at $U = -1.5$ V$_{MSE}$ at time t = 5s. (see vertical line). (a) time dependence of magnetization measured at $H = 600$ Oe, (b) remanence M_R/M and (c) coercive field H_C.

4.4 General conclusions

Ni/Au(111) layers are relaxed epitaxial layers which grow 2D. They are not ferromagnetic below 2 ML. at room temperature because of a reduction of the Curie temperature. Above 8 ML the film becomes fully magnetized and the easy axis of magnetization is in the surface plane. Iron growth on Ni/Au(111) substrate resembles very much Fe/Au(111) growth, with a structural phase transition fcc Fe(111) → bcc Fe(110). The main difference between the two systems concerns the amount of strains which is negligible at Fe/Ni layers. As a result the perpendicular magnetization anisotropy is reduced at Fe/Ni interface due to a reduction of magnetoelastics effects.

The Fe/Ni/Au(111) system presents however unique properties. Below 1.2 ML, there is an exchange coupling between the perpendicularly magnetized Fe layer and Ni layer. We found that the coupling extends over 3 Ni atomic planes. At larger iron thickness, the bilayer Fe/Ni is in plane magnetized and presents a surprising magnetization reversal with a huge coercive field.

4.5 Bibliography:

[1] F. A. Moller, J. Kintrup, A. Lachenwitzer et al., "In situ STM study of the electrodeposition and anodic dissolution of ultrathin epitaxial Ni films on Au(111)," Phys. Rev. B **56** (19), 12506-12518 (1997).

[2] P. Allongue, L. Cagnon, C. Gomes et al., "Electrodeposition of Co and Ni/Au(111) ultrathin layers. Part I: nucleation and growth mechanisms from in situ STM," Surf. Sci. **557** (1-3), 41-56 (2004).

[3] S. D'Addato, L. Pasquali, G. C. Gazzadi et al., "Growth of Fe ultrathin films on Ni(111): structure and electronic properties," Surf. Sci. **454-456**, 692-696 (2000).

[4] G. C. Gazzadi, F. Bruno, R. Capelli et al., "Structural transition in Fe ultrathin epitaxial films grown on Ni(111)," Phys. Rev. B **65** (20), 205417 (2002).

[5] An Bai, Zhang Lin, Fukuyama Seiji et al., "Growth and structural transition of Fe ultrathin films on Ni(111) investigated by LEED and STM," Physical Review B (Condensed Matter and Materials Physics) **79** (8), 085406 (2009).

[6] Ruqian Wu and A. J. Freeman, "Structural and magnetic properties of Fe/Ni(111)," Phys. Rev. B **45** (13), 7205 (1992).

[7] P. J. Jensen and K. H. Bennemann, "Magnetic structure of films: Dependence on anisotropy and atomic morphology," Surf. Sci. Rep. **61** (3), 129-199 (2006).

[8] F. J. Himpsel, J. E. Ortega, G. J. Mankey et al., "Magnetic nanostructures," Advances in Physics **47** (4), 511 - 597 (1998).

[9] F. Huang, M. T. Kief, G. J. Mankey et al., "Magnetism in the few-monolayers limit: A surface magneto-optic Kerr-effect study of the magnetic behavior of ultrathin films of Co, Ni, and Co-Ni alloys on Cu(100) and Cu(111)," Phys. Rev. B **49** (6), 3962 (1994).

[10] J. K. Blum and W. Göpel, "Influence of hydrogen chemisorption on the magnetism of thin nickel films," Thin Solid Films **42** (1), 7-15 (1977).

[11] S. Brauer, G. B. Stephenson, and M. Sutton, "Perfect Crystals in the Asymmetric Bragg Geometry as Optical Elements for Coherent X-ray Beams," Journal of Synchrotron Radiation **2** (4), 163-173 (1995).

[12] J. Stöhr, "Exploring the microscopic origin of magnetic anisotropies with X-ray magnetic circular dichroism (XMCD) spectroscopy," Journal of Magnetism and Magnetic Materials **200** (1-3), 470-497 (1999).

[13] E. Martinez, R. C. Longo, R. Robles et al., "Structure and magnetic properties of small Fe clusters supported on the Ni(001) surface," Physical Review B (Condensed Matter and Materials Physics) **71** (16), 165425 (2005).

[14] J. â€‰ T. Lau, A. Föhlisch, R. NietubycÌ€ et al., "Size-Dependent Magnetism of Deposited Small Iron Clusters Studied by X-Ray Magnetic Circular Dichroism," Phys. Rev. Lett. **89** (5), 057201 (2002).

[15] P. Allongue, L. Cagnon, C. Gomes et al., "Electrodeposition of Co and Ni/Au(1 1 1) ultrathin layers. Part I: nucleation and growth mechanisms from in situ STM," Surface Science **557** (1-3), 41-56 (2004).

Chapter 5

Magnetic and structural characterizations of electrodeposited ultrathin Fe_xNi_{1-x} alloy layers

5.1.   Introduction

Bi−metallic magnetic alloys have attracted a lot of interest since at least one century. For example, the discovery of the permalloy material ($Ni_{80}Fe_{20}$) took place in the Bell labs in 1914 by Gustav Elmen. Later, a permalloy with a slightly modified composition (addition of 2% of molybdenum) was used in the long distance phone copper lines, thus improving by a factor of ten the transmission speed. More recently, a special interest for magnetic alloys rose for data storage application purposes. They are indeed intensively used for the fabrication of the active layer of the hard disks [1] as well as of the hard disk read−head sensors [2]. Their wide application range originates from the possibility of tuning their magnetic properties (permeability, coercive field, magnetization, Curie temperature, magnetic anisotropy) by controlling their composition and their structure. Such a behavior has excited a lot the scientists since decades who studied these properties as a function of different parameters (alloy composition, alloy preparation conditions, substrate in the case of alloy films…), experimentally as well as theoretically, in order to give a correct explanation down to the atomic scale. A renew of interest concerning these materials grew in the last decade due to the possibilities offered first, by the development of experimental setups allowing the controlled growth and the characterization of alloy films at the atomic level, and second, the development of high speed computers allowing to improve the calculation quality and to take into account more sophisticated calculation parameters.

The case of FeNi alloys is of particular interest. As we explained above, $Fe_{20}Ni_{80}$ (permalloy) has a high magnetic permeability and a low coercivity. Another alloy composition, the $Fe_{65}Ni_{35}$ (called Invar) has also a particular behavior with a vanishing thermal expansion coefficient [3]. This is accompanied by a drop of the magnetic moment and of the Curie

temperature [4]. Moreover, at this alloy composition, a structural phase transition from fcc (Ni rich alloys) to bcc (Fe rich alloys) occurs. This phase transition has a large influence on the magnetic behavior, and more specifically on the magnetic state. Indeed, it has been shown that FeNi fcc phase may be in a low spin (LS) state or a high spin (HS) one, which are equally stable, whereas the HS is the only stable state for FeNi bcc phase [5]. The above mentioned properties are very sensitive to the alloy composition and homogeneity as well as to the strain in the case of an alloy film. For example, it has been shown that the fcc phase may be stabilized for Fe content larger than 65% in the case of an alloy film deposited on Cu(100) [6]. The preparation and the morphology (in the case of a film) of the alloy is thus a key issue for studying precisely its properties.

The nucleation and growth processes of alloys are a wide field of study. It is more complicated than the study of monometallic film because of the larger number of involved quantities. In the case of monometallic deposits, the study of the film morphology at different coverage and deposition temperatures allows the determination of atomic quantities like the diffusion energy barrier, using a mean field theory [7]. When two different atoms are co-deposited, the resulting deposit morphology will depend on the diffusion barriers of both metals as well as on the interaction energies between the two metals. A key issue in such studies is to determine the alloy phase (phase separation, solid solution) as a function of the substrate and the alloy film thickness. Indeed, it is sometimes found that the alloy phase in the ultrathin limit differs from the bulk one. Such studies were principally undertaken for surface alloy formation upon metal deposition and subsequent annealing inducing intermixing and alloy formation [8].

FeNi alloys films are usually prepared in ultra high vacuum (UHV) either by co-depositing Fe and Ni [6,9] or by depositing them in sequence followed by sample annealing to induce intermixing [10]. The latter technique is limited to substrates with high melting points, to avoid deposit atoms diffusion into the substrate. FeNi single-crystal alloys were also used, although it was shown in this case that the surface preparation induces a small Ni enrichment [11]. An alternative way to prepare FeNi alloy films is to use electrodeposition. In the same way as for the electrodeposition of monometallic film, a bi-metallic alloy may be deposited if both metallic cations are present in the deposition solution and the deposition potential is more negative than the Nernst potential of both metals. However, numerous experimental studies showed that it is particularly difficult to control precisely the alloy composition because the deposition rates of

both metals strongly depend on the deposition potential, on the solution pH in the film vicinity and on the metallic cation concentrations. Moreover, more peculiar processes may also take place, for example anomalous deposition, where the deposition rate of the less noble metal is strongly enhanced in the presence of the second metal. Several studies tried to disentangle all these dependencies [12,13]. However, these studies focused on relatively thick films (>100 nm) and may be hardly compared to ultrathin layers deposited in UHV. In particular, as explained above, the interesting structural and magnetic properties are present for ultrathin FeNi films, which necessitate a controlled preparation protocol.

In this chapter, we will focus on FeNi alloys, and study their magnetic properties in correlation with their structure as a function of the alloy composition. The magnetic properties of these alloys will be determined by in-situ magneto-optical Kerr effect (MOKE). As we will see in the following, such measurements and their careful analysis yield invaluable information regarding the critical thickness of the magnetization reorientation transition and the film magnetic anisotropy. However, as the relationship between the MOKE signal and the film magnetic moment is not straightforward, complementary ex-situ SQUID measurements were also performed. As explained above, the structure of these alloys is of primary importance to understand their magnetic properties. For this purpose, we used ex-situ X−ray diffraction (XRD) and extended X-ray absorption fine structure (EXAFS) to determine the alloy phase and to estimate the film strain. These measurements were mainly performed on the Soleil Synchrotron (Gif sur Yvette, France), on the DIFFABS line with the invaluable help of the beam line responsible Dominique Thiaudière. Few in-situ scanning tunneling microscope (STM) characterizations were also performed with by Corentin Gougaud and Alexis Damian to check the flatness of the FeNi alloy films.

5.2. Electrochemical characterizations

5.2.1. Determining the alloy composition and thickness

The most straightforward characterization of the Fe and Ni deposition/dissolution processes is cyclic voltammetry. Au(111) voltammetry in Ni^{2+} (respectively Fe^{2+}) containing solution has been presented separately in the former chapters 3 and 4. It is however interesting, for the sake of comparison to overlay these two voltammograms (Figure 5.1a). As explained in the previous chapters, the prominent cathodic peak at $\sim -1.3V$ in both voltammograms, and also present in the absence of Ni and Fe (dashed curve) corresponds to the proton reduction. In the Ni^{2+} containing solution (green curve) this peak overlaps with the Ni deposition one, and an additional peak at ~ -1.05 V appears. The latter peak has already been observed in previous studies and its attribution is still not clear [14]. It is usually absent in the few first voltammograms, and becomes significant after further cycling. However, as in typical MOKE experiments, a large number of deposition/dissolution sequences is performed, the voltammogram shown in Figure 5.1a is more representative. In the Fe^{2+} containing solution (red curve) the Fe deposition peak is at ~ -1.47 V, clearly separated from the proton reduction one. The dissolution peak of Ni (respectively Fe) can be clearly identified at -0.77 V (respectively $-1.24V$) and is marked by two dashed lines.
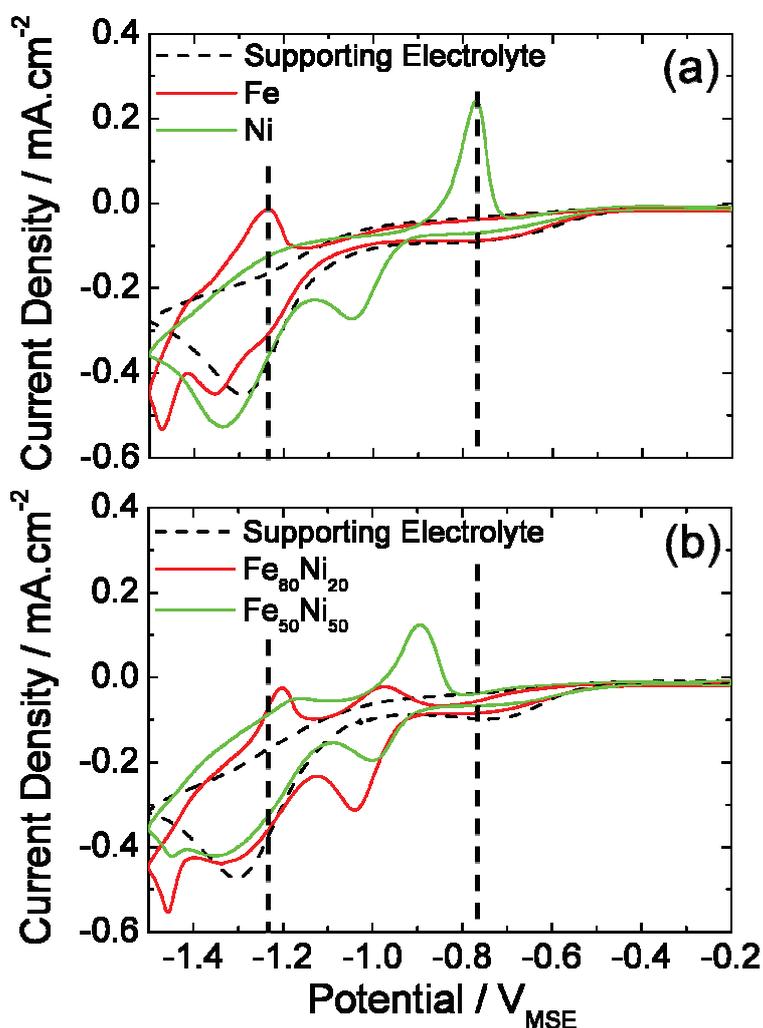
Figure 5.1 - : (a) cyclic voltammograms of Au(111) in supporting electrolyte 0.1M K_2SO_4 + 1mM H_2SO_4 + 1mM KCl (black dashed curve) containing 0.5 mM Fe^{2+} (red curve) or 0.5 mM Ni^{2+} (green curve). (b) Cyclic voltammograms of Au(111) in supporting electrolyte 0.1M K2SO4 + 1mM H2SO4 + 1mM KCl (black dashed curve) containing 0.4 mM Fe^{2+} + 0.1 mM Ni^{2+} (red curve) or 0.25 mM Fe^{2+} + 0.25 mM Ni^{2+} (green curve). The sweep rate is 50 mV/s. The two dashed lines in (a) and (b) indicate the position of Fe and Ni dissolution peaks in (a).

It may be interesting to study the voltammograms in the solution used for FeNi alloy deposition, i.e., in the presence of both ions Ni^{2+} and Fe^{2+} in the solution. Such voltammograms in Fe/Ni:80/20 and Fe/Ni:50/50 solutions are shown in Figure 5.1b. The main consequence of the decrease of the relative concentration of Fe^{2+} is a reduced Fe deposition/dissolution peaks. In the same way, the increase of the Ni^{2+} relative concentration induces an increase of Ni dissolution

peak. The proton reduction peak remains essentially unchanged whereas the variation of the peak at −1.04V is due to its evolution with time and is not strictly related to the change of the Ni^{2+} relative concentration. It is interesting to note that the position of the dissolution peaks of the alloys is within a potential range delimited by the position of pure Ni and pure Fe dissolution peaks (see dashed vertical lines). A more quantitative analysis of these curves is very complicated. Indeed, during the negative potential sweep, Ni starts depositing well before Ni and Fe co-deposition commence. Consequently, at the negative end of the sweep (−1.5V), the electrodeposited alloy layer has a composition strongly thickness dependent with an almost pure Ni layer in contact with the Au substrate ending up with a mixed FeNi layer on top of it. Therefore, the quantitative analysis of the electrochemical dissolution peaks of such complex alloy layer necessitates for example multi-parameter atomic scale simulations, which are out of the scope of this work.

A more appropriate means to study FeNi deposition/dissolution processes is to perform deposition at a fixed potential and to study the dissolution peaks as a function of the deposition time, the deposition potential, and the relative Ni and Fe solution concentration. As we will see in the following, such experiments are, in some cases, easier to analyze quantitatively. Such sequences were used in the previous chapters, especially to estimate the deposition rate. A typical series of dissolution curves for different alloy thickness deposited at −1.5 V in a Fe/Ni:80/20 solution is presented in Figure 5.2. In each curve, two dissolution peaks may be identified. The more negative one is attributed to selective Fe dissolution and the more positive one to Ni dissolution. The assignment of these peaks is consistent with the less noble character of Fe and is furthermore confirmed by magnetic measurements (see section 5.4). In the present case, it is relatively easy to separate both peaks and to estimate the charge of Fe and Ni in the alloy. However, as the peaks extend over a ~ 0.5 V potential range, the baseline correction is particularly delicate and may add a non negligible error on the charge estimation. The main contribution to this baseline is most probably the oxygen reduction current.
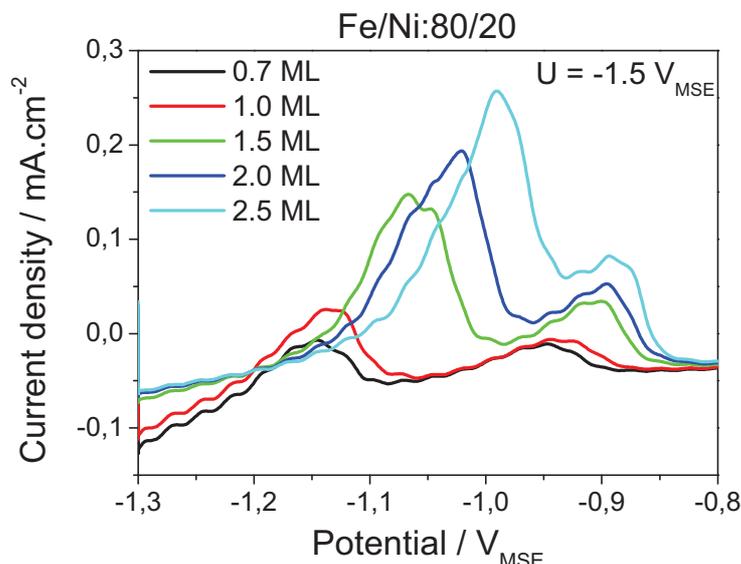
Figure 5.2 - : Positive potential sweeps into the Fe and Ni dissolution range after depositing at −1.5 V$_{MSE}$ 0.7, 1, 1.5, 2 and 2.5 ML of FeNi alloys in a solution containing 0.4 mM Fe^{2+} + 0.1 mM Ni^{2+}. Notice the shift of the onset potential of the dissolution of Fe (the more negative peak).

In order to overcome this difficulty and to fix accurately the more negative point of the two point baseline we used to fit the two peaks, we correlated the dissolution current with the reflectivity signal. The variation of the latter as a function of time upon Fe or Ni deposition is proportional to the deposit thickness, in the ultrathin layer limit. As Fe and Ni are both dissolved into a divalent state, the derivative of the reflectivity as a function of time should be closely correlated to the dissolution current. In Figure 5.3 we present such a correlation where the Y scales have been chosen to allow the more negative peak in the reflectivity derivative curve to match the correspondent one in the dissolution current curve. As we can see, the agreement between the two curves is good. The difference between the amplitudes of the more positive peak is due to the difference of the relative reflectivity between Fe and Ni. In our geometry (solution/deposit/Au(~8 nm)/Si(111)) and for the light wavelength we use in our MOKE setup (633 nm), the relative reflectivity of Ni is ~1.3 larger than that of Fe. Such value has been obtained using the complex refractive index of Fe (2.87 + i*3.36) and Ni (1.98 + i*3.74) found in references [15] and by calculating the reflectivity of the multilayer system. The calculated

difference of 1.3 accounts for the major part of observed difference between the reflectivity and the dissolution current.
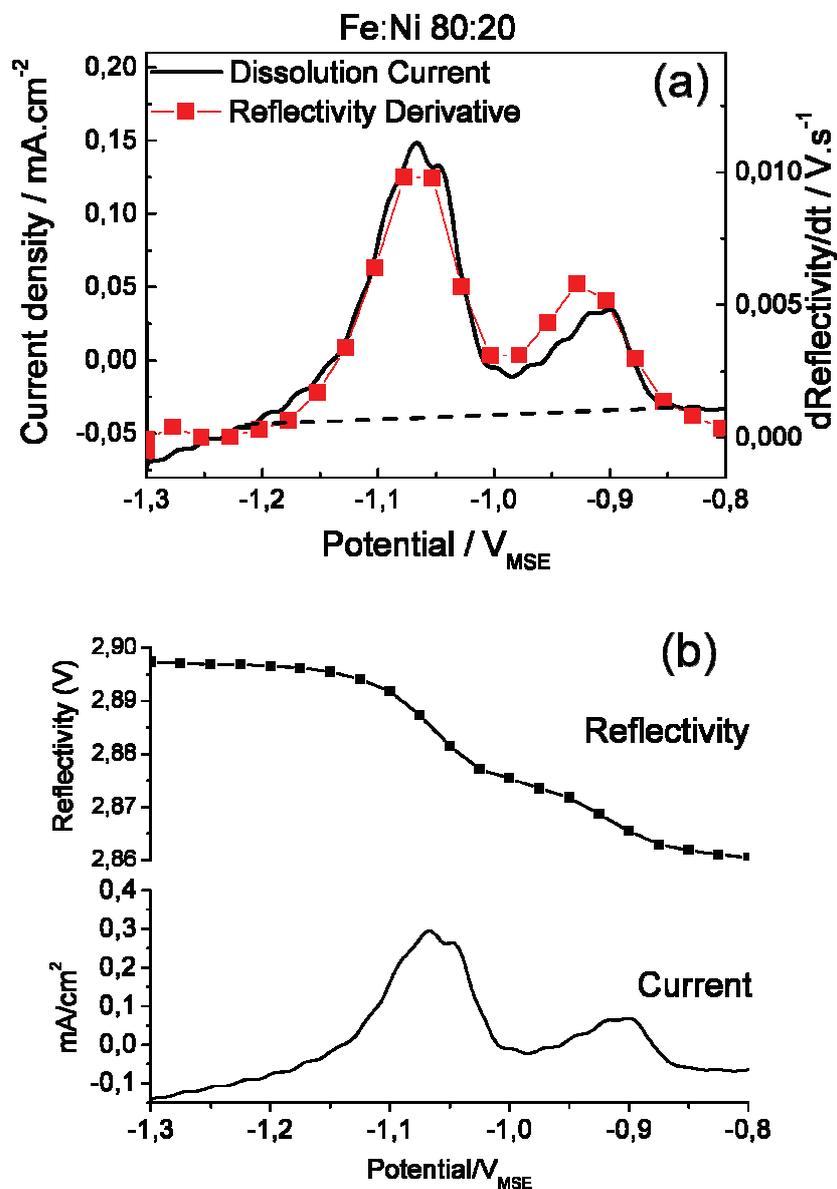
Figure 5.3 – (a) The electrochemical dissolution curve (black line) of a 1.5ML of FeNi alloy film deposited at $-1.5V_{MSE}$, in a solution containing 0.4 mM Fe^{2+} + 0.1 mM Ni^{2+}, together with the derivative as function of time of the film reflectivity (red symbols and line). Notice the good agreement between the two data sets. (b) The respectively reflectometry and curves density as acquired to the MOKE experiments.

The correlation between the reflectivity and the dissolution current allows one to determine the more negative point of the two point baseline as the point where the reflectivity

derivative takes off. The actual baseline of the present curve is represented as a dashed line in Figure 5.3. In spite of such correction, determining the Ni and the Fe contents from the dissolution current may still be tricky.

- First, it is difficult to determine the exact shape of the Fe and Ni peaks, especially in the region where they overlap. Moreover, the overlap between the two peaks becomes strong for layers thicker than 3 ML. We found that a Gaussian function fits more accurately a Lorentzian one. For the sake of simplicity, we didn't use more complicated functions and we fitted dissolution curves in the case of layers thinner than 2 ML.

- The second difficulty is that for solutions where the Fe relative concentration is lower than 50%, separated dissolution peaks could not be observed, as shown in Figure 5.4 in the case of Fe/Ni:20/80. Instead, we could measure the composition of a couple of these samples with a Au capping layer during the measurement campaign at Soleil Synchrotron. For this purpose we derived the alloy composition from the relative intensities of the X-ray fluorescence Kα-peaks, considering that the fluorescence yield of Fe and Ni is similar (their atomic numbers are very close). However, as we will see in the following, the alloys obtained in Ni rich solutions do not present a particularly interesting magnetic behavior. Therefore, they will not be studied thoroughly.

- The third difficulty is that we cannot rule out the possible Fe dissolution in the potential range of the more positive peak. Indeed, a well known phenomenon taking place during the dissolution of the less noble species of a bulk alloy forming a solid solution is the passivation of the alloy surface by the more noble metal [16]. Once the surface is passivated, further dissolution may only be obtained for significantly more positive electrode potentials, possibly in the potential range of the more noble metal dissolution. Such phenomenon is usually observed in the case of bulk alloys. However, it may also take place for ultrathin layer alloys. As we will show in the following sections, the correlation of the magnetic properties with the dissolution current gives evidence for such concomitant Fe and Ni dissolution for alloy layers thicker than 2 ML.
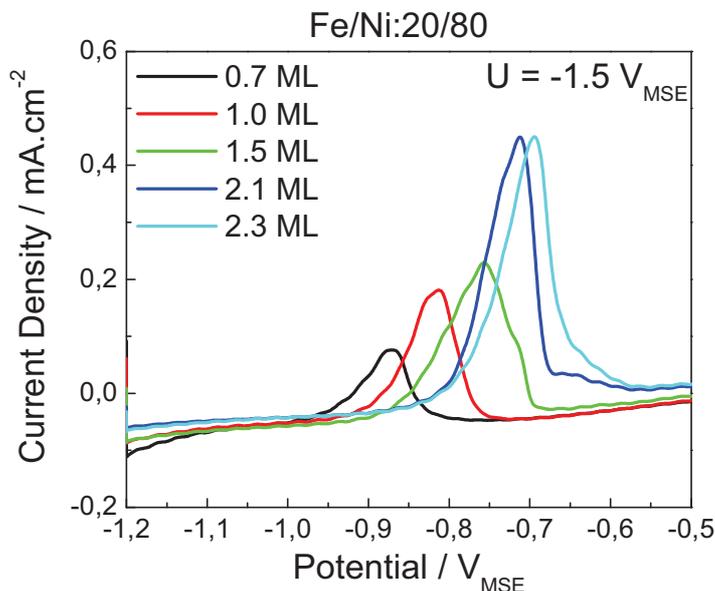
Figure 5.4 - Positive potential sweeps into the Fe and Ni dissolution range after depositing at −1.5 V$_{MSE}$ 0.7, 1, 1.5, 2.1 and 2.3 ML of FeNi alloys in a solution containing 0.1 mM Fe^{2+} + 0.4 mM Ni^{2+}. Notice the shift of the onset potential of the dissolution of Fe (the more negative peak).

Considering the limitation detailed above, we estimated the alloy composition for Fe-rich alloy and layers thinner than 2 ML only. Figure 5.5 shows the alloy composition as a function of the alloy thickness for different solution concentrations Fe/Ni:80/20, 70/30, 65/35, 60/40, and 50/50. The two horizontal lines in each graph indicate the composition of the solution. Closed (respectively open) symbols correspond to Fe (respectively Ni) content. Some common features may be derived from these plots:

- The alloy composition is strongly dependent on the alloy thickness except for the Fe/Ni:50/50 where the variations are within the estimation error.
- The alloy composition is close to Fe$_{50}$Ni$_{50}$ at low layer thickness and increases to approximately that of the solution at ~ 2ML. Although this is a main trend, the actual composition dependence on the thickness is more complex. For example, in the case of Fe/Ni:80/20, the composition for the thinnest layer we could measure is Fe$_{58}$Ni$_{42}$. In the case of Fe/Ni:70/30 and 65/35, the Fe content in the alloy is larger than the Ni one for the thinnest layers. This behavior is reversed in the case of Fe/Ni:60/40 and 50/50. However, one should be aware of the larger uncertainties on these points due to the small measured

111

electric charge and to the broadening of the dissolution peaks for the thinnest layers (see black and red curves in Figure 5.2) increasing the error due to the baseline correction.

- The Fe content in the alloy, in the thickness range 0−2ML, is smaller than the Fe relative concentration in the solution. Although we expect from the large negative deposition potential that the deposition flux is mainly limited by the diffusion of Fe^{2+} and Ni^{2+} species towards the sample surface, which rates should reflect the solution composition, such deviations from the solution composition for the first two alloy monolayers is not surprising. Indeed, the settling of the diffusion limited conditions necessitates a characteristic time equivalent to that needed for the depletion of ~100 µm solution layer (which corresponds to the diffusion layer induced by natural convection at room temperature) [17]. Such a solution volume with a total metallic concentration of 0.5 mM contains ~3 10^{15} metallic ions per cm^2, which yield a deposit thickness of ~1.7 ML (considering that the atom density of a relaxed Fe and Ni layers equals 1.8 10^{15} atoms.cm^{-2}).
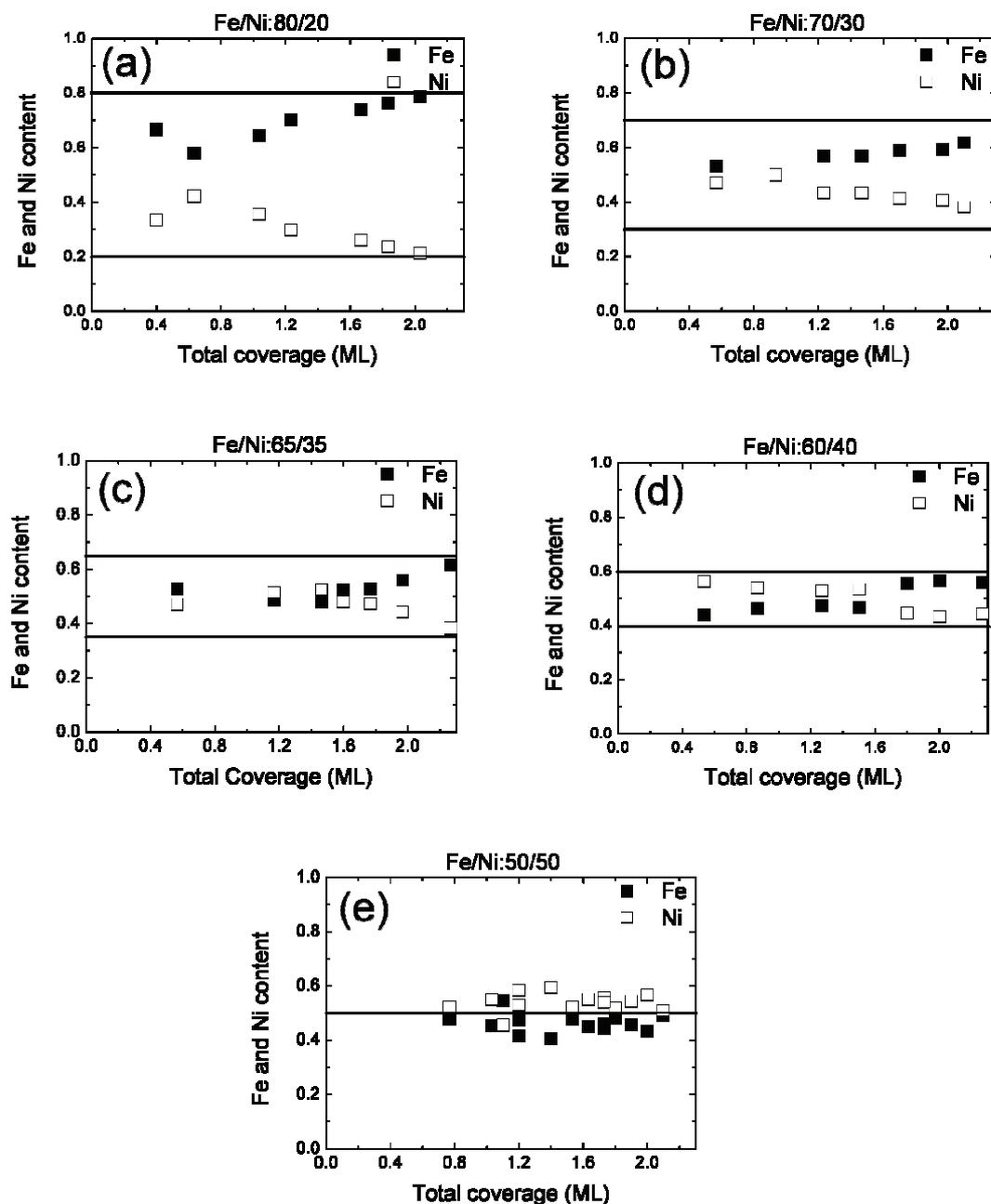
Figure 5.5 - FeNi alloy composition determined from the electrochemical dissolution curves of films in the 0−2ML thickness range deposited at −1.5V$_{MSE}$ in the following solution: (a) 0.4 mM Fe^{2+} + 0.1 mM Ni^{2+}, (b) 0.35 mM Fe^{2+} + 0.15 mM Ni^{2+}, (c) 0.325 mM Fe^{2+} + 0.175 mM Ni^{2+}, (d) 0.3 mM Fe^{2+} + 0.2 mM Ni^{2+}, (e) 0.25 mM Fe^{2+} + 0.25 mM Ni^{2+}. Notice the thickness dependence of the alloy composition.

The significant dependence of the alloy composition on its thickness suggests a peculiar variation of the deposition rate of Fe and Ni. For example, in the case of Fe/Ni:70/30, the first

monolayer composition is 50/50 whereas that of the second monolayer is 60/40. Such an increase of the Fe content necessitates an increase in the Fe deposition rate with respect to that of Ni. In order to get a deeper insight into this process, we show in Figure 5.6 the deposition rate of Fe and Ni as a function of the alloy thickness. Here again, some general trends may be observed:

- The deposition rate of Fe and Ni is approximately identical for alloy thickness of ~0.5 ML (or equivalently, at short deposition time, lower than 5−10s) and equals ~0.1 ML/s for all solution compositions. This behavior might appear intriguing. However, as shown in the previous chapters, the deposition rate of Fe and Ni is specifically high for the first monolayer, most probably due to the specific interaction between these two metals and the Au(111) substrate.

- Except for Fe/Ni:50/50, the deposition rate of Fe is significantly larger than that of Ni for alloy thickness larger than ~1.25 ML (or equivalently, at intermediate deposition time 10s < t < 30s). Moreover, the Ni deposition rate decreases to almost zero at ~1.75 ML. This difference in the deposition rates of Fe and Ni allows the alloy composition to get close to that of the solution at 2 ML. Its origin is not clear. Part of it should be related to the relatively lower concentration of Ni in the solution. However, the Ni deposition rate is not strictly proportional to the Ni concentration of the solution. This indicates that other complicated processes are involved in the slowing down of the Ni deposition above ~1.25ML. For example, we know from the previous chapters that the deposition rates of Ni on Ni and Fe on Fe is smaller than those of Ni on Au and Fe on Au. In the case of the FeNi alloy deposition, if we assume a layer-by-layer growth, the second layer grows on a mixed Fe and Ni substrate. The deposition rate will thus depend in a complex way on the composition of the first alloy monolayer.
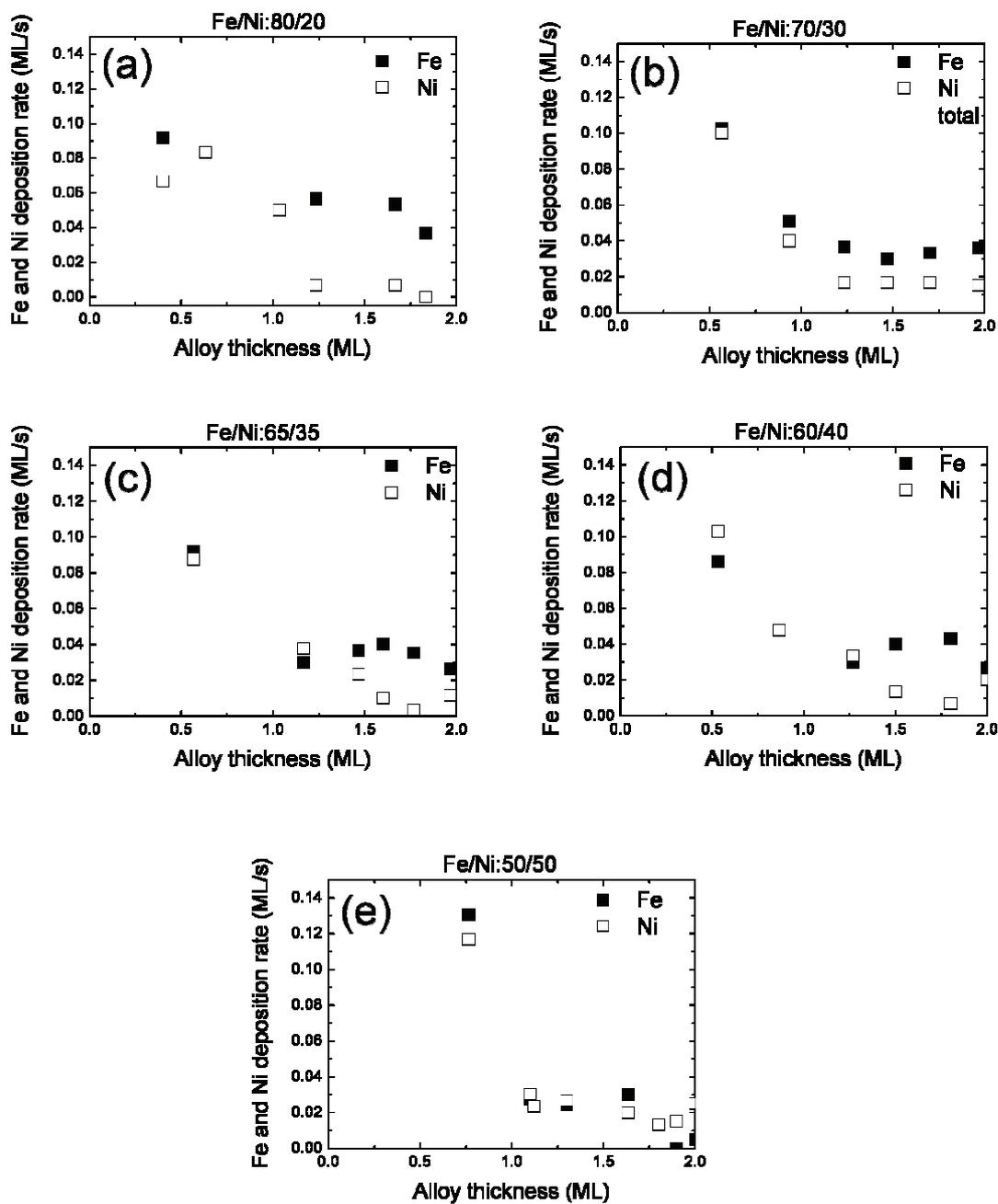
Figure 5.6 - Fe and Ni deposition rates determined from the electrochemical dissolution curves of films in the 0−2ML thickness range deposited at −1.5V$_{MSE}$ in the following solution: (a) 0.4 mM Fe^{2+} + 0.1 mM Ni^{2+}, (b) 0.35 mM Fe^{2+} + 0.15 mM Ni^{2+}, (c) 0.325 mM Fe^{2+} + 0.175 mM Ni^{2+}, (d) 0.3 mM Fe^{2+} + 0.2 mM Ni^{2+}, (e) 0.25 mM Fe^{2+} + 0.25 mM Ni^{2+}. Notice the thickness dependence of the Fe and Ni deposition rates.

It is interesting to study the dependence of the deposition potential on the alloy composition. At potentials more negative than −1.5V, we do not expect a significant difference as compared to −1.5V, because for pure Fe and pure Ni, the deposition rate is no longer potential dependent below −1.5V (see previous chapters). On the other hand, we expect significant changes when the deposition potential is more positive than −1.5V, because the Fe deposition rate should in principle decrease drastically. We will first examine the influence of the deposition potential on the dissolution curves. In Figure 5.7, we show the dissolution curves for a 3.1ML thick FeNi film deposited in a solution Fe/Ni:80/20 at −1.5V (dashed line) and at −1.35V (solid line). As explained above, the Fe and Ni dissolution peaks are no longer separated whenever the total thickness is larger than ~2ML. We indeed observe a rather broad misshapen peak extending from −1.05V to −0.85V. On the opposite, in the case of −1.35V, we clearly observed two well defined dissolution peaks. This presence of two dissolution peaks strongly suggest that Fe is deposited at this rather positive potential and its deposition rate is significant, although, in the absence of Ni in the solution, the Fe deposition rate is at least one order of magnitude smaller. This behavior is called anomalous deposition and is relatively well known in the case of FeNi [13,18]. The well-defined Fe and Ni peaks allow us to determine the alloy composition up to an alloy thickness of at least ~4ML. A further proof of the assignment of the more negative dissolution peak to Fe will be also given in section below dealing with the FeNi magnetic properties. The difference between the dissolution curves for alloy films deposited at −1.5V and −1.35V also suggests that the alloy microstructure might be different.
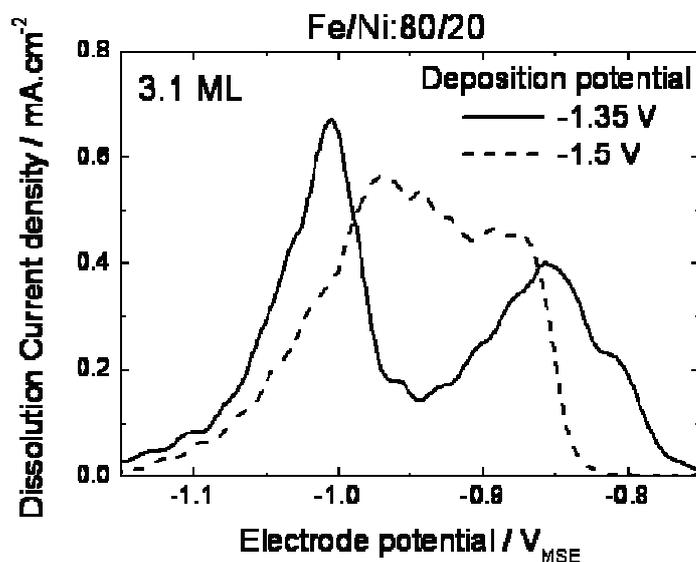
Figure 5.7 - Positive potential sweeps into the Fe and Ni dissolution range after depositing at −1.5 V_{MSE} (dashed curve) and at −1.35V_{MSE} (solid curve) 3.1ML of FeNi alloys in a solution containing 0.4 mM Fe^{2+} + 0.1 mM Ni^{2+}. Notice the difference in the dissolution peak separation.

The alloy composition and the Fe and Ni deposition rates as a function of the alloy thickness are shown in Figure 5.8 a−b. Similarly to deposits at −1.5V, the composition of the FeNi alloy deposited at −1.35V is close to 50/50 below 1ML. In the thickness range between 1ML and 3 ML, the alloy is intriguingly Fe rich. Above 3ML, the alloy recovers the initial 50/50 composition. Again, such a thickness dependent composition is accompanied by a complex dependence of the Fe and Ni deposition rates on the alloy thickness, with a significantly larger Fe rate in the thickness range between 1ML and 2ML. In the rest of this chapter, we will not focus on the possible mechanisms of this specific thickness dependent deposition rate at −1.35V. The understanding of the processes involved in the anomalous deposition calls for atomic scale simulations which are out of the scope of this work.
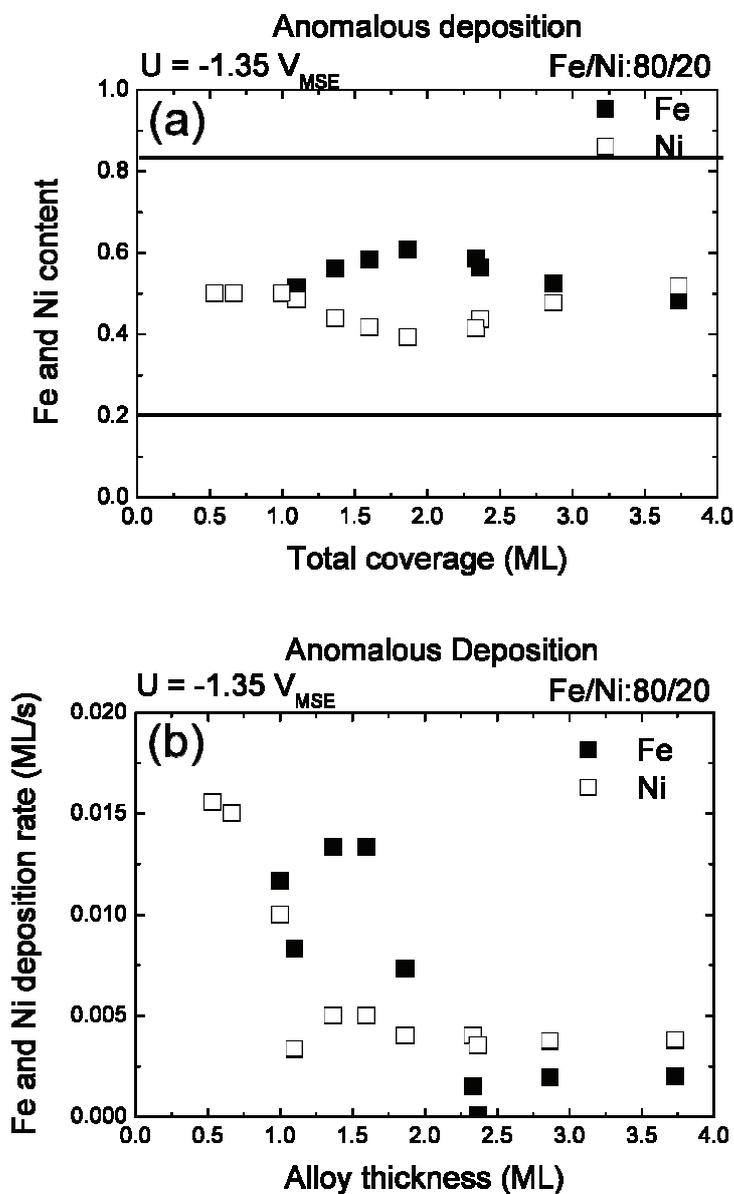
Figure 5.8 - (a) FeNi alloy composition determined from the electrochemical dissolution curves of films in the 0−4ML thickness range deposited in the anomalous regime at −1.35V_{MSE} in the following solution 0.4 mM Fe^{2+} + 0.1 mM Ni^{2+}. (b) Fe and Ni deposition rates determined from the electrochemical dissolution curves of films in the 0−4ML thickness range deposited in the anomalous regime at −1.35V_{MSE} in the same solution.

5.2.2. Determining the alloy composition and thickness: the case of films thicker than 2 ML

As we showed in the previous section, determining the alloy composition from the electrochemical dissolution curve is limited to the film thinner than 2ML. On the other hand, the structural characterization that we will detail in the next section have been performed on films 3−6 ML thick. Moreover, in this case, the deposition electrochemical cell configuration was slightly different (see next section) and the films were capped by an Au layer, which thickness (typically ~2nm) could not be determined accurately. This latter manipulation adds some uncertainties on the alloy thickness estimation. However, in order to properly correlate the alloy magnetic properties with its structural characterizations, it is necessary to be able to estimate the alloy composition and thickness accurately. For this purpose, we used complementary techniques like the X-ray fluorescence, which we obtained by X-ray excitation (at Soleil synchrotron and using the laboratory X-ray spectrometer) or by electron excitation using a scanning electron microscope (SEM). At Soleil synchrotron, we measured the fluorescence intensity at the Fe and Ni K-edges. On the other hand, our laboratory X-ray spectrometer allowed us to measure the sample fluorescence at the Fe K-edge only. In order to obtain the Fe and Ni content in the alloy film, we compared the measured fluorescence intensities with that of a reference Ni and Fe samples with a known thickness. This data analysis didn't necessitate any further correction (except for the background signal).

The X-ray fluorescence obtained in a SEM was measured for Fe and Ni at K and L edges. The electron excitation energy for the K edge measurements was 15 keV, whereas it was 3 keV for the L edge. These values were chosen in order to optimize the signal to noise ratio of the Fe and Ni peaks and to reduce the background signal especially in the case of the L edge peaks. Typical spectra are shown in Figure 5.9. We observed that in these excitation conditions, the L and K peak intensities are approximately in the same range, although the L fluorescence yield is expected to be typically two orders of magnitude smaller than that of the K fluorescence. This unexpected larger fluorescence intensity (especially in the case of Ni) probably originates from the formation of a large density of medium energy electrons in the samples (due to the Au capping layer) thus increasing the absorption yield. This yield enhancement is larger for Ni which results in a larger signal to noise ratio for the Ni L edge peak as compared to the Ni K

edge one. Consequently, although the composition estimation obtained from the L peak is approximately similar to that determined from K peak, that obtained from the L peaks is more accurate. In order to get the atomic percentage, the fluorescence intensities are converted by the X-ray detector software (Noran Six, from Thermo), which takes into account the different experimental conditions.
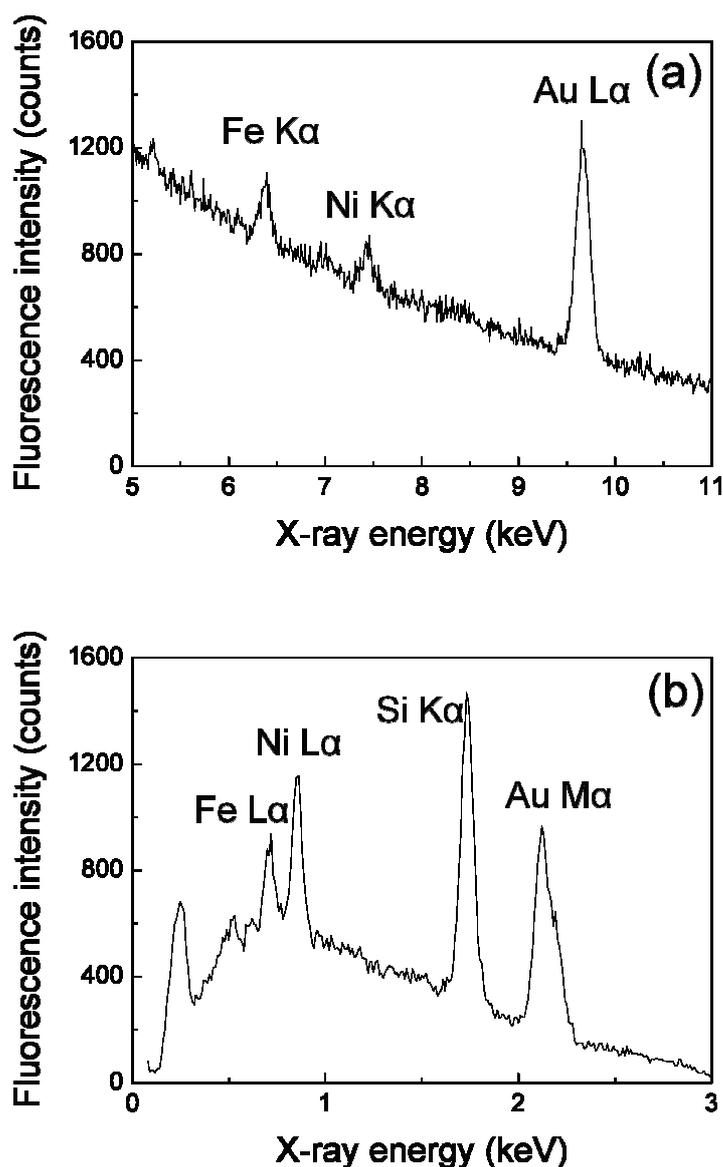

Figure 5.9 - EDX spectra (acquired in a scanning electron microscope) as a function of the X−ray energy using an incident electron beam energy of (a) 15keV and (b) 3keV of ~5ML alloy film deposited at −1.5 V_{MSE} in 0.25 mM Fe^{2+} + 0.25 mM Ni^{2+}. We can clearly distinguish the Kα (a) and Lα (b) lines of Fe and Ni.

In order to cross check the different information obtained from the different composition analysis methods, we show in Figure 5.10 the Fe and Ni atomic percentages (black columns) and thicknesses in ML (red columns) for different samples having distinct compositions and thicknesses. Two different Y-scales were used because it is difficult to normalize the fluorescence measurements with the SEM with respect to a reference sample. We clearly observe in Figure 5.10 the good agreement between the results of the two types of measurements. We are therefore confident with these estimations of the alloy composition and thickness.
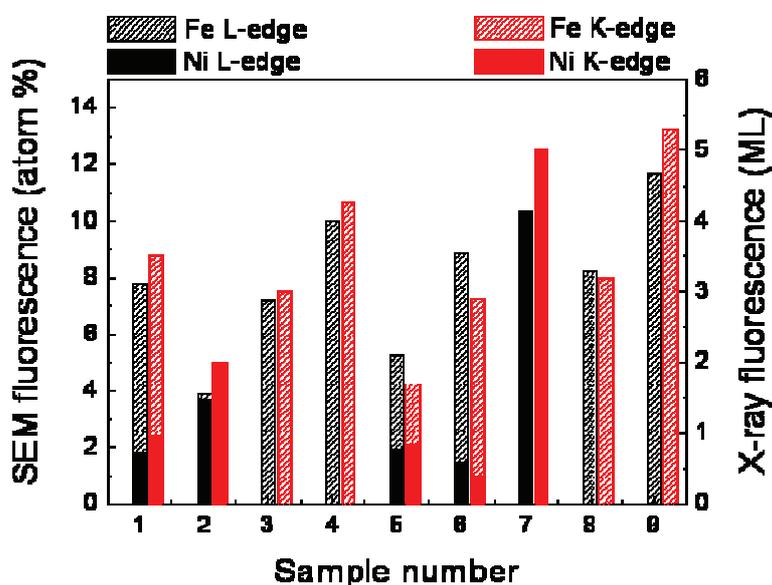
Figure 5.10 - Comparison between the Fe and Ni Lα line intensities (black columns) acquired in the SEM (3keV electron beam) and Fe and Ni Kα fluorescence intensities (red columns) from EXAFS and X-ray experiments, for different FeNi alloy films (3−5ML thickness range). For some sample, the Ni fluorescence was not measured. Notice the good agreement between the results of the two techniques.

From these measurements, we can determine the precise thickness and alloy composition of the capped films specially prepared for ex-situ measurements. Indeed, the characteristics of these films may differ from those prepared in-situ because of the above mentioned different cell configuration and the additional Au capping step. In Table 1 we show the thus determined film thickness and composition for each sample. Although the difference between the expected

thickness and the real one for the 5 ML films is relatively small, it is significantly larger for the 2 ML film, which real thickness is ~3ML. The alloy composition is also different from that of the deposition solution but the difference remains below 20%.

Table 1 - the real sample thickness and composition deposited at −1.5 V_{MSE} in different solution compositions as determined from the fluorescence measurements.

Sample	Real thickness	Real composition
2ML Fe	3.2 ML	
2ML Fe/Ni:50/50	3.4 ML	$Fe_{41}Ni_{59}$
2ML Fe/Ni:80/20	3.3 ML	$Fe_{88}Ni_{12}$
2ML Fe/Ni:80/20 anomalous	2.5 ML	$Fe_{67}Ni_{33}$
5ML Fe	5.3 ML	
5ML Fe/Ni:50/50	5.2 ML	$Fe_{56}Ni_{44}$
5ML Fe/Ni:80/20	5.6 ML	$Fe_{75}Ni_{25}$

In the following, we will use the alloy thickness and composition determined from these analyses (Table 1).

5.3. Structural characterizations

As explained in the introduction section, our aim is to understand the magnetic properties (which will be presented in the next section) of the FeNi ultrathin alloy films. Among the parameters that may influence the magnetic behavior, the atomic volume seems to play an important role in defining the magnetic moment per atom [19]. Moreover, the influence of the film crystallographic structure and orientation, and the presence of strain may be large enough to change the sign of the film magnetic anisotropy. This results in a change in the orientation of the film magnetization (in the case of Ni films see [20]). In this section we will focus on the structure and the strain of the FeNi alloy films deposited on Au(111). We will use X-ray diffraction (XRD) as well as extended X-ray absorption fine structure (EXAFS) to gain insight into the crystallographic phase and orientation as well as to estimate the film strain. This approach is similar to the one used to study Fe films deposited on Au(111) in the chapter 3. We will also present the typical morphology of the alloy films from STM experiments. The purpose is to determine the film flatness.

XRD and EXAFS experiments were performed ex-situ with the sample capped by a ~2nm thick Au layer (to avoid FeNi film oxidation). The capping layer was deposited immediately after the FeNi film deposition by rapidly exchanging, under potential control, the FeNi deposition solution by a solution containing $AuCl_4^-$ ions. The capping of the FeNi layer may alter the structure of the alloy film. Therefore, one should be careful when comparing data of capped alloy films with those obtained in-situ, i.e., with the alloy film in contact with the solution. The available synchrotron beamline time allowed us to study two different thicknesses (typically ~3ML and ~5ML) and three different solution compositions Fe/Ni:80/20, 50/50 and anomalous deposit.

XRD spectra were acquired at 7 keV. EXAFS spectra were acquired at the Fe (7.13 keV) and Ni (8.34 keV) edges when possible. A typical EXAFS spectrum at one edge was taken with a resolution of 2.7 eV. For the 3ML thick samples, it was often necessary to average several spectra in order to obtain a reasonable signal to noise ratio. EXAFS spectra were analyzed in two steps: (i) overall analysis of the general aspect of the spectra allowing to determine the dominant crystallographic phase, i.e., to differentiate bcc from fcc phase; (ii) simulation of the EXAFS spectra with FEFF software [21] to determine the atomic scale arrangement as well as the in plane

strain of the layer. The second step allows in principle to quantitatively estimate the structure, the strain and the composition of the alloy. For the sake of simplicity, the FEFF calculations were performed considering that the alloy layer has no interaction with the substrate and the capping layer, as if it is free standing in vacuum. This corresponds to neglecting the spatial coherence between the alloy layer and the substrate and the capping layer, which may be a crude approximation. Indeed, as we will show in the following, the alloy layer is in epitaxy with the substrate. Not taking into account the substrate in our FEFF calculations will in principle affect the EXAFS spectrum, and it will affect more strongly the thinnest alloy layers.

In the following, we will start by presenting briefly the STM results and then XRD data followed by the EXAFS data.

5.3.1. *Scanning Tunneling Microscopy*

STM experiments were carried on to determine the flatness of the alloy deposits. More thorough STM studies allowing to investigate the initial nucleation and growth of the alloy as well as the arrangement of Fe and Ni in the alloy layer would have been of interest, but are out of the scope of this work.

As shown in the previous chapters, pure Fe and Ni deposits on Au(111) are essentially atomically flat up to a few ML thick. Consequently, we expect that the alloy deposit to be also flat. STM experiments were performed in-situ and the alloys were deposited in the STM cell. The deposition conditions were similar to those in the MOKE cell, although no solution circulation was possible. Therefore, the alloy composition may differ from that of the deposit in the MOKE cell. As we are interested by the deposit flatness only, no special effort has been made to determine precisely the alloy composition when deposition occurred in the STM cell.

In Figure 5.11 we present two typical STM images corresponding to FeNi alloy deposits in the solution Fe/Ni:50/50 (Figure 5.11a) and Fe/Ni:80/20 (Figure 5.11b). The film thickness is ~1ML (Figure 5.11a) and ~2ML (Figure 5.11b). In both cases, atomic steps are clearly visible and the deposit morphology is atomically flat and essentially layer-by-layer. This information is important for the analysis that will be done in the following sections.
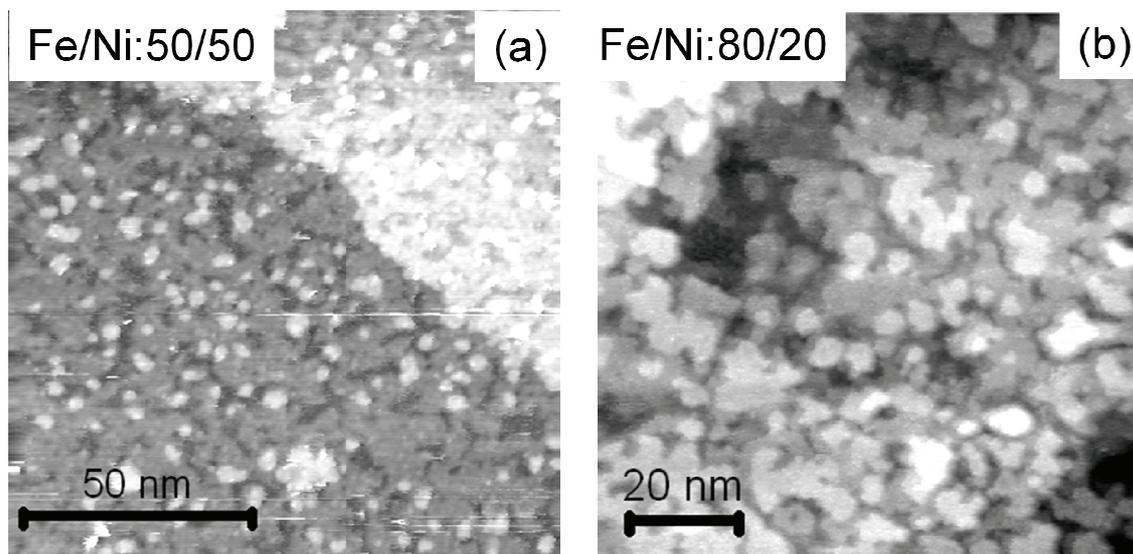
Figure 5.11 - *In−situ* **STM images of (a) ~1ML and (b) ~2ML FeNi alloy films deposited at −1.5V$_{MSE}$ in (a) 0.25 mM Fe^{2+} + 0.25 mM Ni^{2+}, and (b) 0.4 mM Fe^{2+} + 0.1 mM Ni^{2+}. The image size is typially 100x100 nm^2. Notice the flatness of the films on the atomic scale.**

5.3.2.   *X-ray diffraction*

Similarly to the case of pure Fe and pure Ni, we performed X−ray diffraction experiments in Bragg conditions allowing us to observe the possible presence of a fcc phase or a bcc phase. However, as we will see below, the diffraction peaks of the FeNi alloys are broader than those of the pure metals, which make the interpretation more delicate. A typical spectrum of a 5.6ML thick $Fe_{75}Ni_{25}$ alloy film is presented in Figure 5.12a (black symbols). It corresponds to the diffracted intensity as a function of the sample rotation around an axis perpendicular to the sample surface. The detector position corresponds to that allowing to detect the Fe bcc (10−1) peak. We also superimposed the spectrum of pure Fe 5.3ML thick (red symbols). In the latter case we clearly observed two distinct peaks which have approximately similar intensities and are centered roughly symmetrically with respect to Phi = 0°. These peaks have been assigned to Fe(10−1) bcc peaks (see chapter 3). In addition, the angle separating the two peaks is directly related to the in-plane layer tensile strain, which operates along the b-axis of the rectangular unit cell of the 10−1 plane. A peak separation of 10.5° corresponds to the absence of strain, whereas if it equals 0, the strain is 23%. Finally, as we will show in the following, we observed the presence of peak centered at Phi = 0°, even in the absence of a Fe layer. We attribute this peak to

a Au(10L) rod, although we didn't have enough beamline time to perform the necessary scans to confirm this assumption and to estimate the amplitude of this rod. Therefore, the diffraction spectra will be fitted with three peaks, two Gaussian lines corresponding to the bcc phase and one Lorentzian one corresponding to the Au(10L) rod.

In the case of the FeNi alloy, it is difficult to distinguish the two peaks corresponding to the presence of a bcc phase (black symbols). Instead, we observe a broad peak centered at Phi = 0°. However, as we will show in the next section (EXAFS results), this FeNi alloy film has a clear bcc signature. As explained above, a reasonable fit of the experimental data of Figure 5.12a (black symbols) may be obtained using two Gaussian lines and one Lorentzian line centered at Phi = 0°. In order to decrease the number of parameters, we considered that the two Gaussians have identical amplitudes and widths. The fitting of the experimental results is presented in Figure 5.12a (black lines), using a typical width of the Gaussian curves of ~5.5°.
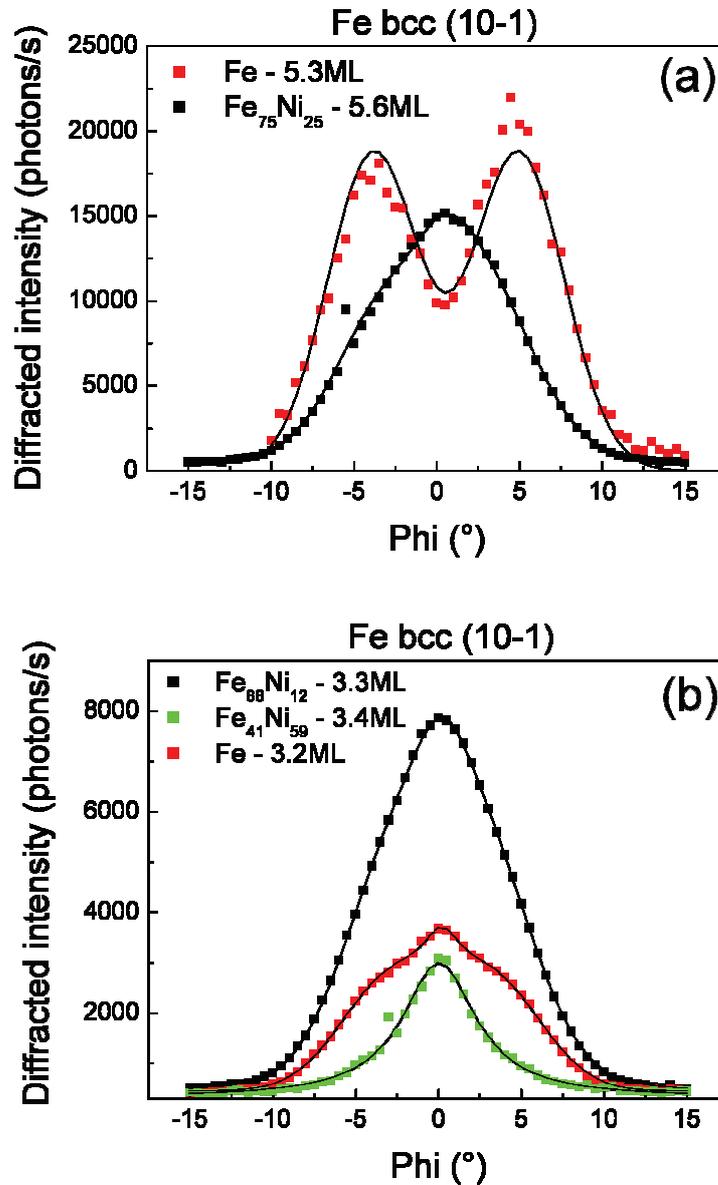
Figure 5.12 - X−ray diffraction spectra as a function of the sample rotation angle Phi in the bcc Fe(10−1) Bragg conditions of (a) ~5ML Fe (red symbols) and $Fe_{75}Ni_{25}$ (black symbols), and (b) ~3ML Fe (red symbols), $Fe_{88}Ni_{12}$ (black symbols) and $Fe_{41}Ni_{59}$ (green symbols) alloy films. The black lines correspond to the experimental data best fits using one Lorentzian line centered at Phi=0° and two symmetrically centered (with respect to Phi=0°) Gaussian lines with equal amplitudes and widths.

In the case of thinner FeNi alloy layers, we also observe similar diffraction pattern. In Figure 5.12b we show the diffraction peak of the 3.3 ML thick $Fe_{88}Ni_{12}$ (black symbols), together with that of the 3.4 ML thick $Fe_{41}Ni_{59}$ alloy (green symbols). We also superimposed the

127

spectrum of a pure Fe 3.2 ML thick (red symbols) for comparison. In the case of the 3.2 ML thick Fe layer, the two peaks explained above are also distinguishable although less prominent because of the presence of the Au rod central peak. The diffraction peak of the 3.3 ML thick $Fe_{88}Ni_{12}$ alloy layer is very similar to that of the 5.6ML thick $Fe_{75}Ni_{25}$ alloy (Figure 5.12a, black symbols). We used the same fitting procedure as for the ~5ML tick films and obtained a good agreement with a Gaussian curve with a typical width of 5.8°−6°. The origin of the much larger diffraction signal of the $Fe_{88}Ni_{12}$ layer (Figure 5.12b, black symbols) as compared to that of pure Fe layer (Figure 5.12b, red symbols) is not clear. It is not due to a change in the experimental conditions (different X−ray intensity or incident angle) and can not be explained by a different capping layer thickness.

The case of the 3.4 ML thick $Fe_{41}Ni_{59}$ alloy is clearly different. The shape of its diffraction peak is obviously distinct, with no clear features except an apparent single peak centered at Phi = 0°. It can be fitted with a single Lorentzian line with no significant fit improvement upon adding two Gaussian lines. Such observations suggest that in this case a significant part of the alloy layer is not bcc. As we will see in the following sections, this conclusion is fully consistent with the EXAFS results.

From these spectra, and more specifically from the angle separation between the two peaks of the bcc phase, we could determine the in-plane tensile strain of the film along the b-axis of the unit cell (similarly to that estimated in the previous chapters for pure Fe). These values are shown in Table 2, together with those of pure Fe layers. These strain values will be useful for comparison with the EXAFS simulations.

Table 2 - The XRD bcc (10−1) separation peaks and the corresponding in−plane strain of different alloy films, deposited at −1.5 V_{MSE}.

Sample	Peak separation (°)	In−plane strain (%)
3.2ML Fe	6.5	7.9
3.3ML Fe$_{88}$Ni$_{12}$	5.4	10
5.3ML Fe	8.5	3.9
5.6ML Fe$_{75}$Ni$_{25}$	6.9	7.9

It is also interesting to study the diffracted intensity in Bragg conditions corresponding to the fcc phase, especially for the 3.4 ML thick Fe$_{41}$Ni$_{59}$ alloy. Figure 5.13a presents the spectrum of the latter sample together with those pure Ni and Fe. As shown in the previous chapters, the pure Ni film is fcc and present six prominent peaks every 60° starting at the expected Phi = 2.8° (red curve). In contrast, the pure Fe spectrum is featureless (green curve). The Fe$_{41}$Ni$_{59}$ spectrum is similar to that of pure Ni, although its intensity is two times smaller. This result together with the absence of diffracted signal in the bcc Bragg conditions strongly suggests that the 3.4 ML thick Fe$_{41}$Ni$_{59}$ alloy is mainly fcc.
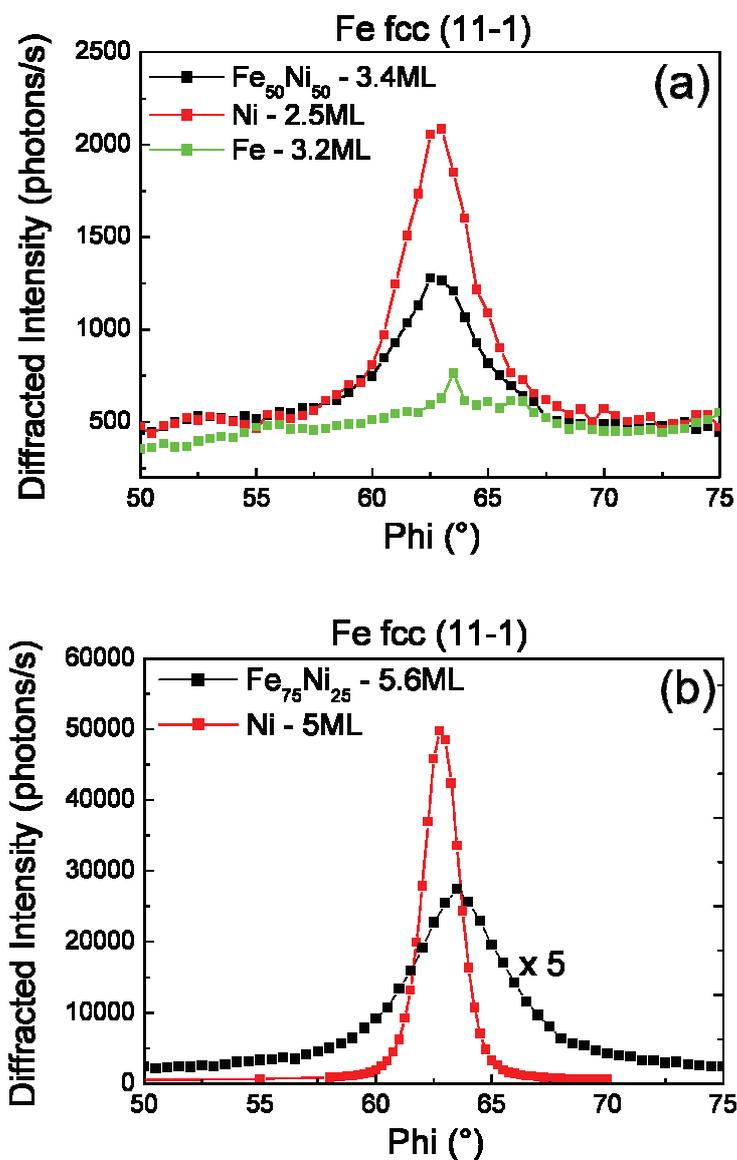
Figure 5.13 - X−ray diffraction spectra as a function of the sample rotation angle Phi in the fcc Fe(11−1) Bragg conditions of (a) ~3ML $Fe_{50}Ni_{50}$(black symbols), Ni (red symbols), and Fe (green symbols) and (b) ~5ML Ni (red symbols), and $Fe_{75}Ni_{25}$ (black symbols) alloy films.

The case of the 5.6ML thick $Fe_{75}Ni_{25}$ alloy is less straightforward. Its spectrum together with that of pure Ni 5ML thick are shown in Figure 5.13. We find the characteristic peaks of Ni fcc centered at Phi = 62.8° with a six fold symmetry (red curve). The diffraction pattern of the $Fe_{75}Ni_{25}$ alloy (black curve) also presents a peak 5 times less intense than that of pure Ni and

slightly shifted towards larger Phi values (63.5°). Therefore, although this sample presents a significant diffraction signal in the bcc Bragg conditions, we cannot exclude the presence of a fcc phase.

5.3.3.   EXAFS

The characteristic form of the EXAFS spectra of Ni and Fe films ~5 ML thick are shown in Figure 5.14. As we showed in the previous chapters, the structure of Fe-5.3ML films is mainly bcc whereas that of Ni-5ML films is fcc. The difference in the structural phase, i.e., in the crystal symmetry, induces differences in the EXAFS spectra. In Figure 5.14, we clearly observe differences in the oscillation amplitude and phase. In addition, a minimum (indicated by an arrow) which is observed in the Fe spectrum at k = 4.8 Å^{-1} is clearly absent in the Ni spectrum. The characteristic shape of the spectra and in particular the dip at k = 4.8 Å^{-1} will allow us in the following to distinguish between the bcc and fcc phases.
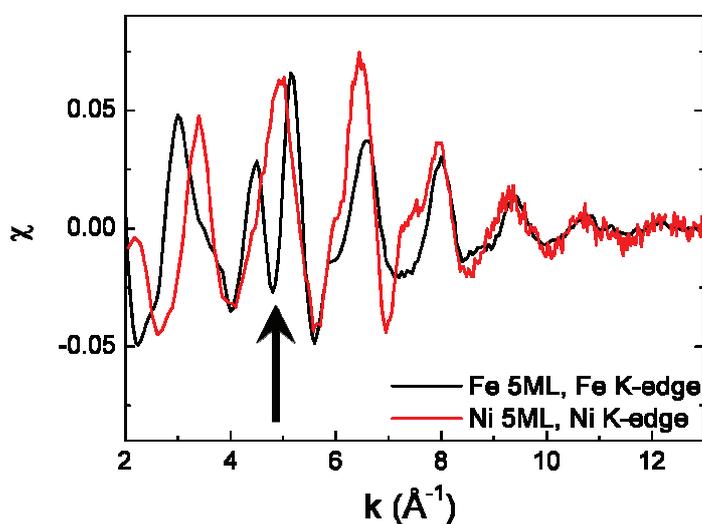
Figure 5.14 - : EXAFS χ-k spectra at the Fe edge (black line) and Ni edge (red line) of ~5ML pure Fe and Ni films. Notice the presence of a dip (indicated by an arrow) in the Fe spectrum which is absent in the Ni one.

EXAFS spectra for 5.6ML thick Fe$_{75}$Ni$_{25}$ (respectively 3.3 ML thick Fe$_{88}$Ni$_{12}$) alloy films are shown in Figure 5.15a (respectively Figure 5.15b). They are superimposed to spectra of pure Fe for comparison. It is straightforward from Figure 5.15a that the phase of the 5.6ML thick FeNi alloy is close to that of pure Fe, i.e. bcc, although the minimum at k = 4.8 Å^{-1} is less pronounced than in the case of pure Fe. Quantitative FEFF simulations are necessary to get deeper insight into these deviations and they are due to an atomic disorder or to the presence of significant amount of an fcc phase. Similar conclusions may be drawn for the 3.3 ML thick alloy (Figure 5.15b). In addition to the EXAFS spectrum obtained at the Fe edge, we superimposed that obtained at the Ni edge (red curve). The almost perfect agreement between these two spectra demonstrates that the alloy forms a single phase, namely, bcc. This result suggests that the FeNi alloy films form a solid solution, because, if the alloy is phase separated, the Ni phase is expected to be fcc. The difference between the two spectra originates probably from the difference between the backscattering amplitude and phase of Fe and Ni.
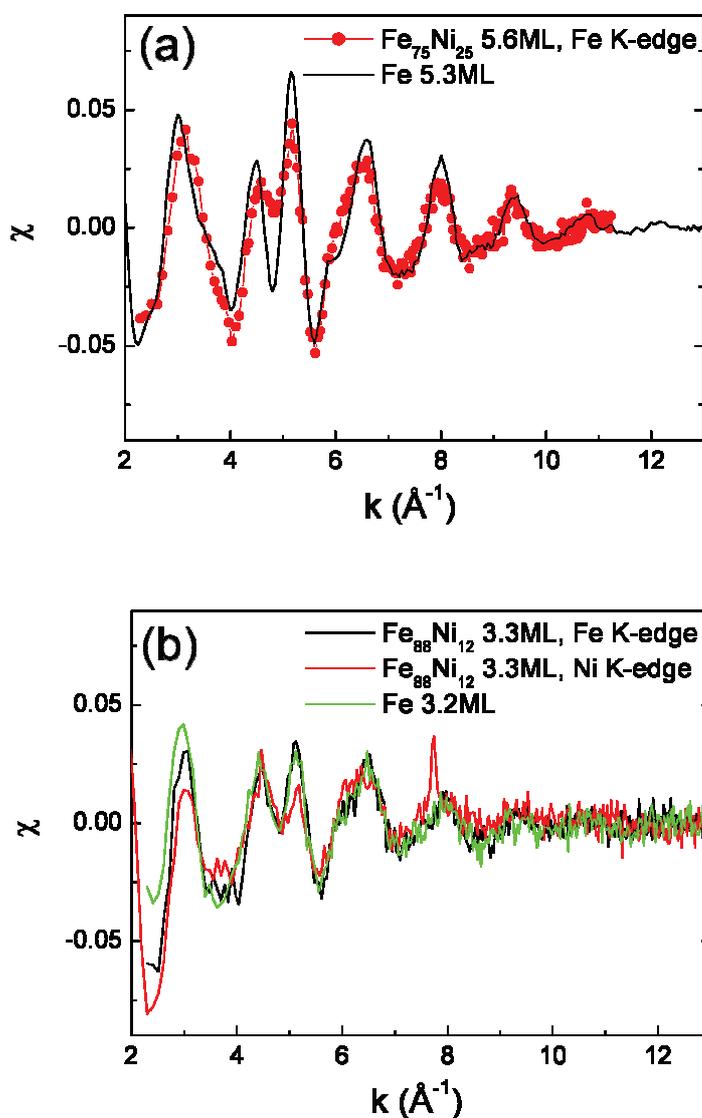
Figure 5.15 - (a) EXAFS χ-k spectra at the Fe edge of ~5ML thick Fe (black line) and Fe$_{75}$Ni$_{25}$ (red symbols and line) films. (b) EXAFS χ-k spectra of ~3ML thick Fe (Fe edge, green line), and Fe$_{88}$Ni$_{12}$ (Fe edge, black line and Ni edge red line) films. Notice the good agreement between the spectra of each graph.

The typical shape of the EXAFS spectra of the 3.4 ML thick Fe$_{41}$Ni$_{59}$ alloy is shown in Figure 5.16. The spectrum at the Fe edge (black curve) and that of the Ni edge (red curve) are almost identical and essentially similar to that of pure Ni layer (green curve). In the same way as we proceeded above, we can conclude that the alloy forms mainly a fcc solid solution.
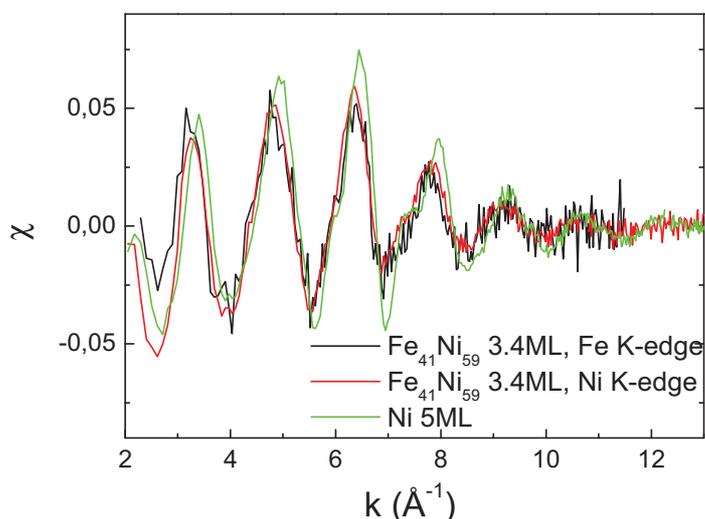
Figure 5.16 - EXAFS χ-k spectra of ~5ML thick Ni (Ni edge, green line), and ~3ML thick Fe$_{41}$Ni$_{59}$ (Fe edge, black line and Ni edge red line) films. Notice the good agreement between the spectra of each graph.

In order to get a better insight into the EXAFS data, we performed FEFF calculations [21] for the different alloy films. We varied the in-plane film strain, the amount of fcc and bcc phase as well as the alloy composition. Before presenting the best fits of our experimental results, we would like to show the effect of each parameter on the calculated EXAFS spectrum to determine to which extent each parameter will affect the EXAFS spectrum.

We already showed previously in this section that the bcc and the fcc phases have clearly distinct EXAFS signatures (see for example Figure 5.14). Now let us see what happens if we keep the crystallographic structure constant and we switch from the pure metal to the alloy. In Figure 5.17 we compare the spectra of a bcc phase (Figure 5.17a) and of a fcc phase (Figure 5.17b) for different Ni content of the alloy. Replacing Fe atoms by Ni atoms (up to 50%) does not seem to change significantly the EXAFS bcc spectrum (Figure 5.17a). The small changes for low k values are within the experimental noise level of our data. In the case of a fcc phase, the changes are slightly larger and become larger than our experimental noise for Ni content larger than 50%. These relatively small differences originate from the close atomic number of Fe and

Ni. Consequently, it will be difficult to determine precisely the alloy composition using the EXAFS data.
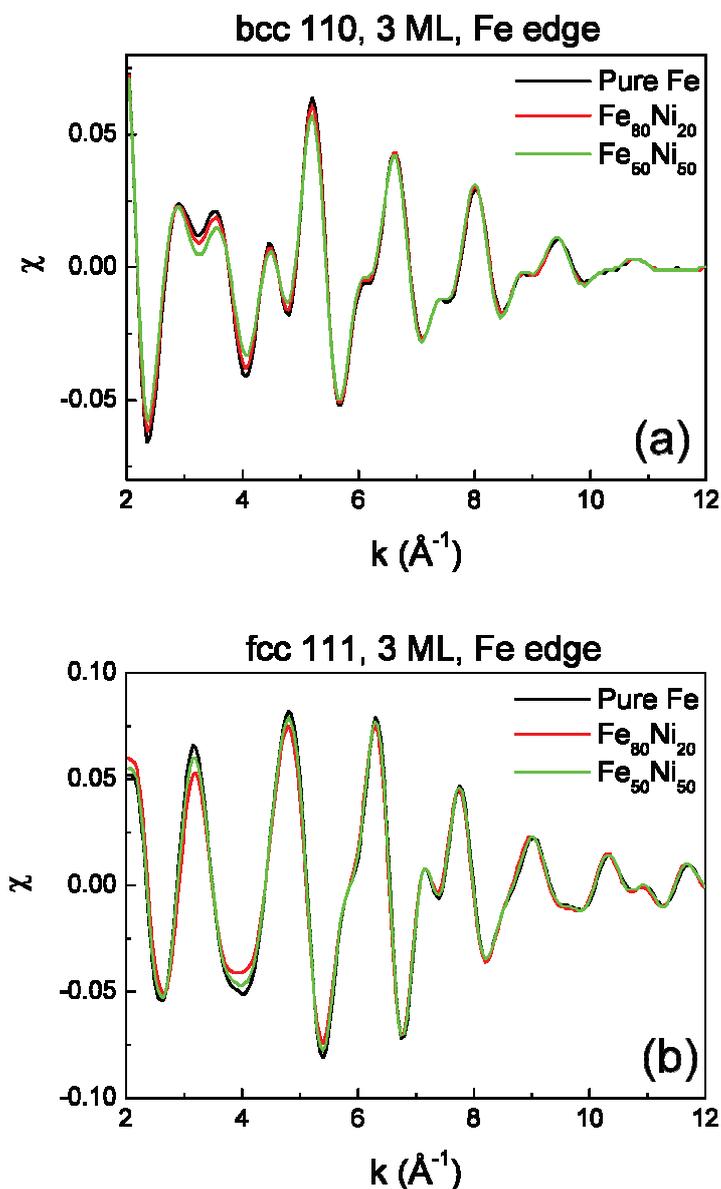
Figure 5.17 - (a) calculated EXAFS χ-k spectra at the Fe edge of 3ML thick bcc (110) Fe (black line), and $Fe_{80}Ni_{20}$ (red line), and $Fe_{50}Ni_{50}$ (green line) films. Notice the small influence of the alloy composition on the spectra. (b) calculated EXAFS χ-k spectra at the Fe edge of 3ML thick fcc (111) Fe (black line), and $Fe_{80}Ni_{20}$ (red line), and $Fe_{50}Ni_{50}$ (green line) films. Notice the larger influence in this case of the alloy composition on the spectra.

The last parameter that we varied is the film strain. In Figure 5.18a, we show the influence of 5% in-plane strain along the b-axis in the case of a bcc phase. Figure 5.18b shows the effect of the same uniaxial strain along one of the in-plane axis in the case of a fcc phase. In both cases, a 2.5% out-of-plane stress has been added to keep the unit cell volume constant. In the case of a fcc phase (Figure 5.18b), the effect of the strain is essentially a shift along the k-axis, the oscillation amplitudes remaining approximately the same. On the hand, a shift along the k-axis as well as a large change in the oscillation amplitudes is observed in the case of a bcc phase (Figure 5.18a). Consequently, the EXAFS spectra of a bcc phase will be very sensitive to an in-plane strain.
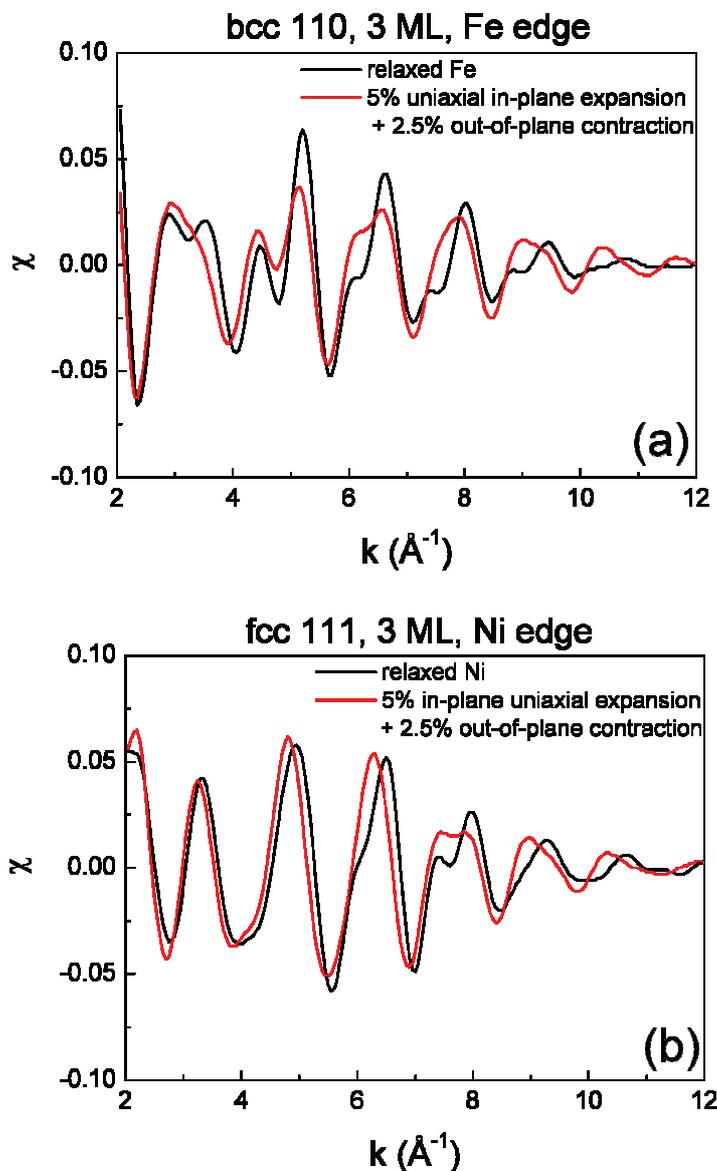
Figure 5.18 – (a) calculated EXAFS χ-k spectra at the Fe edge of 3ML thick bcc (110) Fe film strain−free (black line), and in the presence of 5% in−plane strain (red line). Notice the significant influence of the film strain on the oscillation amplitude. (b) calculated EXAFS χ-k spectra at the Fe edge of 3ML thick fcc (111) Fe film strain−free (black line), and in the presence of 5% in−plane strain (red line). Notice the smaller influence in this case of the film strain on the oscillation amplitude.

Following these simulations results, we will focus on the strain in the case of a bcc phase (Fe rich alloys) and on the alloy composition in the case of a fcc phase (Ni rich alloys). We will also investigate the possible presence of a fcc phase in a bcc one (and vice versa). In Figure

5.19a, we show the best fit of the experimental data in the case of the sample 5.6 ML $Fe_{75}Ni_{25}$. It was obtained by mixing the spectra of a bcc phase and a fcc phase with a ratio 70:30. The presence of the fcc phase improves significantly the fit. On the other hand, adding an in-plane strain does not seem to change the fit quality. This result is consistent with the XRD spectra where bcc and fcc phases were found. As explained above, we can not determine the alloy composition of each phase. Therefore, it is not possible for example to check whether the Ni content is significant in both phases, or whether the bcc phase contains mainly Fe and most of the Ni atoms are in the fcc phase. Unfortunately, because of the lack of beamline time, we could not measure the EXAFS spectrum of the sample at the Ni edge, which would have helped us in answering this question. The absence of strain in the EXAFS fit contrasts with the measured strain from the XRD spectra. We will come back to this point later on in the discussion section.
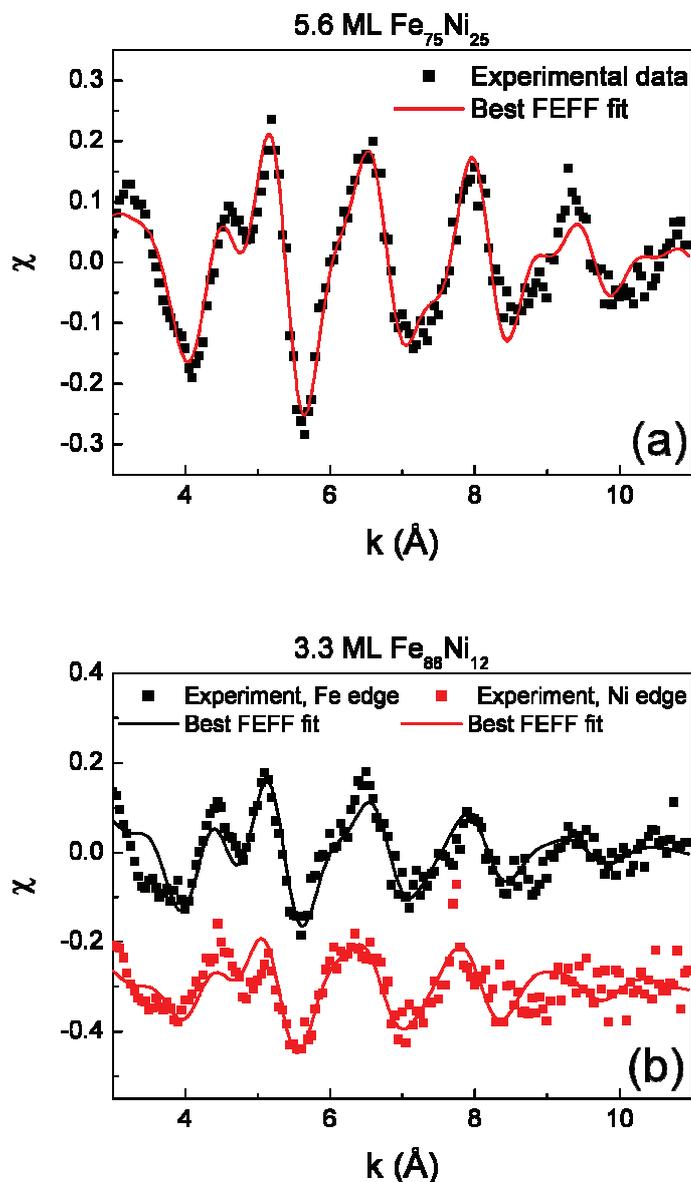
Figure 5.19 - (a) EXAFS χ-k spectrum at the Fe edge of 5.6ML thick Fe$_{75}$Ni$_{25}$ film (black symbols) and its best FEFF fit (red line), which is a combination of a bcc and fcc spectra with a respective weight of 70% and 30%. (b) EXAFS χ-k spectra at the Fe edge (black symbols) and Ni edge (red symbols) of 3.3ML thick Fe$_{88}$Ni$_{12}$ film and its best FEFF fits (black lines). The spectra at the Ni edge were shifted downwards for the sake of clarity.

In Figure 5.19b we applied the same fitting procedure to the EXAFS spectra of 3.3 ML Fe$_{88}$Ni$_{12}$. The spectrum at the Ni edge (in red) was shifted downwards for the sake of clarity. In this case, we could measure the spectra at Fe and Ni edges. The fitting of both spectra improves

if we mix 90% of a bcc phase spectrum and 10% of a fcc phase one. The best fit necessitates also to add 4% elongation along the b-axis (accompanied by 2% contraction along the direction perpendicular to the sample surface). These parameters allowed fitting both spectra. Here again, these results, especially in terms of the film 4% strain, contrast with the 10% strain determined from the XRD analysis. This disagreement will be deepened in the discussion section.

In the case of 3.4 ML $Fe_{41}Ni_{59}$, the best FEFF fits are shown in Figure 5.20 at the Fe (black) and Ni (red) edges (the spectrum at the Ni edge was shifted downwards for the sake of clarity). The parameters of these best fits were: (i) Fe gamma 111 structure compressively stressed by 2% ±0.5% along each in−plane axis, and (ii) a Fe content of 50% ±10%. The in-plane first neighbor interatomic distance of a Fe gamma structure is 2.57 Å. A compression of 2% decreases this distance to ~2.52 Å, which lies between the Ni (2.49 Å) and the Fe interatomic distances. In the case of solid solution, Vegard's law [22], which establishes a linear relationship between the alloy interatomic distance and the alloy composition may be used. If we apply this law to the $Fe_{41}Ni_{59}$ alloy, we expect an interatomic distance of $(0.41*a_{Fe-Fe} + 0.59* a_{Ni-Ni}) = 2.52$ Å (with $a_{Ni-Ni} = 2.49$ Å, and $a_{Fe-Fe} = 2.57$ Å) which is in good agreement with the value determined from the FEFF fits. This is a first indication that the $Fe_{41}Ni_{59}$ alloy forms most probably a solid solution. In order to simulate an alloy spectrum (for example at the Fe edge), we fitted the optimal proportion of two spectra: (1) that of a Fe atom surrounded by 100% of Fe atoms and (2) that of a Fe atom surrounded by 100% of Ni atoms. It is a more simple alternative way to simulate alloy spectra but is more efficient in terms of calculation time. In case the alloy is phase separated, the best FEFF fit should be obtained for ~100% proportion of the first spectrum and ~0% of the second. In case of a solid solution, the proportions should correspond to those of the alloy composition. It is indeed what we obtain for the best FEFF fit, which is a second proof that the $Fe_{41}Ni_{59}$ alloy forms a solid solution.
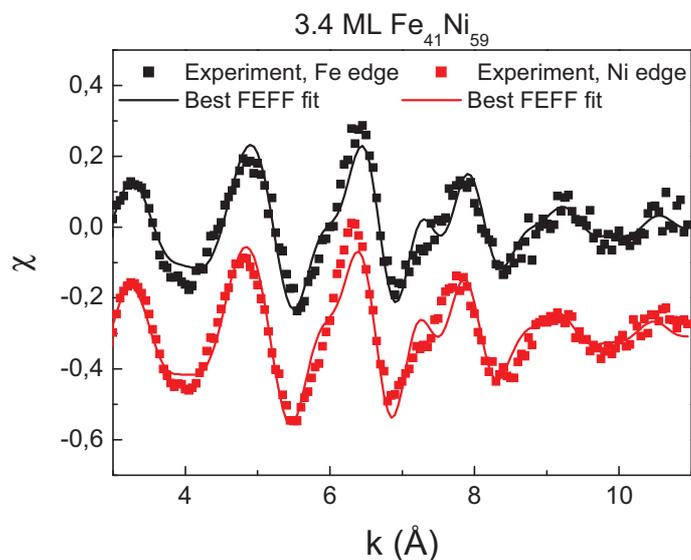
Figure 5.20 - EXAFS χ-k spectra at the Fe edge (black symbols) and Ni edge (red symbols) of 3.4ML thick $Fe_{41}Ni_{59}$ film and its best FEFF fits (black lines). The spectra at the Ni edge were shifted downwards for the sake of clarity.

5.4. Magnetic measurements

As explained in the introduction of this chapter, the magnetic properties of FeNi alloys are very rich and present a large variety of behaviors, which are closely related to the alloy composition and structure. Moreover, the magnetic moment per atom of Fe bcc (2.22 μ_B) and Ni (0.62 μ_B) are very different [3]. In this section, we will study the magnetic properties of our FeNi alloy films. We will use MOKE in the perpendicular (PMOKE) and longitudinal (LMOKE) configurations to measure the film hysteresis cycle with the magnetic field perpendicular or in the film plane. These measurements were done generally in-situ, which has the great advantage to capture the magnetic behavior as a function of the alloy thickness during its growth. We also measure the sample reflectivity during the alloy growth which enables us to estimate precisely the alloy thickness as function of time and allows us to directly correlate each measured hysteresis cycle with an alloy thickness. The uncertainty on the estimated thickness is ~0.1−0.2 ML. In order to make possible such precise correlation, we carefully calibrated the sample

reflectivity using the film dissolution charge in a large number of deposition/dissolution procedures covering a large thickness range. We also used this technique ex-situ to measure the hysteresis cycles of the Au capped samples that have been structurally characterized ex-situ. As using MOKE measurements does not allow to directly access the magnetic moment per atom, we performed SQUID measurements on the same Au capped samples. Measuring the absolute magnetic moment per atom is important in order to detect the presence of low / high spin phase. One may argue about the possibility of comparing the magnetic properties of Au capped alloy films with those of films in contact with the solution. Indeed, the magnetic properties of ultrathin films are sensitive in a complex way to the interface nature. However, it is very difficult to perform in-situ structural characterizations on films thinner than 2−3 ML, and we will keep in mind these differences when comparing both types of samples.

In the following, we will present the in-situ magnetic MOKE measurements followed by ex-situ ones.

Important remark: we will present the magnetic characterizations as a function of the alloy thickness and composition. In section 5.2, we showed that the alloy composition is thickness dependent. Consequently, when we present data as a function of the alloy thickness, one should bare in mind that the alloy composition is not constant. Moreover, the identification of the curves will be based on the composition of the deposition solution and not on the actual alloy composition (because it depends on the thickness). For this purpose, instead of using the usual $Fe_xNi_{100−x}$ notation, we will use the following one, Fe/Ni:x/100−x. Here again, one should keep in mind that the real alloy composition is different from that of the solution. However, when comparing data for a single thickness, the real alloy composition may be determined accurately and will thus be used.

5.4.1.   In-situ PMOKE and LMOKE measurements

We showed in the previous chapters that a practical way to analyze the hysteresis cycles as function of the deposit thickness is to plot the magnetic signal at the maximum applied field (typically 600 Oe) and the ratio of the remnant magnetization and the saturation magnetization as a function of the thickness. In Figure 5.21, we present the PMOKE and LMOKE signal at a field

of 600 Oe as a function of the deposit thickness for different alloy compositions. We also superimposed the data corresponding to pure Fe and Ni. The general shape of the curves magnetization / thickness for different alloy compositions is essentially the same: the magnetization increases with thickness at low thickness values (Figure 5.21a), reaches a maximum and then decreases more or less slowly at large thickness values. The magnetization decrease in the PMOKE measurement is accompanied by the magnetization take off in the LMOKE one (Figure 5.21b). It is followed by a quasi-linear increase as a function of the deposit thickness. As shown in the previous chapters, this behavior is characteristic of an out-of-plane (for low thickness values) to in-plane (for high thickness values) magnetization reorientation. It is due to a competition between interface, magneto-crystalline and shape anisotropies. In Figure 5.21a, we omitted displaying the curves of Fe/Ni:20/80 and pure Ni because in both cases, the signal remains essentially zero in this thickness range. Moreover, the open symbols correspond to experiments where the deposition is stopped at different deposit thicknesses. The very good agreement between these points and the magnetization / thickness curves demonstrates that our calibration of the reflectivity signal is precise.

Now let us analyze how the alloy composition alters these magnetization curves. The main difference between the PMOKE curves in Figure 5.21a may be summarized in three points:

1. the amplitude of the curve decreases with decreasing Fe content in the alloy. This may be a consequence of the smaller Ni magnetic moment per atom.
2. the position of the peak maximum decreases with decreasing Fe content. As explained in the previous chapters, the thickness corresponding to the magnetization maximum is related to the film magnetic anisotropies. We will discuss this point in details in the discussion section.
3. the smaller the Fe content the larger is the thickness of the take off of the magnetization at low thickness.

The LMOKE signal (Figure 5.21b) is complementary to the PMOKE one. No signal is observed up to a certain thickness, and then the signal increases abruptly to reach a uniform linear increase. The differences between different alloy compositions are essentially the signal amplitude and the thickness at which it takes off. The former may be due to the smaller Ni magnetic moment per atom, and the latter to different film magnetic anisotropy.
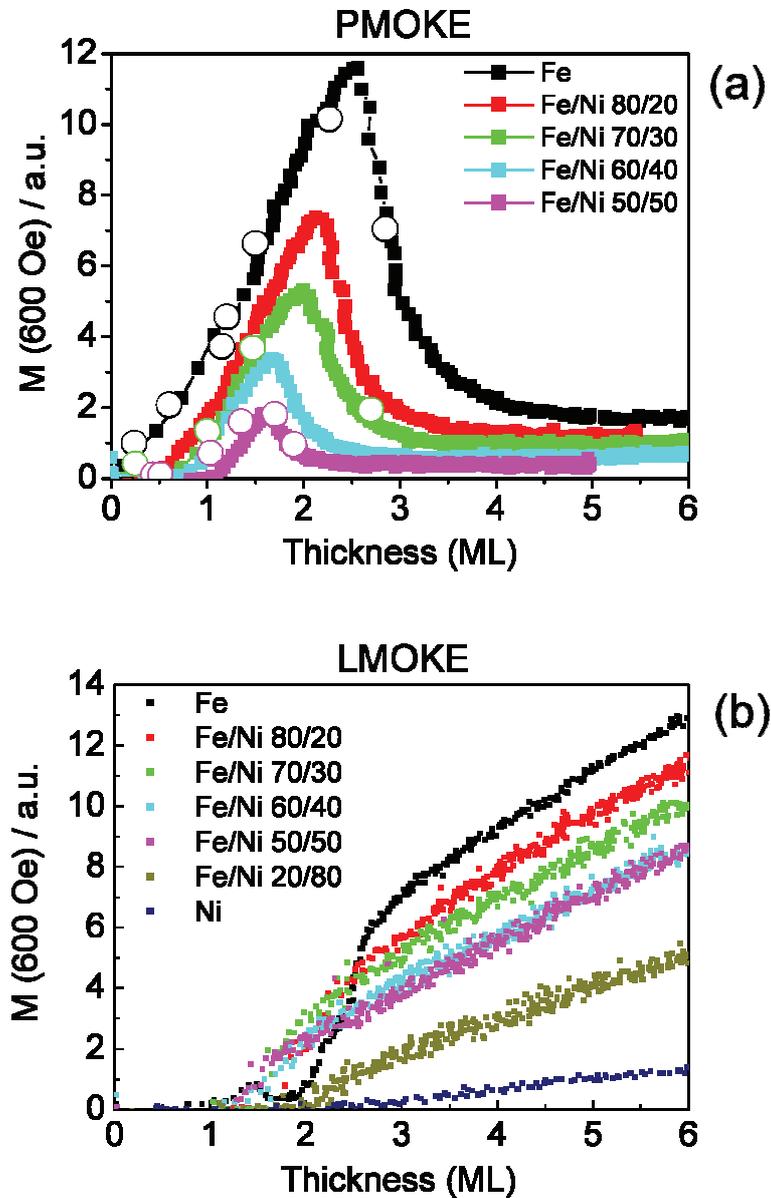
Figure 5.21 - PMOKE (a) and LMOKE (b) signal as a function of the alloy film thickness for different solution compositions: 0.5mM Fe^{2+} (black), 0.4 mM Fe^{2+} + 0.1 mM Ni^{2+} (red), 0.35 mM Fe^{2+} + 0.15 mM Ni^{2+} (green), 0.3 mM Fe^{2+} + 0.2 mM Ni^{2+} (cyan), 0.25 mM Fe^{2+} + 0.25 mM Ni^{2+} (pink), 0.1 mM Fe^{2+} + 0.4 mM Ni^{2+} (dark yellow), and 0.5 mM Ni^{2+} (dark blue). The symbols in (a) correspond to independent measurements demonstrating the correct determination of the alloy thickness.

The data shown in Figure 5.21 correspond to the magnetization at a magnetic field of 600 Oe, which is close to the saturation field. Figure 5.22 show the PMOKE hysteresis cycles of ~1.4 ML of alloys with different composition, including pure Fe. In this case, as the thickness is fixed, we could determine and display the exact alloy composition. Several interesting trends may be observed: (i) the coercive field of the hysteresis cycles decreases with decreasing Fe content and becomes zero between 56% and 47%. (ii) The hysteresis cycle shape is square down to a Fe content of 56% and then becomes reversible below 56%. These two variations may be a direct consequence of the change of the film magnetic anisotropy with the alloy composition.
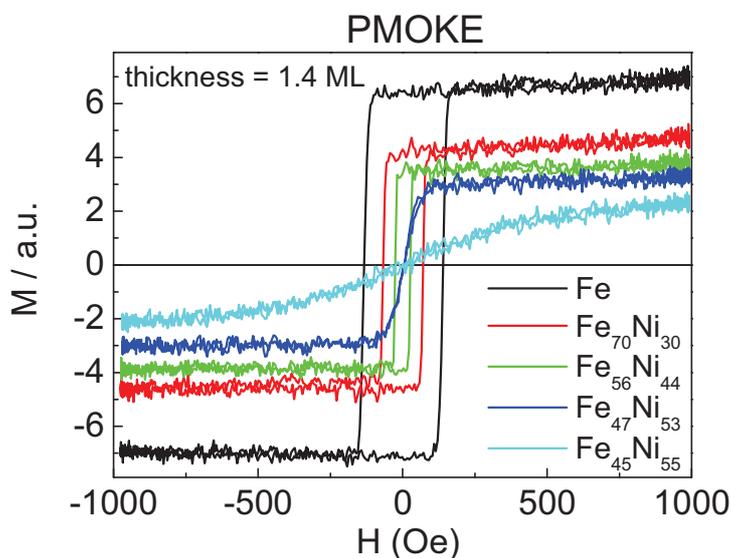
Figure 5.22 - PMOKE hysteresis loops of ~1.4ML thick alloy film with different alloy composition: Fe (black), $Fe_{70}Ni_{30}$ (red), $Fe_{56}Ni_{44}$ (green), $Fe_{47}Ni_{53}$ (dark blue), and $Fe_{45}Ni_{55}$ (cyan). The films were deposited at $-1.5\ V_{MSE}$.

It is interesting to determine for each alloy composition, the thickness range where the hysteresis cycles have a square shape, i.e. a remnant magnetization (Mr) close to the saturation magnetization (Ms). The ratio of these two quantities for the PMOKE and LMOKE signals as a function of the alloy is depicted in Figure 5.23. In the case of LMOKE signal, we only present the data for pure Fe. In agreement with the data of Figure 5.22, a square PMOKE hysteresis

cycle, or equivalently Mr/Ms ~ 1, is obtained for Fe rich alloys. However, the hysteresis cycles become square above a thickness of ~1.4 ML only. Below 1 ML, PMOKE Mr as well as LMOKE Mr are zero, which indicate the absence of stable magnetization of the film at room temperature. This behavior is most probably due to a lowering of the Curie temperature of Fe and Ni in the ultrathin film limit. Such behavior has already been reported on in the case of pure Fe and Ni films deposited by molecular beam epitaxy (MBE) on Cu in UHV [23,24]. More precisely, fcc Ni films deposited on Cu(111) and bcc Fe films deposited on Au(100) are ferromagnetic at room temperature if they are thicker than 2ML. The behavior of Ni is in agreement with our results where no PMOKE signal was measured and the uptake of the LMOKE signal takes place at ~2ML. In spite of the different substrates (Cu in the UHV study and Au in our case), this very good agreement is possible because in both cases, the Ni film is essentially strain free (see Figure 5.21b dark blue symbols). The case of Fe is clearly different as we start observing magnetic ordering at ~1.3ML at room temperature, significantly below the 2ML in UHV.

Similar dependence of Curie temperature on the film thickness were found for Fe rich FeNi alloys deposited on Cu(100) [6]. In the latter case, the FeNi alloy films were fcc (up to a Fe content up to 75%). In addition, in order to obtain a Curie temperature larger than room temperature, a film thicker than ~3 ML is necessary. This behavior contrasts with our findings where the Curie temperature of 1.4 ML thick alloy films is clearly larger than room temperature.
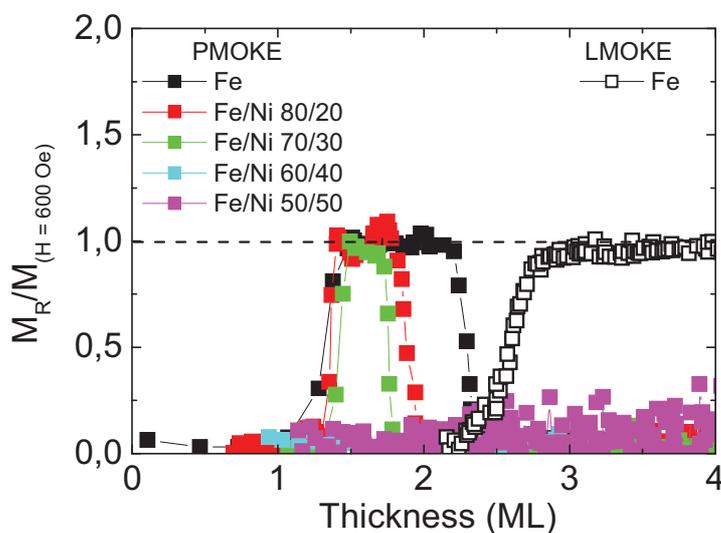
Figure 5.23 - PMOKE (closed symbols) and LMOKE (open symbols) Mr/Ms as a function of the alloy film thickness for different solution compositions: 0.5mM Fe^{2+} (black), 0.4 mM Fe^{2+} + 0.1 mM Ni^{2+} (red), 0.35 mM Fe^{2+} + 0.15 mM Ni^{2+} (green), 0.3 mM Fe^{2+} + 0.2 mM Ni^{2+} (cyan), 0.25 mM Fe^{2+} + 0.25 mM Ni^{2+} (pink). Notice the complementary behaviors of PMOKE and LMOKE.

Our results show that the pure Fe film and the two alloys with the largest Fe content reach Mr/Ms ~ 1 at approximately the same thickness, namely ~1.4ML ±0.1 ML. At this thickness, the Fe content in these films is respectively 100%, 70% and 56%, indicating that the Curie temperature of the films does not depend significantly on the Fe content above ~50%. This behavior is again in agreement with that of films deposited by MBE on Cu(100) [6]. Below 50%, the Curie temperature seems lower than the room temperature. After the increase of Mr/Ms at ~1.4ML, it drops back to zero at a thickness which depends on the Fe content of the alloy. In the case of pure Fe, Mr/Ms ~0.7 at 2.2 ML (Mr/Ms =0.7 corresponds to a magnetization orientation at ~45° with the respect to the sample surface). This critical thickness t^* corresponds also to the take off of the LMOKE Mr/Ms curve (open symbols in Figure 5.23). In the case of the other two alloys, the drop occurs at ~1.9ML and ~1.75 ML respectively. These values are related to the film magnetic anisotropies.

Before presenting the ex-situ measurements (next section), it is worth analyzing the MOKE signal during the dissolution of an alloy film. Indeed, we showed in section 5.2.1 that, in the case of alloy film thinner than 2ML, the dissolution current is characterized by the presence

of two peaks, which we assigned to Fe and Ni dissolution peaks. The attribution of these peaks was based on their position with respect to the Nernst potentials of Fe^{2+}/Fe and Ni^{2+}/Ni, the more negative peak corresponding to the less noble metal, here Fe. From the in-situ PMOKE results, we showed that the magnetization of an alloy film decreases with decreasing the Fe content and vanishes between 40 and 20%. This behavior originates essentially from the absence of magnetic ordering of pure Ni films in the thickness range 0-2ML due to the lowering of the Curie temperature. Consequently, the film magnetization is a direct indication of the Fe content of the alloy.

In Figure 5.24 we present the dissolution current during a positive potential sweep in the case of two alloy films ~1.4ML thick and which composition is $Fe_{78}Ni_{22}$ (Figure 5.24a black curve) and $Fe_{47}Ni_{53}$ (Figure 5.24b black curve). In order to directly compare the dissolution curves with the MOKE signal, we superimposed in each case the derivative as a function of time of the MOKE signal (red curves in Figure 5.24). The latter present a single peak during the complete dissolution of the alloy and the magnetization vanishes at the positive side of the peak. This peak overlaps within a good approximation with the more negative dissolution current peak. Following the analysis developed in the last paragraph, we can conclude that when the magnetization vanishes, i.e., at the positive side of the first dissolution current peak, then the Fe content of remaining film is rather low. In other words, we can confidently assign the more negative dissolution peak with that of the selective dissolution of Fe. Consequently, this allows us to validate the procedure used in section 5.2.1 to determine accurately the alloy composition from the dissolution curves in the 0-2ML thickness range. This is particularly important for further analysis of the magnetism data.
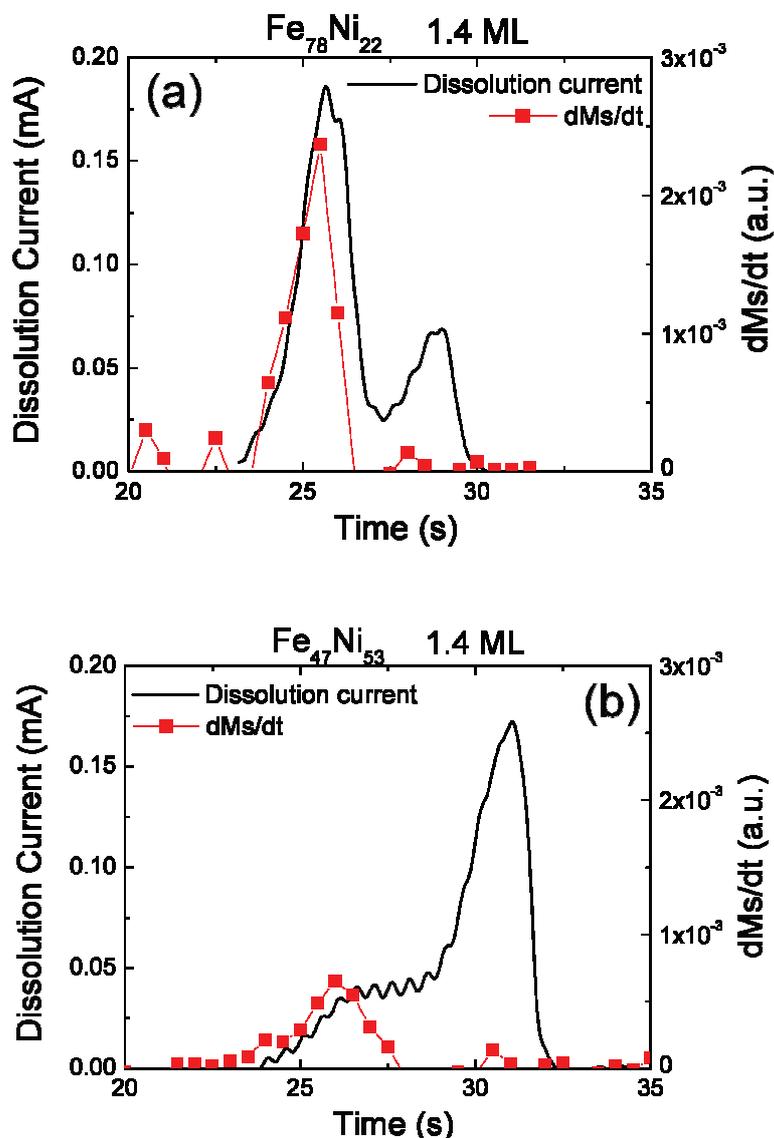
Figure 5.24 - Positive potential sweep in the Fe and Ni dissolution range showing the dissolution peaks (black lines) and the variation of the PMOKE signal derivative as a function of time (red symbols and line), in the case of 1.4ML thick $Fe_{78}Ni_{22}$ (a) and $Fe_{47}Ni_{53}$ (b) alloy films. The deposition potential is -1.5 V_{MSE}. Notice the good correlation between the PMOKE derivative and the more negative dissolution peak.

Let us see now how good is the correlation between the MOKE signal and the dissolution current for thicker alloy films. In Figure 5.25 we present similar analysis for alloy films ~3ML thick. The dissolution current still presents two peaks although they are much less defined than in Figure 5.24. On the other hand, the peak of the derivative of the PMOKE magnetization as a function of time is not correlated anymore with the more negative dissolution peak. Instead, it is

positioned in the center between the two dissolution peaks, indicating that Fe is not selectively dissolved before Ni dissolution starts. This behavior contrasts with that of thinner films and prevents us to determine the alloy composition from the dissolution current.
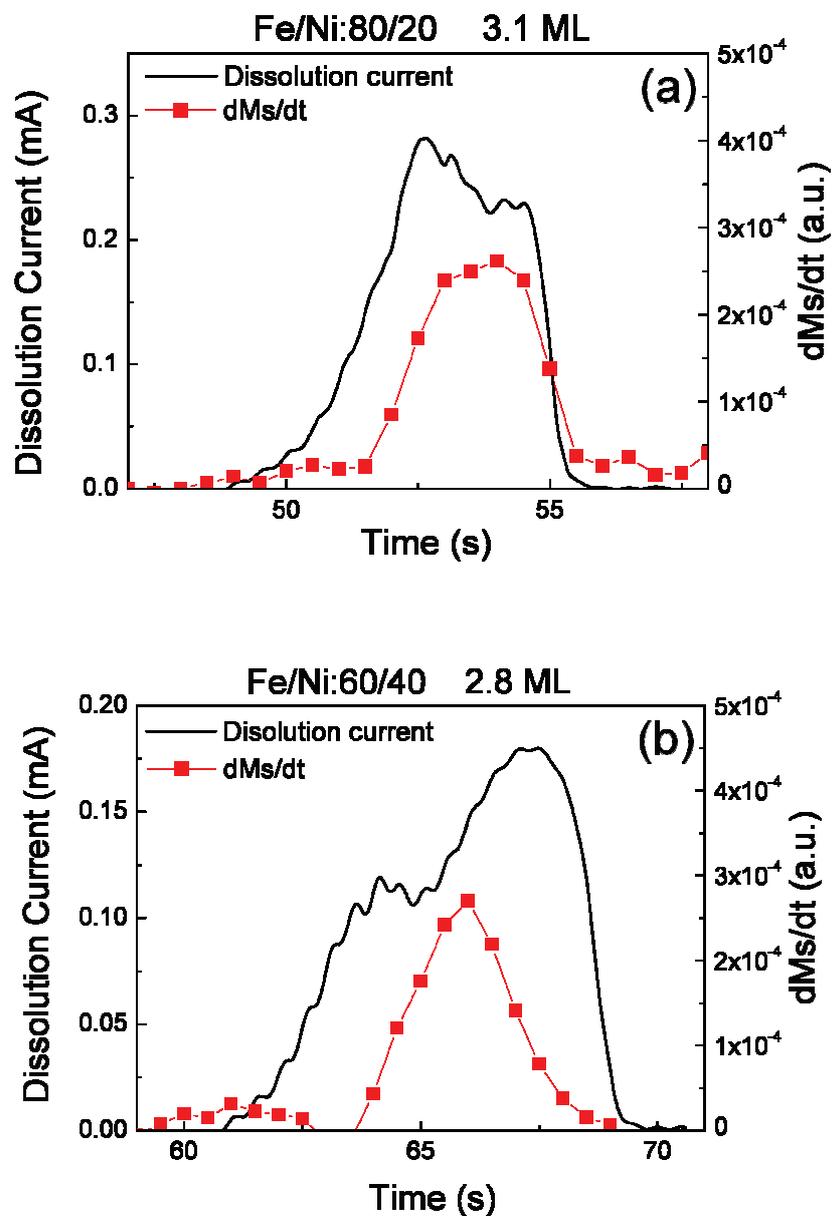
Figure 5.25 - positive potential sweep in the Fe and Ni dissolution range showing the dissolution peaks (black lines) and the variation of the PMOKE signal derivative as a function of time (red symbols and line), in the case of (a) 3.1ML thick film deposited in 0.4mM Fe^{2+} + 0.1mM Ni^{2+} solution and (b) 2.8 ML thick film deposited in 0.3mM Fe^{2+} + 0.2mM Ni^{2+} solution. The deposition potential is −1.5 V_{MSE}. Notice the bad correlation between the PMOKE derivative and the more negative dissolution peak.

5.4.2.   *ex-situ LMOKE and SQUID measurements*

The magnetic properties of the Au capped samples prepared for ex-situ X-ray and EXAFS experiments could not be measured in-situ because of the specific cell used for Au capping. However, we performed these measurements ex-situ, and analyzed them in order to compare them with in-situ measurements. Of course, one should keep in mind that these samples may differ from their in-situ equivalents by at least two aspects, namely, the upper alloy film interface and the film strain. These differences are expected to alter the film magnetic anisotropy and average moment per atom. In addition to the ex-situ MOKE measurements, we did also SQUID measurements between 10°K and room temperature, which allowed us to determine the absolute magnetization of the samples and to determine whether the film Curie temperature is close to room temperature.

In Figure 5.26, we show typical hysteresis loops of 3.4ML Fe$_{41}$Ni$_{59}$ (black line) and 5.7ML Fe$_{75}$Ni$_{25}$ (red line) obtained by LMOKE. The acquisition of a single hysteresis cycle took typically few seconds. We also superimposed a hysteresis cycle from an in-situ experiment (green line) which amplitude has been adjusted to equals its equivalent of an ex-situ sample. Although the in-situ cycle has been acquired 4 times faster than the ex-situ sample, the coercive field of the ex-situ sample is significantly larger. This indicates that the Au capping increases the in-plane magnetic anisotropy of the film. The square hysteresis loops of the ex-situ samples indicate that the magnetization easy axis is in the film plane, which is in full agreement with the in-situ data.
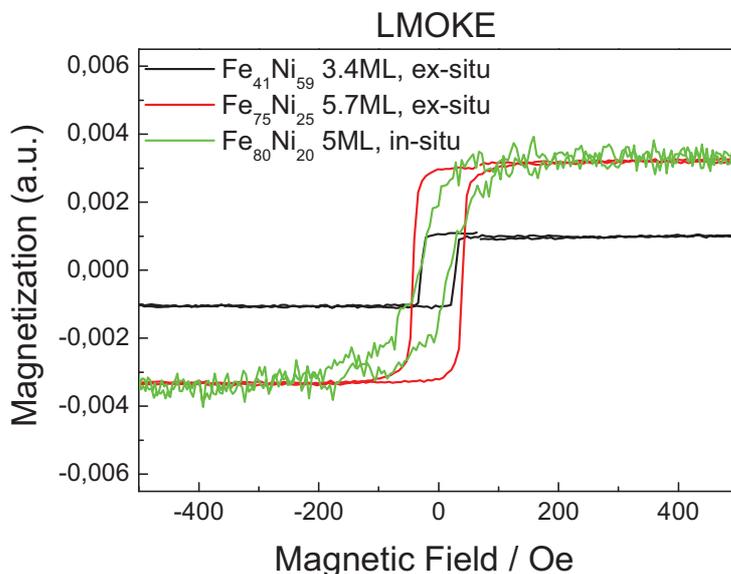
Figure 5.26 - *Ex−situ* **LMOKE hysteresis loops of 3.4ML thick $Fe_{41}Ni_{59}$ (black line) and 5.7ML thick $Fe_{75}Ni_{20}$ (red line) alloy films. For comparison we superimposed an in−situ LMOKE hysteresis loop of 5ML thick (green line) deposited in 0.4mM Fe^{2+} + 0.1mM Ni^{2+} solution. The films were deposited at −1.5 V_{MSE}.**

In Figure 5.27a, we present the hysteresis loops of the same samples of Figure 5.26 obtained by SQUID at room temperature and at 10°K. The acquisition of each hysteresis cycle took typically 1-2 hours. The cycles measured at room temperature (red and blue curves) have no coercivity in contrast with LMOKE measurements. This is mainly due to the difference in the acquisition conditions which are, equivalent to a quasi-static measurement when the SQUID is used whereas they correspond to a dynamic one with the MOKE. The cycles obtained at 10°K have a significant coercivity which is related to the in-plane magnetic anisotropy of the films. The amplitude of the cycles is only slightly larger at low temperature when compared to room temperature one, which suggests that the Curie temperature of these films is significantly higher than room temperature. We also performed temperature dependent measurements at a constant magnetic field (corresponding to the sample saturation). The resulting curves are presented in Figure 5.27b for four different samples. In all cases, the maximum observed deviation of the magnetization from its value at 10°K is typically 14% for ~5ML thick films and 23% for ~3ML film. This shows that the Curie temperature of all of the Au capped alloy samples is higher than

room temperature, but lower than the bulk one. Consequently, the measured moment per atom for these thin films is smaller than that for bulk alloys.
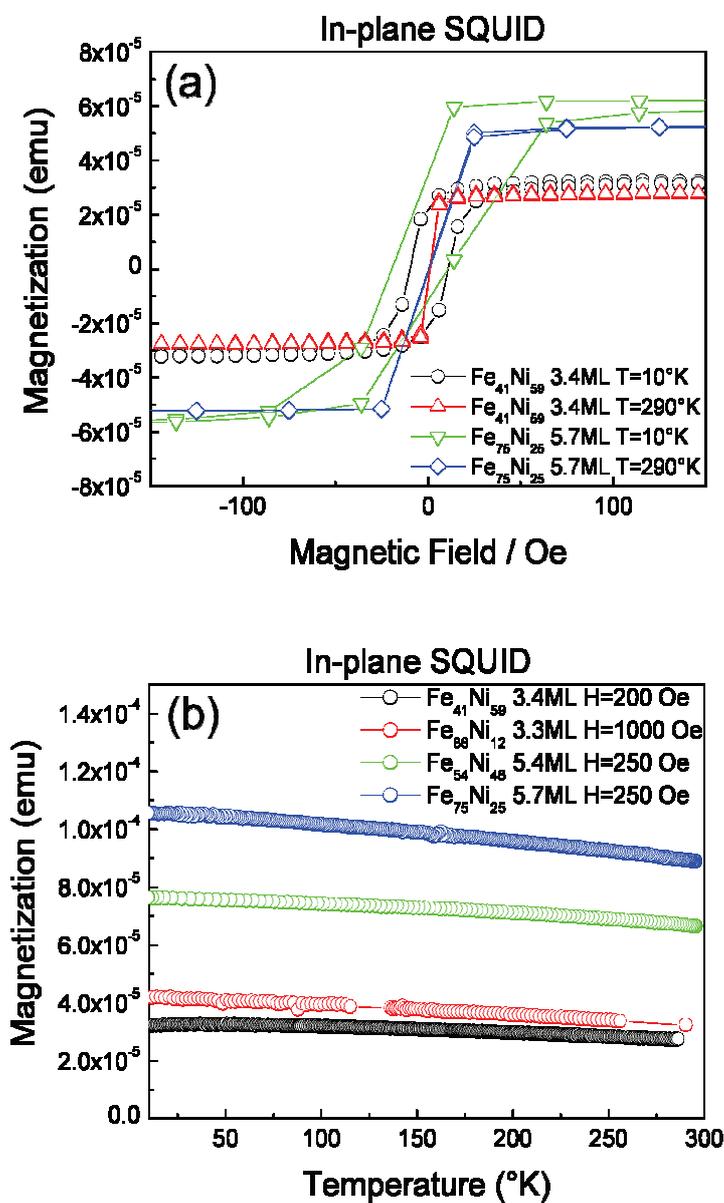
Figure 5.27 - (a) ex−situ in−plane SQUID hysteresis loops of alloy films: 3.4ML Fe$_{41}$Ni$_{59}$ at 10°K (black symbols and line) and at 290°K (red symbols and line); 5.7ML thick Fe$_{75}$Ni$_{20}$ at 10°K (green symbols and line) and at 290°K (dark blue symbols and line). (b) ex−situ in−plane SQUID signal at saturation as a function of the sample temperature of alloy films: 3.4ML Fe$_{41}$Ni$_{59}$ (black symbols and line), 3.3ML Fe$_{88}$Ni$_{12}$ (red symbols and line), 5.4ML Fe$_{54}$Ni$_{46}$ (green symbols and line) and 5.7ML Fe$_{54}$Ni$_{46}$ (dark blue symbols and line).

In order to cross correlate the two types of experiments, LMOKE and SQUID, we compared the magnetization amplitudes obtained by the two techniques for the different samples. The results are shown in Figure 5.28, where the black columns correspond to LMOKE and red ones to SQUID. The latter values are absolute values, whereas the former ones have to be normalized. For this purpose we considered that the MOKE signal of the 5 ML thick pure Fe layer correspond to a fully magnetized layer with a magnetic moment per atom of 2.2 μ_B. In spite of a significant disagreement for a couple of samples, the overall results are well correlated. The discrepancy may originate from the sample inhomogeneity, especially that of the Au capping. Indeed, in a SQUID experiment, the total magnetization of the sample is measured independently on the capping thickness, whereas in a MOKE experiments ~1 mm^2 of the sample surface is measured and the incident light has to cross the capping layer. We indeed observed that the magnetization amplitude measured on different sample regions may differ.
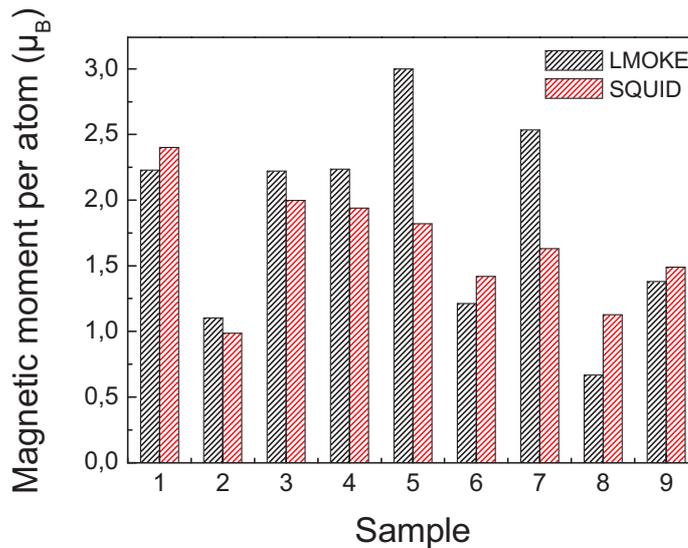
Figure 5.28 - : comparison between the ex−situ LMOKE (black columns) and SQUID (red columns) for different FeNi alloy films (3−5ML thickness range). The LMOKE signal was normalized in μ_B considering that the signal of the 5ML thick Fe film corresponds to 2.2 μ_B per atom. Notice the good agreement between the results of the two techniques.

5.5. Discussion

We will first recall the main conclusion regarding the morphology and the structure of the alloy films as a function of the alloy composition. Then we will focus on the magnetic results obtained in the different experiments and try to cross correlate them to determine a general trend as a function of the alloy composition.

5.5.1. *Morphology, structure and composition*

From the electrochemical measurements, we attributed the more negative dissolution peak of the alloy to selective Fe dissolution. This peak is shifted to more positive potentials as compared to pure Fe, suggesting that the presence of Ni in the deposit makes Fe nobler. This behavior is different from that of Fe deposited on Ni (chapter 4). This result suggests that the FeNi alloy most probably forms a solid solution and is not phase separated. The correlation of the electrochemical dissolution measurements with the reflectivity measurements allowed us to determine accurately the alloy composition from the two dissolution peaks in the 0−2ML range. For thicker deposits, the correlation between the more negative dissolution peak and the Fe content is no more possible. These results as well as the attribution of the more negative peak to selective Fe dissolution are in perfect agreement with the magnetic measurements during the alloy dissolution. Indeed, the magnetization vanishes within the more negative peak. In the same time, for thicker deposits, the magnetic signal is present up to the complete dissolution of the alloy, indicating that Fe selective dissolution from the alloy is no more possible. The alloy composition thus determined varies significantly with the alloy thickness with the following general trend: the composition is close to 50/50 for small alloy thickness, and tends to the solution composition close to 2ML.

The STM results showed that the alloy films are atomically flat, which is in agreement with the fact that pure Ni and pure Fe grow layer-by-layer on Au(111). The STM work was not extensive enough to extract more information from the morphological observation. For example, we could not evidence the presence of a moiré pattern which would have helped us in determining the alloy interatomic distance and consequently the in-plane film strain. The latter information is important for understanding the magnetic behavior. On the other hand, the flat

morphology of our deposits is essential for the further analysis, as it means that considering 2D films in the EXAFS and magnetism models is appropriate.

The XRD and EXAFS data give a rather complicated picture of the structure of the alloy films as a function of the alloy composition. For alloys with almost equal Fe and Ni contents, the film structure if fcc (111) in epitaxy with the Au(111) surface. Both XRD and EXAFS results agree on this point. Moreover, the best FEFF fit of the EAXFS data may be obtained only by considering a FeNi solid solution. This conclusion is in good agreement with the electrochemical measurements which showed that Fe in FeNi alloys becomes nobler. This behavior clearly suggests that the FeNi alloys are not phase separated. The interatomic distance determined from the EXAFS simulations is ~2.52 Å, which is in reasonable agreement with the Vegard's law. The Fe rich (Fe content > 75%) alloys have a clearly different crystallographic structure. The EXAFS results show the presence of a bcc structure with a small proportion of a fcc structure, which is in agreement with the XRD spectra. However, the small Ni content of these alloys and the small difference in the atomic numbers of Fe and Ni did not allow us to determine whether the Fe rich alloys form a solid solution. However, as we found in the electrochemical measurements that the dissolution peak of Fe is shifted positively in the same way as for the other alloys, we conclude that the Fe rich alloys form also a solid solution. We could also measure the in-plane film strain. We found that the bcc (110) alloy films are expanded along the b direction. This behavior is identical to that observed for pure Fe (chapter 3) and allows better registry between the film and the substrate. However, the values deduced from the XRD peak fitting are typically twice as large as those determined from EXAFS spectra fitting. This disagreement may appear at first sight surprising. Let us consider what do we measure in each type of experiment? In XRD, we measure the interplanar distance average over the coherence length of the X-ray incident beam (typically 1 μm on a synchrotron beamline), which much larger than the interatomic distances. Therefore, the presence of defects in the film within this scale (lattice distortion for example at the boundary between neighboring alloy domains) will yield an apparent increase of the average lattice distance. It will also significantly broaden the diffraction peaks, which is the case (see Figure 5.12 and Figure 5.13). In EXAFS, we observe the effect of the electron diffusion on the neighboring atoms. The contribution to the EXAFS signal of the atoms few atomic distances far from the central atom is rather negligible. Therefore, we probe the atomic environment over a length of few interatomic distances only. If we consider that the film defects are confined at the

alloy domain boundary, only the atoms situated few atomic distances close to these boundaries will experience the change in the atomic environment. Because the surface density of these atoms is much lower than that of the atoms within the domains, their contribution to the EXAFS signal will be negligible.

In conclusion, the EXAFS and XRD data show that the alloy films form a solid solution and undergo a bcc to fcc structural transition in the Fe content range of 45−70%. This transition seems to take place in the same Fe content range as for the bulk alloys. Regarding the film strain, XRD and EXAFS results are consistent together if we assume that the alloy films consist in domains with moderate in-plane strain separated by domain boundaries with large lattice distortion. Now let us see if this transition affects the magnetic properties.

5.5.2. *Magnetism*

As we explained in the introduction, there has been a large debate about the average magnetic moment per atom of the FeNi alloys films. Indeed, in the case of bulk alloys, the magnetic moment per atom does not follow a simple linear relationship as a function of the Fe and Ni contents as shown in Figure 5.29a [3]. Instead, it follows a rather complex behavior with a dip at ~65%. This dip corresponds to a transition between a bcc phase at larger Fe content to a fcc one at lower Fe content. A large theoretical effort has been made to understand the average magnetic moment per atom of the fcc phase, the larger Fe moment per atom than that in the bcc phase and the moment change close to the fcc-bcc transition [5,25,26]. They point out to the important influence of average number of neighbors of the Fe atom as well as the atomic volume (see [26] and references therein). The case of FeNi ultrathin films prepared in UHV is essentially similar to that of bulk alloys except that the fcc phase may be stabilized up to 75% Fe content [6,27].

In the following, we will cross correlate our different magnetic measurements and compare them with those obtained for bulk alloys. In Figure 5.29, we superimposed the LMOKE signal that we measured in-situ for 3ML (closed black squares) and 5ML (closed red circles) films as a function of the alloy composition. In this case, we could not determine the alloy composition precisely, as it was possible for the 1.4ML samples (because of the reasons detailed in section 5.2). Therefore, we considered that the alloy composition is similar to that of the

solution. This approximation is reasonable for films thicker than 3 ML, because the deposition rate is then mainly limited by the diffusion of Fe^{2+} and Ni^{2+} in the solution towards the Au substrate. The deposition flux of each ion is then determined by the concentration and the diffusion coefficients (0.72 cm^{2}s^{-1} and 0.66 cm^{2}s^{-1} for Fe^{2+} and Ni^{2+} respectively [28]). In order to compare the in-situ measurements and the magnetic moment per atom for bulk alloys (black curve), we adjusted the right axis scale (corresponding to the LMOKE signal) to make the data points for pure Fe (black curve and 5ML thick films) coincide. Indeed, as shown in chapter 3, our pure Fe films thicker than 3 ML are bcc, as determined from EXAFS, XRD and magnetic anisotropy analysis of the PMOKE signal.

The 5ML films appear to have a rather linear dependence on the alloy composition. For low Fe content, the points follow almost perfectly the bulk alloy curve, whereas at high Fe content, they follow the black line, i.e. the signal is proportional to the Fe content. The transition takes place in the Fe content range of 50−60%. The behavior of the 3ML thick film is essentially similar, except that the data point of pure Fe is lower than expected and that the linear dependence is not strictly observed. The latter is most probably due to the low measured signal in this case, especially for Ni-rich alloys. The former originates from the known lower Curie temperature of ultrathin films [23]. Now let us see if these LMOKE results are consistent with the PMOKE results.
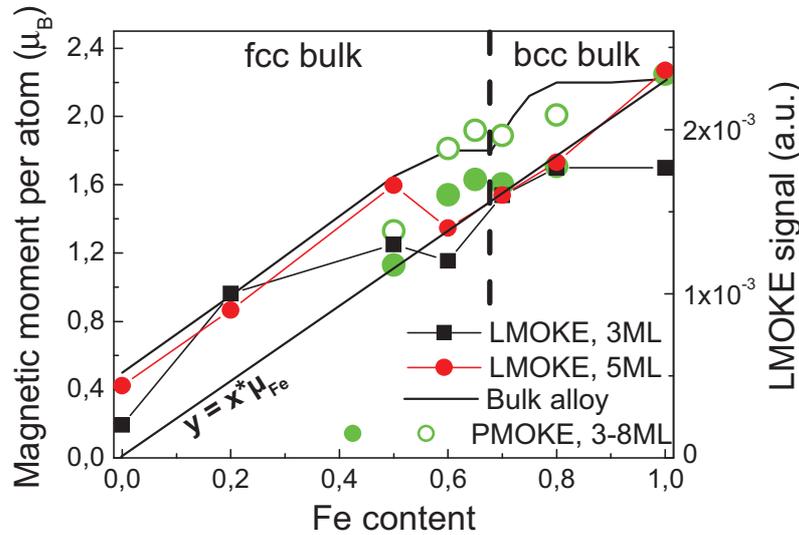
Figure 5.29 - Comparison between the in−situ LMOKE signal of 3ML (black line and symbols) and 5ML (red line and symbols) as a function of the alloy composition. We also superimposed the data determined from the PMOKE analysis (green closed symbols) and their extrapolation at low temperature (green open symbols). The LMOKE scale was adjusted in a way that the signal of the 5ML thick Fe film corresponds to 2.2 μ_B per atom. We also added the bulk magnetic moment of FeNi alloys (black curve) and the marked the composition of the fcc−bcc structural transition.

One way to analyze the PMOKE data in the large thickness range is to follow the same procedure as for the case of pure Fe (chapter 3). This procedure allows one to determine the interface and magneto-crystalline anisotropy constants of the film. Or inversely, if the magneto-crystalline constant is fixed, this data analysis yields the saturation magnetization of the film and the interface anisotropy. In the case of the alloys, we will use the latter way of analyzing the data. Although we do not know the magneto-crystalline constants of our films, we expect them to be negligible. Indeed, it has been shown experimentally that they lay below 10^5 erg.cm^{-3} in the Fe content range 10%-90% in the case of evaporated FeNi films [29]. Moreover, this analysis procedure is particularly interesting in the present case because it yields the saturation magnetization which is an important issue in the case of an alloy. The result is displayed in Figure 5.29 (green closed circles). The agreement between these data points and the LMOKE results is relatively good, taking into account the facts that the PMOKE signal is one order of magnitude lower in this thickness range as compared to below 2ML, and that the lower the Fe

content, the lower is the PMOKE signal and the larger is the uncertainties regarding the determination of the film magnetization. Now, how to compare these data points with the bulk magnetic moment per atom (black curve). We already mentioned that the small film thickness decreases the Curie temperature, thus inducing a lowering of the magnetic moment per atom at room temperature. In order to overcome this uncertainty, one would have to compare data at low temperature. In the case of bulk alloy, the magnetic moment per atom does not change significantly (~1%) between room temperature and for example 10°K, in the case of Fe rich alloys, because the Curie temperature in this case is rather high. However, in the case of ultrathin films, we clearly demonstrated by temperature dependent SQUID measurements that the moment decrease between 10°K and room temperature may be as large as 15% (see Figure 5.27). Once the data is corrected for this decrease, the bulk and the ultrathin films may be more easily compared. The resulting corrected data is shown as open green circles in Figure 5.29. Although the agreement is not perfect, especially when the Fe content is close to 50%, the data points are closer to the magnetic moment of a bcc structure, and well below that of a fcc structure. On the basis of these results, one may confidently conclude that the Fe rich FeNi alloy films form a bcc structure. This is in agreement with XRD and EXAFS conclusions.

Finally, let us compare the in-situ LMOKE data with the ex-situ SQUID data of the Au capped samples. In Figure 5.30, we superimposed the room temperature SQUID measurements of 3 ML (open black squares) and 5 ML (open red circles) thick samples. The agreement for the 3ML samples and the 3ML LMOKE data is good. It is also the case for the 5ML data points in the case of pure Fe and Ni rich alloys. Moreover, the data points coincide with the bulk curve in the case of Ni rich alloys (fcc FeNi alloy region). This is in full agreement with the XRD and EXAFS data analysis showing that in the Fe content range, the alloy film are fcc. However, the two data points of the 5ML films, which correspond to $Fe_{54}Ni_{46}$ and $Fe_{75}Ni_{25}$ alloys, are clearly different from the LMOKE data and also from the bulk behavior (black curve). We do not understand this discrepancy. It does not originate from miss estimating of the sample area or of the presence of some impurities in the SQUID. The SQUID extraction curves were not noisy and the hysteresis loops were square (see Figure 5.27). Moreover, we also observe this deviation by ex-situ LMOKE measurements. In the case of $Fe_{75}Ni_{25}$, EXFAS showed that the alloy structure is partly (~30%) fcc. Even if we take into account the higher magnetic moment of the fcc structure, we should end up with an average moment per atom of ~1.9 μ_B, which well below the

2.4 μ_B we measure. Although it has been shown that the capping layer may influence the magnetic anisotropy of Co films [30] or the Curie temperature in the case of Fe films [31], it is not clear how the magnetic moment of the alloy film may be increased by adding a Au capping layer.
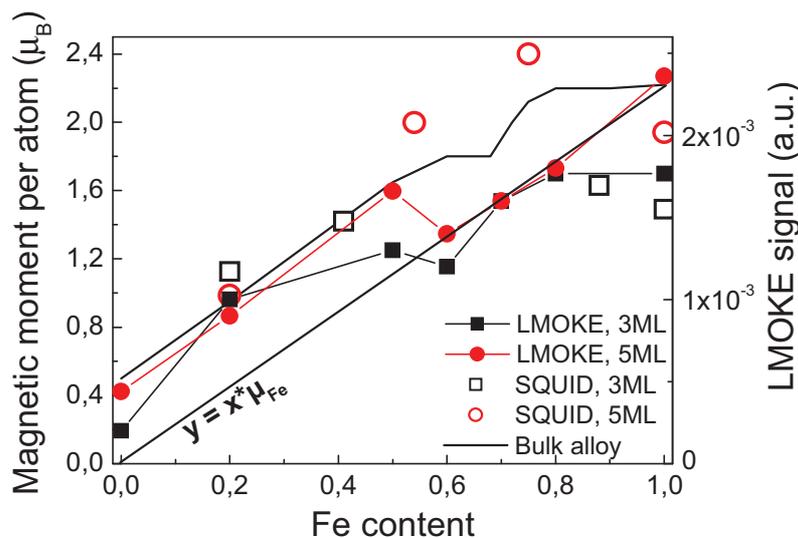

Figure 5.30 - comparison between the in−situ LMOKE signal of 3ML (black line and symbols) and 5ML (red line and symbols) as a function of the alloy composition. We also superimposed the data determined from the ex−situ SQUID measurements of ~3ML (black open symbols) and ~5ML (red open symbols) films. The LMOKE scale was adjusted in a way that the signal of the 5ML thick Fe film corresponds to 2.2 μ_B per atom. We also added the bulk magnetic moment of FeNi alloys (black curve).

Now, we still have two additional questions to answer:

1. Where does the fcc-bcc transition take place?
2. What is the reason for the drop in magnetization observed at a Fe content of 60%?

It is tempting to associate the observed drop in the alloy magnetization at a Fe content of 60% with the fcc to bcc structural transition. Indeed, a drop in the magnetic moment as well as in the Curie temperature is expected close to the fcc-bcc transition (see for example [6,32] and references therein). A fcc to bcc transition at a Fe content of 60% would be in good agreement with the EXAFS and XRD data. However, if it is the case, it is not clear why the magnetic

162

moment, which follows the bulk magnetic behavior for low Fe content, remains significantly different from it for large Fe content, and remains proportional to the Fe content. The disagreement may be also presented in a second way. Let us assume that the difference between the measured LMOKE signal and the bulk behavior is essentially due to the low Curie temperature, which is reasonable as discussed above. How come that below a Fe content of 60%, the film magnetic moment does not seem to be affected by the low Curie temperature and follows strictly the bulk magnetic behavior? One possible origin of this abrupt magnetization change is a structure dependent MOKE signal. If this hypothesis is true, then the fcc to bcc transition takes indeed place at a Fe content of ~60%. This value is well below that obtained in UHV on Cu substrates, where it was possible to stabilize the fcc structure up to 75% Fe content [6]. These differences between the UHV and the electrochemical behavior point to the important influence of the film / electrolyte interface

5.6.   Conclusion

In this chapter, we studied the magnetic properties of FeNi alloy ultrathin films as function of their structure and their composition. Using the electrochemical dissolution curves correlated with the reflectivity and magnetic measurements, we succeeded in accurately estimating the alloy film composition in the thickness range 0−2ML. We also evidenced a thickness dependent composition starting from a 50/50 composition to reach at ~2ML, the solution one. We performed XRD and EXAFS experiments, which allowed us to conclude on the structure of the film and the in-plane strain. We could show that the Fe rich alloys form mainly a bcc structure and contain a tensile strain, whereas the Ni rich alloys are fcc with smaller in-plane strain. The difference between the strain values determined from XRD and from EXAFS allowed us to speculate on the spatial distribution of the lattice distortion, namely, the alloy films consist in alloy domain with moderate strain separated by domain boundaries with large lattice distortion. We measured the magnetic properties of these alloy films in-situ and ex-situ using PMOKE, LMOKE and SQUID. We succeeded in correlating the results of these different measurements, taking into account the magnetization drop of the alloy film due to the ultrathin geometry. We evidenced a clear drop of the average magnetic moment at a Fe content of ~60%,

which we attribute to the fcc to bcc structural transition. The fact that this transition takes place at significantly lower Fe content than in UHV indicate the strong influence of the solution on the magnetic properties of the FeNi alloy films.

5.7. Bibliography

1   Andreas Moser, Kentaro Takano, David T. Margulies et al., "Magnetic recording: advancing into the future," Journal of Physics D: Applied Physics **35** (19), R157-R167 (2002).

2   P. P. Freitas, R. Ferreira, S. Cardoso et al., "Magnetoresistive sensors," Journal of Physics: Condensed Matter **19** (16), 165221 (2007).

3   Peter Mohn, *Magnetism in the solid state*. (Springer, Berlin, 2006).

4   F. O. Schumann, R. F. Willis, K. G. Goodman et al., "Magnetic Instability of Ultrathin fcc FexNi1-x Films," Physical Review Letters **79** (25), 5166 (1997).

5   I. A. Abrikosov, O. Eriksson, P. Söderlind et al., "Theoretical aspects of the FecNi1-c Invar alloy," Physical Review B **51** (2), 1058 (1995).

6   F. O. Schumann, S. Z. Wu, G. J. Mankey et al., "Growth and magnetic properties of CoxNi1-x and FexNi1-x ultrathin films on Cu(100)," Physical Review B **56** (5), 2668 (1997).

7   H. Brune, "Microscopic view of epitaxial metal growth: Nucleation and aggregation," Surface Science Reports **31** (3-4), 125-229 (1998).

8   H. E. Hoster, E. Filonenko, B. Richter et al., "Formation and short-range order of two-dimensional Cu[sub x]Pd[sub 1 - x] monolayer surface alloys on Ru(0001)," Physical Review B (Condensed Matter and Materials Physics) **73** (16), 165413-165411 (2006); H. Hartmann, T. Diemant, A. Bergbreiter et al., "Surface alloy formation, short-range order, and deuterium adsorption properties of monolayer PdRu/Ru(0 0 0 1) surface alloys," Surface Science **603** (10-12), 1439-1455 (2009); W. L. Ling, J. C. Hamilton, K. Thürmer et al., "Herringbone and triangular patterns of dislocations in Ag, Au, and AgAu alloy films on Ru(0 0 0 1)," Surface Science **600** (9), 1735-1757 (2006).

9   Y. Sato, T. F. Johnson, S. Chiang et al., "Magnetic domain structures in ultrathin Fe[sub x]Ni[sub (1 - x)] films on Cu(111): Dependence on film thickness and stoichiometry," Journal of Vacuum Science & Technology A: Vacuum, Surfaces, and Films **22** (1), 135-139 (2004); H. G. Lee, I. G. Baek, S. Kim et al., "Electronic and magnetic properties in Fe-based Fe1-xNix, Fe1-xCox, and Fe1-xVx films on W(1 1 0)," Surface Science **600** (18), 4137-4142 (2006).

10 Bai An, Lin Zhang, Seiji Fukuyama et al., "Fe-Ni Surface Alloy Formation on Ni(111) Investigated by Scanning Tunneling Microscopy," Jpn. J. Appl. Phys. **47** (7), 6081 (2008).

11 M. Ondracek, F. Maca, J. Kudrnovsky et al., "Chemical ordering and composition fluctuations at the (001) surface of the Fe[sub 64]Ni[sub 36] Invar alloy," Physical Review B (Condensed Matter and Materials Physics) **74** (23), 235437-235437 (2006).

12 Wendy C. Grande and Jan B. Talbot, "Electrodeposition of Thin Films of Nickel-Iron," Journal of The Electrochemical Society **140** (3), 675-681 (1993); Patrick Fricoteaux and Céline Rousse, "Influence of substrate, pH and magnetic field onto composition and current efficiency of electrodeposited Ni-Fe alloys," Journal of Electroanalytical Chemistry **612** (1), 9-14 (2008).

13 Wendy C. Grande and Jan B. Talbot, "Electrodeposition of Thin Films of Nickel-Iron," Journal of The Electrochemical Society **140** (3), 669-674 (1993); Keith Y. Sasaki and Jan

B. Talbot, "Electrodeposition of Iron-Group Metals and Binary Alloys from Sulfate Baths," Journal of The Electrochemical Society **145** (3), 981-990 (1998).

14 A. Lachenwitzer and O. M. Magnussen, "Electrochemical quartz microbalance studies on the kinetics of Ni monolayer and multilayer electrodeposition on (111)-oriented Au films," Journal of the Physical Chemistry B **104**, 7424-7430 (2000).

15 Edward D. Palik, *Handbook of Optical Constants of Solids*. (Academic Press, London, 1985); Edward D. Palik, *Handbook of Optical Constants of Solids II*. (Academic Press, London, 1991); P. B. Johnson and R. W. Christy, "Optical constants of transition metals: Ti, V, Cr, Mn, Fe, Co, Ni, and Pd," Physical Review B **9** (12), 5056 (1974).

16 J. Erlebacher, M. J. Aziz, A. Karma et al., "Evolution of nanoporosity," Nature **410**, 450-453 (2001); K. Sieradzki, N. Dimitrov, D. Movrin et al., "The dealloying critical potential," Journal of the Electrochemical Society **149**, B370-B377 (2002).

17 Allen J. Bard and Larry R. Faulkner, *Electrochemical Methods: Fundamentals and Applications, 2nd Edition*. (John Wiley & Sons, New York, 2001).

18 N. Zech, E. J. Podlaha, and D. Landolt, "Anomalous Codeposition of Iron Group Metals: I. Experimental Results," Journal of The Electrochemical Society **146** (8), 2886-2891 (1999); N. Zech, E. J. Podlaha, and D. Landolt, "Anomalous Codeposition of Iron Group Metals: II. Mathematical Model," Journal of The Electrochemical Society **146** (8), 2892-2900 (1999).

19 R. D. Ellerbrock, A. Fuest, A. Schatz et al., "Mössbauer Effect Study of Magnetism and Structure of fcc-like Fe(001) Films on Cu(001)," Physical Review Letters **74** (15), 3053 (1995); V. L. Moruzzi, P. M. Marcus, and J. Kübler, "Magnetovolume instabilities and ferromagnetism versus antiferromagnetism in bulk fcc iron and manganese," Physical Review B **39** (10), 6957 (1989).

20 B. Schulz and K. Baberschke, "Crossover from in-plane to perpendicular magnetization in ultrathin Ni/Cu(001) films," Physical Review B **50** (18), 13467 (1994).

21 Farrel Lytle, "The EXAFS family tree: a personal history of the development of extended X-ray absorption fine structure," Journal of Synchrotron Radiation **6** (3), 123-134 (1999).

22 A. R. Denton and N. W. Ashcroft, "Vegard's law," Physical Review A **43**, 3161-3164 (1991).

23 P. J. Jensen and K. H. Bennemann, "Magnetic structure of films: Dependence on anisotropy and atomic morphology," Surface Science Reports **61** (3), 129-199 (2006).

24 C. A. F. Vaz, J. A. C. Bland, and G. Lauhoff, "Magnetism in ultrathin film structures," Reports on Progress in Physics **71** (5), 056501 (2008).

25 E. A. Smirnova, I. A. Abrikosov, B. Johansson et al., "Calculated magnetic properties of an Fe1-xNix monolayer on Cu(001)," Physical Review B **59** (22), 14417 (1999).

26 V. L. Sedov and O. A. Tsigel'nik, "Magnetic moments of iron atoms in Invar Fe-Ni alloys," Journal of Magnetism and Magnetic Materials **183** (1-2), 117-126 (1998).

27 E. Foy, S. Andrieu, M. Finazzi et al., "Magnetic instabilities in fcc FexNi1-x thin films," Physical Review B **68** (9), 094414 (2003).

28 Y. Marcus, *Ion properties*. (New York, 1997).

29 L. F. Yin, D. H. Wei, N. Lei et al., "Magnetocrystalline Anisotropy in Permalloy Revisited," Physical Review Letters **97** (6), 067203-067204 (2006).

30 A. Bounouh, C. Train, P. Beauvillain et al., "Kerr rotation and perpendicular magnetic anisotropy oscillations versus Cu(111) coverage thickness in Cu(111)/Co/Au trilayers," Journal of Magnetism and Magnetic Materials **165** (1-3), 484-486 (1997).

31   R. Vollmer, S. van Dijken, M. Schleberger et al., "Dependence of the Curie temperature on the Cu cover layer in x-Cu/Fe/Cu(001) sandwiches," Physical Review B **61** (2), 1303 (2000).

32   N. Janke-Gilman, M. Hochstrasser, and R. F. Willis, "Measuring atomic moment and magnetic order through magnetic linear dichroism with angular dependence studies of transition-metal alloys," Physical Review B **70** (18), 184439 (2004).

Chapter 6 – Conclusions & Perspectives

In this PhD work, we studied the magnetic properties of ultra-thin monometallic and bimetallic films electro-deposited on Au(111). Our aim is to understand down to the atomic level, the magnetic properties correlated with the film composition and structure, which are challenging to determine for such ultra-thin layers. For this purpose, we employed several complementary techniques: for determining the film structure and composition we performed X-ray diffraction and extended X-ray absorption fine structure using a laboratory X-ray spectrometer as well as synchrotron radiations, in addition to fluorescence measurements in a scanning electron microscope; the film flatness was determined by in-situ scanning tunneling microscopy; the magnetic properties were measured in-situ by magneto-optic Kerr effect in the polar and longitudinal geometries; we also performed ex-situ temperature dependent magnetic measurements using a superconducting quantum interference device. Although these different techniques may appear redundant, the comparison of the different results, especially in the case of the bimetallic layers was particularly instructive.

After the introduction and experimental chapters, chapter 3 was devoted to the study of Fe layers electrodeposited on Au(111). We found that the structure of Fe layers thicker than 3ML is bcc with the (110) orientation, whereas it is strained fcc (111) below 3ML. We also evidenced a spin reorientation transition from out-of-plane to in-plane at a thickness of ~2.2ML, which we attribute to the fcc to bcc structural transition. The magnetic measurements are also consistent with a rather large magnetic moment per atom below 2.2ML, which value, if corrected from moment lowering due to the ultra-thin film geometry, is very close to that of Fe fcc (2.75 μ_B). Above 2.2ML, we measure a magnetic moment per atom close to that of the bcc structure (2.2 μ_B). We could also determine the film interface anisotropy, which we found relatively large, indicating a positive Fe/solution interface anisotropy, which is rather uncommon.

In chapter 4, we give a brief summary of the growth and magnetic properties of Ni ultra-thin layers on Au(111), then we focus on Fe layers deposited on Ni/Au(111). Ni layers grow fcc with the (111) orientation and strain-free on Au(111). Ni layers do not present magnetic ordering below a thickness of ~2ML, because of the low Curie temperature. The layer magnetic moment is found to be in-plane and no spin reorientation transition was observed. When Fe is deposited

on top a Ni layer, the behavior is completely different. We could evidence that, in the presence of Fe, the Ni recovers a magnetic ordering at room temperature and the magnetization of the Fe/Ni film is out-of-plane up to ~1.5ML of Fe. By studying this behavior as a function of the Ni layer thickness, we also found that the Ni magnetic ordering concerns essentially the first atomic layer, the one in contact with the Fe layer.

The study of the growth and magnetic properties of bimetallic alloy is tackled in chapter 5, which represents an important part of this work. Indeed, the preparation and the study of bimetallic alloys ultra-thin films are challenging and new. Using the electrochemical dissolution curves correlated with the reflectivity and magnetic measurements, we succeeded in accurately estimating and controlling the alloy film composition in the thickness range 0−2ML. We also evidenced a thickness dependent composition starting from a ~50/50 composition to reach at ~2ML, the solution one. We could show that the Fe rich alloys form mainly a bcc structure and contain a tensile strain, whereas the Ni rich alloys are fcc with smaller in-plane strain. The difference between the strain values determined from XRD and from EXAFS allowed us to speculate on the spatial distribution of the lattice distortion, namely, the alloy films consist in alloy domains with moderate strain separated by domain boundaries with large lattice distortion. Regarding the magnetic properties, we succeeded in correlating the results of the different techniques, taking into account the magnetization drop of the alloy film due to the ultra-thin geometry. We evidenced a clear drop of the average magnetic moment at a Fe content of ~60%, which we attribute to the fcc to bcc structural transition. The fact that this transition takes place at significantly lower Fe content than in UHV indicate the strong influence of the solution on the magnetic properties of the FeNi alloy films.

This work opens up perspectives in different directions. A direct follow up of this work, is exploring the influence of the deposition potential of FeNi alloys on microstructure and magnetic properties. We indeed expect specific structure close to the Fe^{+2}/Fe Nernst potential, where anomalous deposition takes place, i.e., when an enhanced Fe deposition rate occurs upon Ni co-deposition. In this deposition condition, special core-shell 2D morphology at the nanometer scale may be obtained which must strong modify the magnetic properties.

Another follows-up study would be replacing Ni by another element. For example, it would be interesting to study FeCo alloys in the ultrathin film limit, because pure Fe and pure Co have PMA and are also both ferromagnetic at submonolayer coverage. In the case of non

magnetic metal, it would be also interesting to compare FeCu and FePd alloys. Indeed, Pd is known to favor the PMA.

Finally, the capabilities of the *in-situ* MOKE measurements and the flow cell allows exploring the deposition of artificial ordered alloy by alternating one monolayer of each element at a time, so as to prepare novel thicker nanomaterials with PMA. It would be for example interesting to study Fe/Ni and Co/Ni multi-stacking as a function of the thickness of each layer (in a few atomic layer ranges). Such quantitative study would be possible with one combined *in-situ* MOKE and reflectivity measurements associated with the flow cell.